https://doi.org/10.35662/unine-thesis-3024

Université de Neuchâtel
Faculty of Sciences
Centre for Hydrogeology and Geothermics

Towards unprecedented spatiotemporal observations in hydrological systems using Uncrewed Vehicles

Ph.D. Dissertation

To obtain the degree of
Doctor of Science

Presented by
Kalliopi Koutantou
From Crete, Greece

approved in March 2023

At the request of

Prof. Philip Brunner
Prof. Philippe Renard
Dr. Tobias Jonas
Dr. Jorge Vazquez-Cuervo

Université de Neuchâtel
WSL
SLF
NASA Jet Propulsion Laboratory
California Institute of Technology

Université de Neuchâtel
Faculté des sciences

Rue Emile-Argand 11
CH-2000 Neuchâtel

doctorat.sciences@unine.ch

IMPRIMATUR POUR THESE DE DOCTORAT

La Faculté des sciences de l'Université de Neuchâtel autorise l'impression de la présente thèse soutenue par

Madame Kalliopi KOUTANTOU

Titre :

"Towards unprecedented spatiotemporal observations in hydrological systems using Uncrewed Vehicles"

sur le rapport des membres du jury composé comme suit:

- Prof. Philip Brunner, directeur de thèse, Université de Neuchâtel, Suisse
- Prof. Philippe Renard, Université de Neuchâtel, Suisse
- Dr Tobias Jonas, SLF Davos, Suisse
- Dr Jorge Vazquez-Cuervo, JPL/Caltech, USA

Neuchâtel, le 24 mars 2023

Le Doyen, Prof. R. Bshary

To my brother Grigoris,
my mother Lilly and my father Giannis,
who believed there is nothing I cannot achieve in my life.

Acknowledgments

Firstly, I would like to thank my Ph.D. advisor Professor Philip Brunner, who allowed me to pursue this dissertation, who trusted and supported me throughout the whole journey, and who contributed to my personal and scientific development.

I would also like to thank the colleagues I collaborated with from the University of Neuchatel: Laurent Marguet for his high motivation and patience to assist me during my fieldwork while trying to get to know my UAVs; Laurent Fasnacht for his contribution to getting my drone up in the air; Prof. Philippe Renard and Julian Straubhaar for their kindness to support my first endeavors with geostatistics and the rest of the CHYN members who made my stay at the lab very pleasant. Many thanks to Prof. Stéphane Burgos and his group from the Bern University of Applied Sciences for their contribution to my last Ph.D. project. I would also like to thank the Swiss National Science Foundation and the University of Neuchatel for funding my Ph.D. (R'Equip grant 206021_170753) and the latter also for awarding me a ''Fonds des donation'' grant for my visit to the NASA JPL.

I would like to express my gratitude to the research groups I collaborated with during my two exchange visits. Initially, the members of the Snow Hydrology group at the SLF who as great scientists helped me to build up my snow science background in the best working environment I could, and as the coolest people helped me get on skis for the very first time. Especially I would like to thank my Ph.D. co-mentor Dr. Tobias Jonas who allowed me to join his group and who as a well-rounded scientist taught me and assisted me with everything needed. Also, my Ph.D. projects at the SLF would not have been so successful without my friend and colleague Dr. Giulia Mazzotti, to whom I am grateful for her kindness, patience, and for sharing her admiring knowledge and cool scripts. Additionally, I owe an enormous thank you to my mentor at NASA JPL Dr. Jorge Vazquez-Cuervo who helped me fulfilling my deepest engineering dream to become a NASA intern by joining the Ocean Circulation and Air-See Interaction Group. Many thanks to the rest of the group members for giving me the chance to chat with NASA scientists, especially my friend and colleague Dr. Rachel Spratt.

Special thanks to my Ph.D. committee members Prof. Philip Brunner, Prof. Philippe Renard, Dr. Tobias Jonas, and Dr. Jorge Vazquez-Cuervo for accepting to review my thesis.

Furthermore, I was glad to meet great people during my Ph.D. who became my friends and believed in me; without them, my social and Ph.D. life would not have been the same.

Lastly and most importantly, I would like to express my gratitude to my family who made me love science since my school years, provided me and supported me since I was a kid with everything I needed, and for making me the person I am now.

Neuchâtel, February 2023 Kalliopi Koutantou

Abstract

The improvement of water resources management has been a big challenge and the appropriate use of water is of high importance for the ecosystems and the human population globally. Climate change affects the water cycle and therefore water use and human activities around the world. There is therefore an increased need for better monitoring of the water resources and the understanding of the hydrogeological processes that take place in hydrological and hydrogeological systems. Remote sensing technology has been intensively used to monitor water bodies, but so far mainly via satellites and crewed aircraft.

However, there are still limitations in terms of data resolution and lack of in situ data in isolated and difficultly accessible areas. Therefore, there is a need for more advanced technologies that can observe the water at finer spatial and temporal scales. In this context, uncrewed vehicles with their innovative autonomous technology and their high spatiotemporal resolutions open a new era in the study of hydrogeological systems.
Uncrewed aerial vehicles (UAVs) have been used in hydrogeological studies due to their operational flexibilities such as their ability to fly at low altitudes, in challenging environments, and whenever the user needs them at low costs. These flexibilities overcome the low spatial and temporal resolutions of the satellite data and the high costs of crewed aircraft data acquisitions.
Besides the UAVs, uncrewed surface vehicles (USVs) have also been used in ocean studies due to their autonomous and long-range navigation. Their high sampling frequencies and their ability to directly sample the ocean surface and not just a few meters underneath, make them more favorable than traditional in situ measurement platforms such as buoys or other crewed boats.

The aim of this Ph.D. thesis is to improve the understanding of hydrogeological processes using this innovative technology of uncrewed vehicles. By combining various remote sensing platforms and data, we produced new datasets for the scientific community with unprecedented spatiotemporal resolutions. Our studies, using these uncrewed vehicle-borne data with their unprecedented spatiotemporal resolutions, prove the efficiency and potential of the uncrewed vehicle technology. We pursue four different studies related to different hydrogeological processes in different environments. The first study is a technical contribution to snow mapping techniques using UAV-borne LiDAR technology. The second study, which is the first-ever study conducted in steep forested terrain using UAV-borne LiDAR demonstrates the effect of canopy structure and solar radiation in the formation of snow patterns within the steep forested slopes. We also extract valuable technical contributions for similar future campaigns. The third study focuses on sea surface temperature dynamics on the California Coast and proves that Saildrone, an uncrewed surface boat, is capable of validating satellite products with its one-minute sampling frequency. It is the first study to compare MODIS level-2 with Multi-scale Ultra-high Resolution (MUR) level-4 satellite products over the California Coast and the first one to assess the accuracy of MODIS level-2 quality levels over the California Coast. The last study aims at mapping topsoil organic matter at high resolution by exploiting the soil spectral properties along with traditional laboratory analysis.

KEYWORDS:

water resources management; hydrogeological processes; remote sensing; uncrewed vehicles; uncrewed aerial vehicles; uncrewed surface vehicles; UAVs; USVs; LiDAR; snow hydrology; ocean dynamics; soil properties; hyperspectral

Résumé

L'amélioration de la gestion des ressources en eau a été un grand défi et l'utilisation appropriée de l'eau est d'une grande importance pour les écosystèmes et la population humaine dans le monde entier. Le changement climatique affecte le cycle de l'eau et donc l'utilisation de l'eau et les activités humaines dans le monde entier. Il est donc de plus en plus nécessaire de mieux surveiller les ressources en eau et de comprendre les processus hydrogéologiques qui se déroulent dans les systèmes hydrologiques et hydrogéologiques. La technologie de la télédétection a été intensivement utilisée pour surveiller les masses d'eau, mais jusqu'à présent principalement par le biais de satellites et d'avions pilotés.

Cependant, des limites subsistent en termes de résolution des données et de manque de données in situ dans les zones isolées et difficilement accessibles. Il est donc nécessaire de disposer de technologies plus avancées permettant d'observer l'eau à des échelles spatiales et temporelles plus fines. Dans ce contexte, les drones, avec leur technologie autonome innovante et leurs résolutions spatio-temporelles élevées, ouvrent une nouvelle ère dans l'étude des systèmes hydrogéologiques. Les véhicules aériens sans pilote (UAV) ont été utilisés dans les études hydrogéologiques en raison de leur souplesse opérationnelle, notamment leur capacité à voler à basse altitude, dans des environnements difficiles et à tout moment, à faible coût. Cette souplesse permet de surmonter les faibles résolutions spatiales et temporelles des données satellitaires et les coûts élevés de l'acquisition de données par des avions pilotés. Outre les drones, les véhicules de surface sans pilote (USV) ont également été utilisés pour l'étude des océans en raison de leur autonomie et de leur navigation à longue distance. Leurs fréquences d'échantillonnage élevées et leur capacité à échantillonner directement la surface de l'océan et pas seulement quelques mètres en dessous, les rendent plus favorables que les plateformes de mesure in situ traditionnelles telles que les bouées ou d'autres bateaux habités.

L'objectif de cette thèse de doctorat est d'améliorer la compréhension des processus hydrogéologiques en utilisant cette technologie innovante des véhicules sans pilote. En combinant diverses plateformes et données de télédétection, nous avons produit de nouveaux ensembles de données pour la communauté scientifique avec des résolutions spatio-temporelles sans précédent. Nos études, qui utilisent ces données transportées par des véhicules sans pilote avec des résolutions spatio-temporelles sans précédent, prouvent l'efficacité et le potentiel de la technologie des véhicules sans pilote. Nous menons quatre études différentes liées à différents processus hydrogéologiques dans différents environnements. La première étude est une contribution technique aux techniques de cartographie de la neige à l'aide de la technologie LiDAR embarquée sur drone. La deuxième étude, qui est la toute première étude menée sur un terrain forestier escarpé à l'aide d'un LiDAR embarqué sur un drone, démontre l'effet de la structure de la canopée et du rayonnement solaire sur la formation de motifs de neige dans les pentes forestières escarpées. Nous avons également obtenu des contributions techniques précieuses pour des campagnes similaires à venir. La troisième étude porte sur la dynamique de la température de surface de la mer sur la côte californienne et prouve que Saildrone, un bateau de surface sans équipage, est capable

de valider les produits satellitaires grâce à sa fréquence d'échantillonnage d'une minute. Il s'agit de la première étude comparant les produits satellitaires MODIS niveau 2 et MUR (Multi-scale Ultra-high Resolution) niveau 4 sur la côte californienne et de la première étude évaluant la précision des niveaux de qualité MODIS niveau 2 sur la côte californienne. La dernière étude vise à cartographier la matière organique de la couche arable à haute résolution en exploitant les propriétés spectrales du sol ainsi que les analyses traditionnelles en laboratoire.

MOTS-CLÉS:

gestion des ressources en eau; processus hydrogéologiques; télédétection; véhicules sans équipage; véhicules aériens sans équipage; véhicules de surface sans équipage; UAV; USV; LiDAR; hydrologie de la neige; dynamique des océans; propriétés du sol; hyperspectral

List of contributions

Journal publications

Koutantou, K., Mazzotti, G., & Brunner, P. (2021). UAV-BASED LIDAR HIGH-RESOLUTION SNOW DEPTH MAPPING IN THE SWISS ALPS: COMPARING FLAT AND STEEP FORESTS. *The International Archives of the Photogrammetry, Remote Sensing and Spatial Information Sciences*, *XLIII-B3-2021*, 477–484.
DOI: https://doi.org/10.5194/isprs-archives-XLIII-B3-2021-477-2021
(Cited 7 times)

Koutantou, K., Mazzotti, G., Jonas T., Webster C., & Brunner, P. (2022). Exploring snow distribution dynamics in steep forested slopes with UAV-borne LiDAR. Cold Regions Science and Technology, Volume 200, 103587.
DOI: https://doi.org/10.1016/j.coldregions.2022.103587
(Cited 9 times)

Koutantou, K., Brunner, P., & Vazquez-Cuervo, J. Validation of NASA Sea Surface Temperature Satellite Products using Saildrone data. *Remote Sens. 2023, 15*, 2277.
DOI : https://doi.org/10.3390/rs15092277
(cited 1 time)

Collaborations

- Visiting Ph.D. student at the Swiss Federal Institute for Snow and Avalanche Research SLF, Snow Hydrology Group, *February 2019-April 2019 & December 2019-June 2021*
- Visiting Ph.D. student at the NASA Jet Propulsion Laboratory, Ocean Circulation and Air-Sea Interaction Group, *May 2022-September 2022*
- Ph.D. Student Collaborator of the Bern University of Applied Sciences, School of Agricultural, Forest and Food Sciences HAFL, collaborating with Prof. Stéphane Burgos, *August 2021-January 2023*

Awards

- ‘‘Fonds des donation’’ grant for the 5-month internship at the NASA Jet Propulsion Laboratory, *July 2022*

Table of Contents

Acknowledgments *7*

Abstract *9*

Résumé *11*

List of contributions *13*

1.Introduction *19*

1.1 Spaceborne and airborne remote sensing for hydrological studies 19

1.2 Spatiotemporal limitations in observational data 20

1.3 Uncrewed aerial vehicles in hydrology 20

1.4 Uncrewed surface vehicles 22

1.5 Scope of the Ph.D. thesis 23

2.UAV-Based LiDAR High-Resolution snow depth mapping in the Swiss Alps: Comparing flat and steep forests *25*

2.2 Methods 26

2.2.1 UAV acquisitions 26

2.2.2 In-situ snow depth measurements 27

2.2.3 Post Processing Kinematic correction of the UAV trajectory 28

2.2.4 Manual strip adjustment 28

2.2.5 Registration of the scans 29

2.2.6 Snow/Ground classification 30

2.2.7 Snow mapping over the flat forested terrain 31

2.2.8 Snow mapping over the steep forested terrain 33

2.2.9 Snow depth maps validation 35

2.3 Results and discussions 36

2.3.1 UAV data acquisitions in forested environments 36

2.3.2 Registration of strips and scans 37

2.3.2 Snow depth maps validation 38

2.3.3 Snow/ground classification 38

2.3.4 Evaluation of the snow depth algorithms and snow depth grids 39

2.4 Conclusions 42

3. ***Exploring snow distribution dynamics in steep forested slopes with UAV-borne LiDAR*** *45*

3.1 Introduction 46

3.2 Data 48

3.2.1 Study sites 48

3.2.2 Equipment and LiDAR data acquisition 49

3.2.3 Auxiliary data acquisition 50

3.3 Methods 50

3.3.1 UAV-borne LiDAR point cloud data processing 51

3.3.2 Snow depth data processing 53

3.3.3 Canopy structure data processing 54
3.3.4 Radiation modeling 56

3.4 Results 57
3.4.1 Snow depth maps accuracies 57
3.4.2 Spatio-temporal snow distribution dynamics relative to canopy structure 57
3.4.3 Spatio-temporal dynamics of sub-canopy incoming SWR 60
3.4.4 Correlations between snow distribution and local canopy structure 62

3.5 Discussion 64
3.5.1 The interplay between canopy structure and topography shapes snow distribution dynamics in forested slopes 64
3.5.2 Technical challenges, lessons learned, and recommendations for future UAV-borne LiDAR forest snow studies in steep slopes 66

3.6 Conclusions 68

4. Validation of NASA Sea Surface Temperature Satellite Products using Saildrone data 77

4.1. Introduction 77

4.2. Study area and data 81
4.2.1 Study area 81
4.2.2 In situ measurements 81
4.2.3 Satellite Sea Surface Temperature products 81

4.3. Methods 83
4.3.1 Sea Surface Temperature 83
4.3.2 Thermal gradients 83

4.4 Results 85
4.4.1 Sea Surface Temperature 85
4.4.2 Thermal gradients 90

4.5. Discussion 93
4.5.1 Accuracies compared to previous Saildrone studies 93
4.5.2 Accuracies compared to previous MODIS studies 94
4.5.3 Source of errors due to Saildrone 94
4.5.4 Source of errors due to mismatches between the instruments 95
4.5.5 Assessment of the MODIS quality levels and the MUR interpolation 95
4.5.6 Comparing both gradient approaches 96

4.6 Conclusions 96

5.Fine spatial resolution topsoil organic matter mapping using UAV-borne hyperspectral data: A preliminary study 103

5.1 Introduction 103

5.2 Methods 106
5.2.1 The study site 106
5.2.2 Hyperspectral data acquisition 106
5.2.3 Soil sampling 107
5.2.4 Auxiliary data acquisition 107
5.2.5. Remote sensing data processing 108
5.2.6 Laboratory soil analysis 110

5.2.7 Statistical analysis 111

5.3 Results and Discussion 112

5.3.1 Statistical analysis and soil organic matter map 112

5.3.2 Data quality assessment 116

5.3.3 Recommendations for future campaigns 117

5.4 Conclusions 118

6. Thesis Conclusions and Outlook 123

6.1 Contributions of the Ph.D. thesis 123

6.2 Potential of the UAVs for hydrological studies 124

6.3 Technical challenges of the uncrewed aerial vehicles 124

6.4 Uncrewed surface vehicles in the future 125

6.5 Personal Outlook 126

Bibliography 127

Curriculum Vitae 133

1. Introduction

Improving water resources management is particularly important for the protection of ecosystems and for human health and food security. Due to climate change and its effects on the water cycle, there is an increased need for monitoring water resources for efficient water use (Cui et al., 2019). Being able to accurately map and study hydrological and hydrogeological processes is challenging, given the high spatial and temporal variability of hydrological state variables, and the physical parameters and climatic forcing functions affecting them (Chawla et al., 2020; Gholizadeh et al., 2016). Remote sensing technology can provide very useful information in this regard. In fact, this technology has proven crucial for assisting the development of water resources modeling and management practices (Brunner et al., 2007; Herndon et al., 2020; Kumar and Tv, 2013; Sagan et al., 2020). Owing to the rapid developments of UAVs and/or other uncrewed vehicles,< new possibilities to monitor hydrological systems are emerging. This Ph.D. thesis explores how uncrewed vehicles can be used to resolve the above-mentioned limitations of the existing hydrological studies.

1.1 Spaceborne and airborne remote sensing for hydrological studies

Satellite remote sensing (or spaceborne remote sensing) has been widely used to monitor hydrogeological systems and to complement existing hydrometeorological monitoring networks based on in situ data collection (Chawla et al., 2020; Sheffield et al., 2018).
Some of the most used satellites to map the water surface are the Landsat satellites (Landsat 5,8), the Moderate Resolution Imaging Spectroradiometer (MODIS), and the Sentinel satellites (Sentinel 2,3,6). The recently launched Surface Water and Ocean Topography (SWOT) satellite with its altimetry technology will offer the first global monitoring of the Earth's water surface table dynamics. The sensors onboard Landsat 5 (Multispectral Scanner (MSS), Thematic Mapper (TM)), Landsat 8, MODIS, and Sentinel 2 Multispectral Instrument (MSI) are multispectral. Recently, hyperspectral spaceborne sensors are also used in water-related studies, due to their increased spatial and spectral resolutions compared to multispectral sensors (Cao et al., 2022; Flores-Anderson et al., 2020). With their ability to map the water surface at big spatial extents, different studies with spaceborne optical, infrared, and microwave sensors have been done to study water depth, water quality, surface water discharge, snow, soil moisture, etc.

Airborne spectral imaging spectroscopy is also used for water quality assessment (Chadwick et al., 2020; Mbuh, 2019; Olmanson et al., 2013). Some of the most used airborne (crewed helicopters and airplanes)-based sensors are the Airborne Visible Infrared Imaging Spectrometer (AVIRIS) from the NASA Jet Propulsion Laboratory, the HyMap from the Earth Search Sciences Inc. and the Hyperspectral Digital Imagery Collection Experiment (HYDICE) from the Naval Research Lab. The airborne sensors offer better spatial resolutions than the spaceborne sensors, down to a few meters, because they fly in lower altitudes. However, compared to satellite missions, they cover smaller spatial areas. Additionally, airborne applications come with high costs and therefore their temporal resolution is restricted.

1.2 Spatiotemporal limitations in observational data

As it is described in more detail above, satellites and crewed aircraft applications cover study areas of large spatial extent but at limited spatial and temporal resolutions. Therefore, their coarse spatial resolutions might prohibit them from studying small inland waterbodies such as small lakes and rivers (Schaeffer et al., 2013; Sun et al., 2022). Also, the temporal resolution is restricted due to the high cost and logistic efforts and from the scheduled orbit in the case of the crewed aircraft and the satellite applications, respectively.

In situ measurements are important for the validation of remote sensing data. However, acquiring in situ water samples is a time-consuming procedure, only representative of point locations, and often restricted in terms of field site accessibility (Bierman et al., 2011). In situ water measurements acquired only at specific locations and at a specific date and time do not always represent the water parameters of the whole water body nor the water parameters of a longer time period (Schaeffer et al., 2013).

Considering the abovementioned limitations of the existing remote sensing platforms there are still multiple, unresolved issues from a water resource management perspective. These remaining issues would strongly benefit from more robust and spatially resolved mapping approaches. Snow dynamics, mapping of soil properties, and understanding temperature dynamics in the sea or lakes are a few examples of open questions which would potentially be brought to a new level by using the new and rapidly developing technologies in the field of remote sensing. New remote sensing platforms can offer more flexibility than existing technologies in terms of operation and mapping. An innovative, increasingly used and evolving remote sensing technology is the uncrewed vehicles which are briefly introduced in the following paragraphs.

1.3 Uncrewed aerial vehicles in hydrology

A rapidly evolving remote sensing technology that can assist in resolving the limitations of air-and spaceborne approaches described above is the uncrewed aerial vehicles (UAVs). The UAVs offer numerous advantages in terms of operation: They acquire data at fine and unprecedented spatial scales and temporal resolutions (Acharya et al., 2021; Hill et al., 2020; Sibanda et al., 2021; Vélez-Nicolás et al., 2021). Their ability to fly very close to the observed target produces UAV-borne data of high spatial resolution, even of a few centimeters, a resolution that cannot be achieved by spaceborne and crewed airborne sensors. This flexibility in space and time assists the study of small-scale hydrogeological processes (Vélez-Nicolás et al., 2021).
Another advantage of UAVs compared to spaceborne and crewed airborne applications is their ability to operate even in difficult and inaccessible environments. UAVs can operate in areas that are not covered by the defined orbit of the satellites or areas where crewed aircraft are difficult to be launched (steep terrain, glaciers, etc.). Additionally, UAVs can operate in environments that humans cannot access due to difficult or impossible accessibility (steep terrain, avalanches, landslides, etc.).

In terms of data acquisition, UAV-borne data are not affected by clouds, which is one of the main constraints in the case of satellite data. UAVs can also be used for real-time hazard monitoring since they can be used at any time and in dangerous environments that humans cannot/are not allowed to access. In terms of data processing, UAV sensors are not affected by atmospheric interaction and atmospheric transmittance (Golubkov et al., 2018) due to the low-altitude flights, making the data processing less complicated. Therefore, no atmospheric correction is needed, which is a very demanding workflow over inland and coastal water bodies (Mouw et al., 2015).

UAVs have started being used in various hydrological and water management-related studies (Acharya et al., 2021; Arango and Nairn, 2020; DeBell et al., 2016; Vélez-Nicolás et al., 2021). A big variety of applications includes flood detection, climate change, snow and ice monitoring, and mapping of different soil properties (soil moisture, soil organic matter, etc.).

Nowadays, UAVs' capabilities in design, battery consumption, sensor characteristics, and available software for data processing are rapidly improving, offering better mapping options, less logistical efforts, and more straightforward data processing.
In hydrogeological studies, UAVs are mainly used with optical, multispectral, hyperspectral, and thermal sensors as well as LiDAR scanners (Isgró et al., 2022; Lu et al., 2021; Maesano et al., 2020; Peterson and Zhang, 2005; Zarco-Tejada et al., 2012). An accurate data processing workflow can retrieve point clouds, digital elevation (or surface) models, orthomosaics, and thermal and reflectance maps of high spatial resolutions, depending on the characteristics of the flights and the capabilities of the sensors. Fusion of sensors mounted at the same time on the UAV can offer more advanced final data outputs and a more advanced research (Alevizos et al., 2022; Baluja et al., 2012; Casas-Mulet et al., 2020). UAV-borne LiDAR technology is evolving due to the high-resolution elevation data and object detection it can provide. Flood assessment, accurate groundwater level mapping, underwater vegetation monitoring, bathymetry and snow mapping are a few UAV-borne LiDAR applications that prove the efficiency of this technology (García-López et al., 2023; Jacobs et al., 2021; Maesano et al., 2020; Trepekli et al., 2022). Besides the UAV-borne LiDAR technology that is rapidly advancing, UAV-borne hyperspectral sensors are more and more used since they offer high spectral resolutions. Various UAV-borne hyperspectral studies have already been performed mainly for water quality monitoring, soil mapping and soil quality evaluation, and flood detection (Levy and Johnson, 2021; Liu et al., 2021; Yu et al., 2022).

However, despite being a promising technology that advances rapidly, the operation of UAVs comes with many challenges that need to be taken into consideration. Initially, before the UAV operation, accurate flight planning is crucial for ensuring the acquisition of good quality data according to the needs of each study (flying altitude, ground sampling distance, speed, etc). The sensors mounted on the UAVs should be correctly calibrated before the data acquisition. There are also unpredictable technical challenges related to the operation of the UAVs, such as technical failures related to the UAV itself, battery malfunctions, or collision with obstacles or other aerial vehicles. Heavy sensors that operate by consuming energy from the UAVs can increase the risk of failure during the flight due to low battery voltage. Additionally, the UAV operation has to follow the safety rules of each country. Therefore, before going to the field the UAV pilot should be sure that follows all the safety

guidelines related to the operation of the UAV away from human beings, the existence of other vehicles in the sky, etc.
Considering all these potential risks while flying, the UAV pilot should be experienced enough to tackle rapidly any problem that might appear in the field site and retain the safety of the people, the constructions around the field site, and the equipment used. These potential risks can increase in difficult environments (steep terrain, the existence of human-made constructions, etc.).
Besides the accurate flight planning, the sensors' calibration, and the operation safety, the data processing workflow applied to the data is also crucial. Depending on the study, the type of data, and the desired final remote sensing product, the data processing workflow should be adjusted accordingly to eliminate noise within the data, co-register different datasets, and include any other steps needed to derive a high-quality remote sensing product that will be used for the study of the different hydrogeological parameters.

In this thesis, as described analytically in each chapter separately, we had to deal with many of the abovementioned technical challenges mainly related to the environment and data processing. Therefore, this thesis aims at advancing the use of UAVs for hydrogeological studies by providing important insights into the technical aspects of UAV operation, especially in challenging environments.

1.4 Uncrewed surface vehicles

Besides UAVs for different hydrogeological applications, other uncrewed technologies are also evolving, such as uncrewed surface vehicles (USVs). The USVs are uncrewed boats or ships that operate on the water surface and are used in oceanography and environmental monitoring (Nikishin et al., 2020; Totland and Johnsen, 2022; Yang et al., 2018). They are mainly deployed in oceans, retaining the abovementioned advantages of the UAVs but also offering higher spatial coverage and full autonomy (no need for remote-control use).

One of the most used and advancing autonomous surface technologies for ocean studies is the Saildrone (https://www.saildrone.com). It is a wind-driven and solar-powered boat with meteorological and oceanographic sensors capable of mapping the ocean even in difficult and isolated environments. Its field of application includes climate, mapping, and maritime security. Saildrones can sample a big amount of ocean parameters such as chlorophyll concentration, seawater conductivity, air pressure, seawater salinity, and seawater temperature every minute. They have already been successfully used in missions in the Arctic, the Atlantic, the Pacific, the North Sea, and the Mediterranean Sea (Chiodi et al., 2021; Vazquez-Cuervo et al., 2022; Zhang et al., 2022). The high sampling frequency of the Saildrones makes them promising technology for the validation of satellite ocean products, especially in areas where in situ data acquisition is restricted, and satellite data have gaps, such as in coastal, cloud-covered areas.

1.5 Scope of the Ph.D. thesis

This Ph.D. thesis explores to what extent the evolving technology of uncrewed vehicles can be employed to provide robust information in environments and spatiotemporal resolutions that other remote sensing platforms are difficult or impossible to provide.
Whereas technological evolution in terms of data acquisition is advancing rapidly, the application of these evolving technologies to monitor hydrological systems is still difficult. Especially for uncrewed vehicles, despite the operational flexibility they offer, their deployment also comes with many difficulties, especially in challenging environments.
In the thesis, we reduce the ‘‘application gap’’ between the technology and its application, and while doing this we provide numerous insights into the state variables of hydrological systems. Also, this thesis extracts useful technical insights related to the UAVs operation aiming to facilitate their use in future studies over similar environments.

The thesis integrates UAV and spaceborne applications using data of unprecedented spatiotemporal resolution from a variety of sensors: From spaceborne multispectral imaging radiometers to UAV-borne hyperspectral and LiDAR sensors.

The thesis consists of the four different projects that follow:

- UAV-based LiDAR high-resolution snow depth mapping in the swiss Alps: Comparing the snow mapping techniques for flat and steep forests
- Exploring snow distribution dynamics in steep forested slopes with UAV-borne LiDAR
- Validation of NASA Sea Surface Temperature satellite products using Saildrone data
- Fine spatial resolution topsoil organic matter mapping using UAV-borne hyperspectral data: A preliminary study

The structure of the thesis is as follows: The current introduction, four chapters that each correspond to the abovementioned four projects, and the Thesis conclusions and outlook in which the outcomes of the thesis are analyzed along with perspectives of future UAV-borne remote sensing studies in hydrogeology.

2. UAV-Based LiDAR High-Resolution snow depth mapping in the Swiss Alps: Comparing flat and steep forests

Publication:
Koutantou, K., Mazzotti, G., & Brunner, P. (2021). UAV-BASED LIDAR HIGH-RESOLUTION SNOW DEPTH MAPPING IN THE SWISS ALPS: COMPARING FLAT AND STEEP FORESTS. *The International Archives of the Photogrammetry, Remote Sensing and Spatial Information Sciences*, *XLIII-B3-2021*, 477–484.
DOI: https://doi.org/10.5194/isprs-archives-XLIII-B3-2021-477-2021

Abstract

Snow depth mapping in Alpine forests is of high importance for hydrogeology, ecology, tourism, and natural hazards prevention. Different remote sensing approaches have been employed for the precise mapping of snow depth within forests. However, optical sensors cannot provide the below-canopy information. While Airborne Laser Scanning (ALS) systems have been used successfully in this context and allow obtaining data below canopies, the costs of acquisitions are very high, not allowing frequent data acquisitions. UAV-based LiDAR technology potentially can provide the critical below-canopy information at a lower cost and allows for frequent acquisitions.
First attempts to employ a UAV-based LiDAR system in forests have proven promising, but they are limited to flat forests and to grid-level snow depth calculations. In this study, we present UAV-based LiDAR data of both flat and steep forests. Different LiDAR processing workflows are analyzed and compared, and snow depth algorithms are used both at the point and the grid level. Whereas the UAV-LiDAR system proved capable of mapping snow in both environments, the steep forests' data processing comes with greater challenges, especially for the 3D registration, ground classification, and point-to-point snow depth calculations.

Keywords
UAV ; LiDAR ; forests; snow depth mapping; 3D registration; C2

2.1 Introduction

Forests cover around 30% of the surface of Switzerland. Especially in Alpine regions, the snow dynamics and the snowpack properties affect ecology (Wipf et al., 2009), water resources (Farinotti et al., 2012; Thornton et al., 2021) and are relevant for snowmelt forecasts and tourism (Pütz et al., 2011). They are also important in the context of natural hazards such as avalanche prevention (Einhorn et al., 2015).

However, mapping snow in forests remains a big challenge for remote sensing applications. Uncrewed Aerial Vehicle (UAV)-mounted optical sensors appear inefficient in mapping snow below canopies (Harder et al., 2020). Airborne LiDAR Systems (ALS) show promising capabilities in mapping snow in forests within different scales and canopy types (Hopkinson et al., 2004; Currier et al., 2019). However, apart from the high cost of data acquisition, challenges related to the forested environment can underestimate the snow depths (Hopkinson et al., 2004). Also, data gaps below the canopy (Mazzotti et al., 2019; Broxton et al., 2015) can limit ALS systems' application to map snow dynamics. UAV-based LiDAR techniques potentially overcome the constraints of optical sensors by capturing both canopies and the sub-canopy snow surface at the same time. The feasibility of frequent scans of various scanning angles in contrast to the ALS systems leads to denser point clouds and differential snow depth grids of high spatial and temporal resolution. Only a few UAV-based LiDAR studies for forest snow mapping have been published (Harder et al., 2020; Jacobs et al., 2021). The challenges identified include accurate flight planning and the subsequent LiDAR-related processing workflows. These challenges are accentuated in steep forested terrain due to the difficulties of operating UAVs in such terrain. However, steep terrain typically leads to increased vertical inaccuracies for LiDAR systems with larger laser beam footprints (Deems et al., 2013; Baltsavias et al., 1999). For this reason, UAV-based LiDAR has the potential to generate snow cover datasets of higher quality than those that can be obtained by ALS in steep forested terrain, yet such an application has not been attempted yet

In this study, we are presenting a UAV-based LiDAR approach and comparing snow mapping techniques over flat and steep forests. For the first time, we present UAV-based LiDAR data obtained over steep slopes with a high resolution of 0.5m and forest snow depth extraction directly from the point clouds.
The study's specific objectives are 1) presenting LiDAR data processing workflows for snow cover mapping in flat and steep forested terrain and 2) comparing 3D registration algorithms and the snow depth mapping techniques applied individually to each case study.

2.2 Methods

2.2.1 UAV acquisitions

UAV-based LiDAR data were acquired over a flat forest of 200 by 200m at Flin, Engadine, in the eastern Swiss Alps in 2018. One snow data acquisition in late March and a snow-free acquisition in

the middle of June were carried out. In 2019, data over two forested slopes of opposing orientation were collected over an area of the same extent in Davos Dorf. Eight and thirteen snow-on flights over the north and south-exposed slopes were complemented by snow-off flights at the end of March and at the beginning of May, respectively.

We used a Yellowscan Mapper II mounted on a multicopter from Altigator SA. The LiDAR system operates in the 905nm with a FOV of 100◦ and horizontal and vertical accuracies of 15 and 5 cm, respectively. It weighs approximately 3 kg (including battery), can carry a payload of 12 kg, and operates autonomously.

The flight planning for both 2018 and 2019 combined four interlaced flying patterns for each acquisition to achieve higher point densities. Each flying pattern consisted of four scanning lines. The flying altitude was retained at 70-80 m above ground, aiming to follow the topography in the steep forest case, and the flight speed was set to 3m/sec. These flying characteristics led to a mean point density of 30 points/m^2 per scan with a maximum of two returns per pulse.

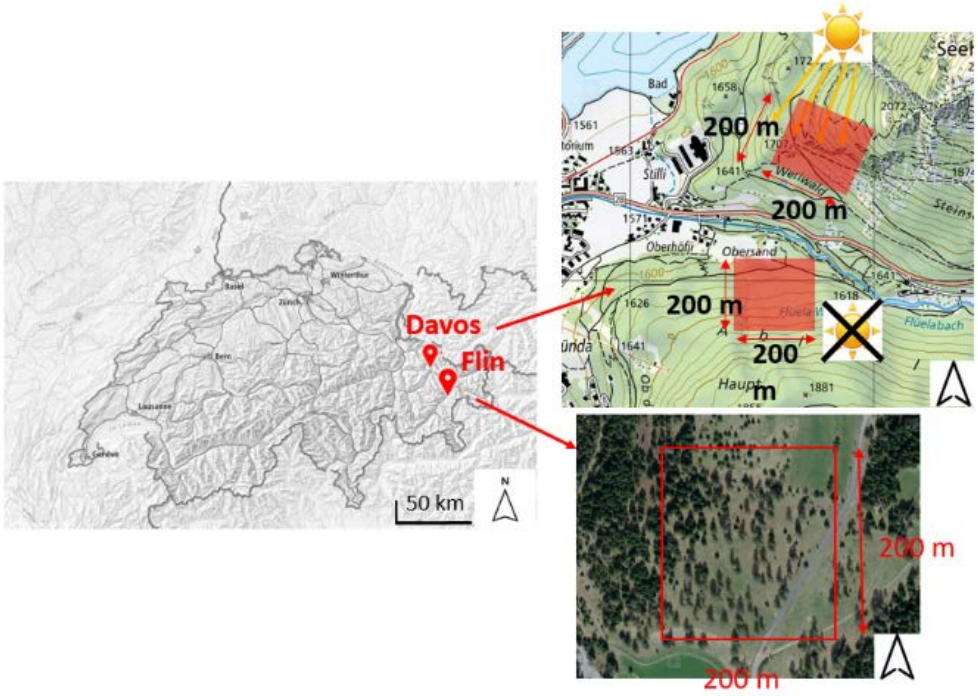

Figure 1: Field sites of the steep (upper) and flat forests (lower).

2.2.2 In-situ snow depth measurements

In-situ snow depth measurements were acquired for both studies to validate the snow depth maps. In the flat forest case, snow probe measurements were acquired in five different transects within the forest with a one-meter spacing. The measurements took place after the snow-on flight so as not to perturb the snow surface. 74 snow probe measurements were acquired in total within the five transects.

In the case of the steep forests, due to the difficulty in the accessibility of the sites and the need for in-situ snow measurements for each winter acquisition, we followed different procedures:
We used five snow depth sticks that we installed in fixed locations within the forests. They remained in the fields during the whole winter and were removed after the snowmelt.
In addition to the snow depths measurements on the snow depth sticks, we placed three plastic hemispheres covered with reflective tape on the snow surface during every acquisition. The reflective tape could backscatter the incident beams of the LiDAR in the wavelength of 905 nm. Therefore, the hemispheres could be identified on the point clouds (PCs) using the ‘‘intensity’’ value of each point that had been automatically recorded from the LiDAR system and saved as a scalar field on the PC. Absolute snow depths with a snow probe were measured in the center of the hemispheres. The snow depth sticks and the hemispheres used provided 8 in-situ snow measurements per acquisition.

2.2.3 Post Processing Kinematic correction of the UAV trajectory

The data from the INS of the LiDAR system that include both the IMU and GPS recordings were retrieved and converted into PCs using Yellowscan CloudStation (version 1.18.0, licensed).
For increased PC accuracy, the IMU and GPS data were further used to correct the raw UAV trajectory. This integrated forward and backward GNSS post-processing correction was performed using the POSPac UAV software (version 8.3, licensed). We used the GNSS data from a base station from the Swiss Continuously Operating Reference Stations (CORS) network near the field sites, within 2km. The Post Processing Kinematic (PPK) correction of the UAV trajectory led to a position accuracy of around 1-2 cm. The corrected trajectory was then exported as a Smoothed Best Estimated Trajectory (SBET) file and re-imported into the CloudStation to correct the PCs. This workflow was followed for all the data acquisitions of the flat and steep forests.

2.2.4 Manual strip adjustment

As a next step, for each acquisition, a strip adjustment quality check took place to evaluate the alignment of the four scanning lines. In some cases, even after the SBET-based post-processing of the PCs, there was a misalignment between neighboring scanning lines (hereafter strips). This can be related to uncertainties related to the calibration angles, unsuccessful initialization of the IMU, satellite loss, or heading drifts.

We thus established a manual strip adjustment workflow that was applied in case of misalignments after the SBET-based post-processing of the PCs. This workflow includes the selection of a random intersection of the two neighboring strips within the PC. The workflow took place on CloudCompare software (version 2.11, open-source). One intersection remained fixed (reference), while the other was manually moved to co-register to the reference. The 3D transformation matrix was then extracted and applied to the whole strips. A quality check was done to evaluate if the transformation matrix was well applied to all the corresponding strips' points. The process was repeated using different intersections until the extracted transformation matrix was successfully

applied to all the points. The workflow was applied separately for every two strips, and the final result was one PC for each scan.

The manual strip adjustment was mainly used for the steep forests data, where the higher alignment errors were identified within neighboring strips. For the flat forest, the SBET post-processed PCs yielded better strip alignment. Therefore it was not needed to apply the manual workflow.

2.2.5 Registration of the scans

The strip adjustment quality check mentioned in section 2.2.4 was followed by the registration of each acquisition's four flying patterns (hereafter scans). The aim was to extract one PC per acquisition, combining all four scans for increased point density. For the data of the flat forest, the Iterative Closest Point (ICP) algorithm was used for the registration of the four scans, as follows:

For every two scans, the ground points of the overlapping parts were used for the ICP algorithm. The scans' registration per acquisition for the flat forest took place after the snow/ground classification (see section 2.2.6). The ICP algorithm was applied only on the snow/ground points. The vegetation points were excluded since the canopy point density was not satisfying enough for the ICP algorithm to operate adequately.

After applying the ICP algorithm on the ground points of the overlapping parts of the two scans, the 3D transformation matrix was extracted and then applied to the whole PCs of the corresponding scans. The quality check included selections of random intersections within the PCs to evaluate whether the 3D transformation matrix was well applied to all the points. If not, the ICP algorithm was re-applied but in a smaller sub-sample of the points within the scans' overlapping part until the 3D transformation matrix was well applied to all the points throughout the whole PCs.

This process took place for every two overlapped scans until all four of them were correctly co-registered to each other. The final result was one PC per acquisition. The ICP implementation, as well as the quality check, were performed using the CloudCompare software.
Interestingly, the ICP algorithm could not be applied to the forested slopes' data as it led to large errors (see section 2.3.2.2). Alternatively, we performed manual strip adjustment as described in section 2.2.4 using the whole scans instead of individual strips.

The co-registered PCs derived from the application of the ICP and the manual adjustment workflow were further used for the snow/ground classification.

2.2.6 Snow/Ground classification

The co-registered PCs derived from the application of the ICP and the manual adjustment workflow were further used for the snow/ground classification, which is an essential step for creating snow depth maps. It aims to separate the snow or ground from the vegetation points in order to extract the snow or bare earth surface. For this step, the lasground tool from LAStools software (academic version 198012, licensed) was used, which classifies points into ground and non-ground points.

2.2.6.1 Ground classification of the flat forest

In the flat forest case, for the snow-on PC, the lasground tool was used with the default parameters proposed for a flat natural environment (parameter set called ‘‘natural’’). Additionally, we applied the setting ‘‘offset = 0.6 m’’, which entails all points within this threshold from the initial ground-classified points to be classified as ground as well.

For the snow-off PC classification, the lasground algorithm had to account also for the underlying low vegetation in the middle of June when the snow-off acquisition took place. The low-vegetation points could be wrongly classified as ground points and therefore lead to an overestimation of ground elevations in the DEM of the snow-off acquisition, which would result in an underestimation of the snow depths. Despite the ‘‘natural’’ and ‘‘step 5’’ parameters suggested for the flat forest, the offset parameter was set to 0.8 meters in order to include all ground points.

2.2.6.2 Ground classification of the steep forests

The snow/ground classification workflow followed was different from the one used for the flat forest. In the case of the steep forests, the algorithm had to identify whether the differences between points are because they are of a different class or due to the elevation difference.
Since the south-exposed site was steeper than the north-exposed one, the vertical inaccuracies derived from the in-built LiDAR configuration were higher. This constraint affected the selection of the lasground parameters for the snow-on PCs, which were then different from those used for the north-exposed slope. Regarding the snow-off PCs' ground classification, the algorithm had to account also for the low-vegetation points. Since the snow-off acquisition for the north-exposed slope took place later than the south-exposed slope, the ground classification parameters used were different.

For the snow classification, for the south-exposed slope, the offset parameter was set to 0.7 meters. To remove all the spikes 5 meters above or below the initial snow classified surface, we set the ‘‘spike’’ parameter equal to 5 meters. To account for the forested environment, we used the parameter ‘‘nature’’ and in order to intensify the search of initial ground points due to the terrain's steepness, we added the parameter ‘‘hyper fine’’. With these selected parameters resulting from many iterations, we managed to separate the snow from the vegetation points even in the forest's steeper parts.

For the snow classification of the north-exposed slope, the parameters remained the same as those for the south-exposed slope. The only difference was the offset that was set to 0.5 instead of 0.7 m.

Regarding the ground classification of the snow-off PCs, the lasground tool had to account for the low-vegetation points and the steepness of the terrain.
For the south-exposed slope, we used the same parameters for the snow-on PCs. The offset in the case of the snow-off PC was set to 0.5 meters.

In order to remove the low-vegetation points, we additionally applied the lasthin tool. The ground classified points from the lasground tool were used on lasthin to keep only the percentile of 30% of the elevations within a step of 10 cm, similar to Mazzotti et al. (2019). This ‘‘percentile 30’’ parameter is aimed at retaining as ground points only the lowest points within the 30 % of the elevation values of all points within a step of 10cm. This concluded to a thinner ground surface that most of the low-vegetation points had been filtered out.

For the north-exposed slope, the lasground parameters were the same as those for the snow classification, with the difference of setting the offset to 0.8 meters. As in the south-exposed slope, the ‘‘percentile 30’’option on lasthin tool was used to filter out the low-vegetation points within a step of 10cm.
To evaluate the classification results for both flat and steep forests, we were visualizing the two classes via the ‘‘classification’’ scalar field assigned to the PCs during the classification process from lasground. Afterward, we took intersection within the classified PCs to evaluate whether the classification was efficient, especially in challenged parts, such as below-canopies. Not satisfying classification, including misclassified vegetation points or fluffy snow surface, led us to change the lasground parameters. The evaluation process was repeated until we extracted satisfying classification results, including as less as possible misclassified points and thin summer ground surface.

2.2.7 Snow mapping over the flat forested terrain

The snow and ground-classified PCs were used for the creation of the snow depth maps. The workflow followed for the flat and steep forest was different.

2.2.7.1 Cloud to Cloud (C2C) distance algorithm

The distances between the snow-on and snow-off ground classified points were estimated using the Cloud to Cloud (C2C) distance algorithm on CloudCompare. The C2C algorithm uses the one PC as a ‘‘reference’’ and computes the Euclidean distances to the second one that acts as the ‘‘compared’’ PC. The identification of the closest point on the compared PC is based on the Hausdorff algorithm (Rockafellar and Wets, 2005).

Before applying the C2C distance algorithm, we tested the relative position between the snow-on and snow-off PCs.
They are dependent on the geolocation inaccuracies between the acquisitions. These are relative to the initial processing (SBET post-processing, strip adjustment, and registration of the scans).
Despite the precise application of the registration method at the strip or scan level (ICP or manual strip adjustment), the registration comes with errors from millimeters to centimeters, depending on the quality of the PC (density, noise) and the accuracy of the method used. Since there are inaccuracies at each processing level, the final PCs retain all the processing steps' errors. Consequently, it is important to access the geolocation accuracies between the PCs.

We used the groomed street on the field site to detect potential misalignments between snow-on and snow-off PCs. Since the groomed road was snow-free during the snow-on and snow-off acquisitions, the two PCs were expected to be finely co-registered along this road, which was indeed the case. Consequently, no additional co-registration was required.
For the C2C distance algorithm, we used the ground-classified snow-off PC as reference, and the Euclidean distances to the snow-classified snow-on PC were computed. The distances were stored as a new scalar field into the ground classified snow-off PC and gridded into a 0.5m spatial resolution raster to yield a snow depth map. For the gridding, we selected the average values of points falling within a pixel of 0.5 by 0.5m. The gridding was also performed using Cloud Compare without using any type of interpolation for gap-filling purposes.

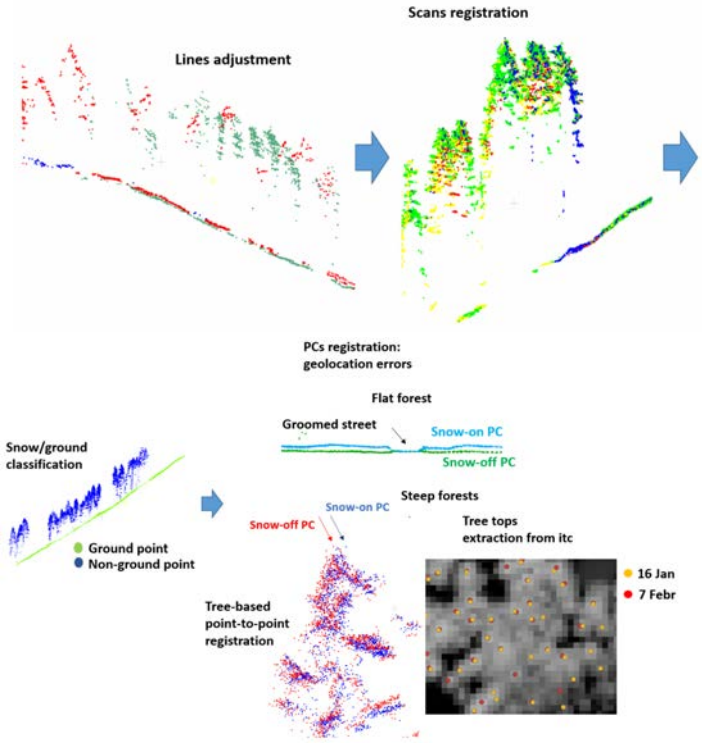

Figure 2: Point Cloud-level processing workflow.

2.2.7.2 DEM of difference (DoD)

The second methodology, called DEM of difference (DoD) is based on the subtraction of two DEMs to create a new one. The two initial DEMs used for the subtraction are the snow-on and snow-off DEMs. The produced DoD is the snow depth map.

This second approach acquires as a first step the gridding of the ground points of the snow-on and snow-off PCs.
The spatial resolution chosen for our study was 0.5m depending on the point density of the PCs. Finer resolutions of 0.2 and 0.3 m were tested but yielded many data gaps.

The PCs were gridded using the lasgrid tool from LAStools. Each pixel was given the average elevation value of all the ground points within an area of 0.5 by 0.5 meters. The resulting elevation rasters were the DEMs of the snow-on and snow-off acquisitions. By subtracting the snow-off DEM from the snow-on DEM, we created the DEM of difference (DoD) in which each pixel represents the snow depth value.

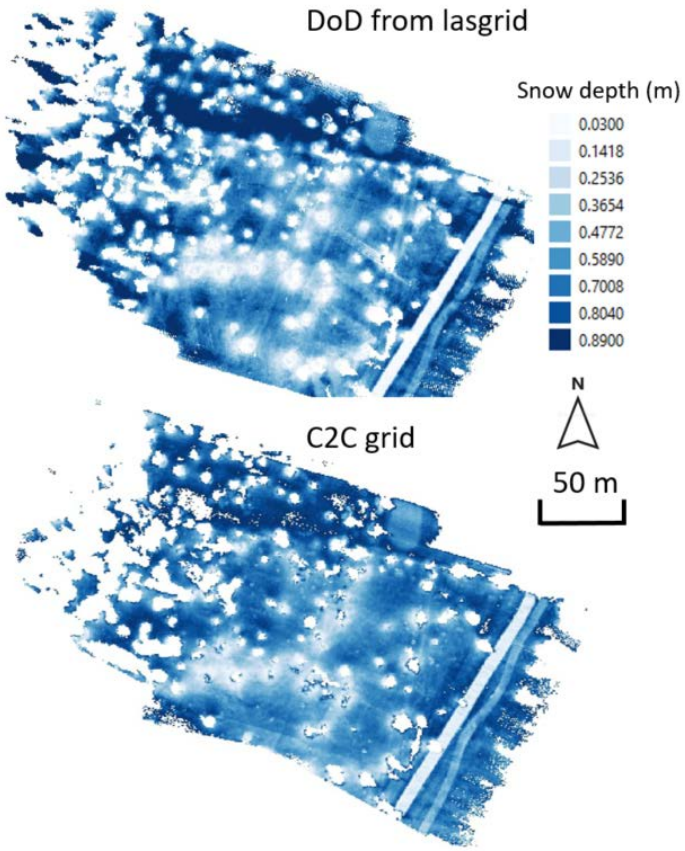

Figure 3: Snow depth grids extracted from DoD lasgrid and C2C algorithms.

2.2.8 Snow mapping over the steep forested terrain

The snow maps for the steep forested slopes were extracted using the before-mentioned DEM of difference (DoD) method. The C2C algorithm was initially tried on the data but yielded high errors due to the terrain's steepness (see section 2.3.5.2).

The steep forests lacked snow-free features within the sites that would have allowed evaluation of the alignment of the snow-on and snow-off PCs. To assess and minimize geolocation errors, we could only use tree points to register different PCs. As we were flying during wind-free conditions and when the snow intercepted in the tree branches was limited, the trees were stable features within all the acquisitions. The points corresponding to the branches and the treetops were therefore used for applying different feature-based 3D registration algorithms: point-to-point manual alignment, ICP algorithm, and 3D transformation proposed by Ferraz et al. (2018) were applied to our data.

The first two point-based methods did not identify pairing points in the trees (more details in section 2.3.2.2).
Alternatively, we used the registration workflow proposed by Ferraz et al., 2018. Since this is a registration methodology based on the treetop positions within the scans that need to be co-registered, we first had to segment the treetops.
We used the ITC segmentation package (itcSegment) integrated into R designed by Michele Dalponte (2018) to extract the positions of the treetops on the snow-off and each of the snow-on PCs. The 3D optimal rigid transformation was followed based on the extracted rotation and translation matrices from the treetops' coordinates. The snow-off PC was used as reference, and the registered one was used the snow-on PC. This method proved to be also not applicable to our data (see section 2.3.2.2).

Taking different transections within the different PCs, it was concluded that the geolocation errors within the different scans existed only in some locations in the PCs' borders. This made the misalignments non-uniform between the PCs. Therefore, the geolocation errors could not be quantified through the transformation matrices that were extracted from the abovementioned registration methods. Considering this data-related restriction, we proceeded with the snow depth gridding, acknowledging that those errors would be retained in the snow depth maps.

2.2.8.1 DEM of difference (DoD)

The ground-classified points of the snow-on and snow-off PCs were gridded into rasters of 0.5m spatial resolution, using the average elevation value of all the points falling within an area of 0.5 by 0.5 meters using the lasgrid tool.

The resulting grids were the DEMs of the snow-off acquisition. They were subtracted from each of the snow-on DEM and the output DoD raster was the snow depth grid. The same procedure was followed for all the snow-on acquisitions for both slopes.

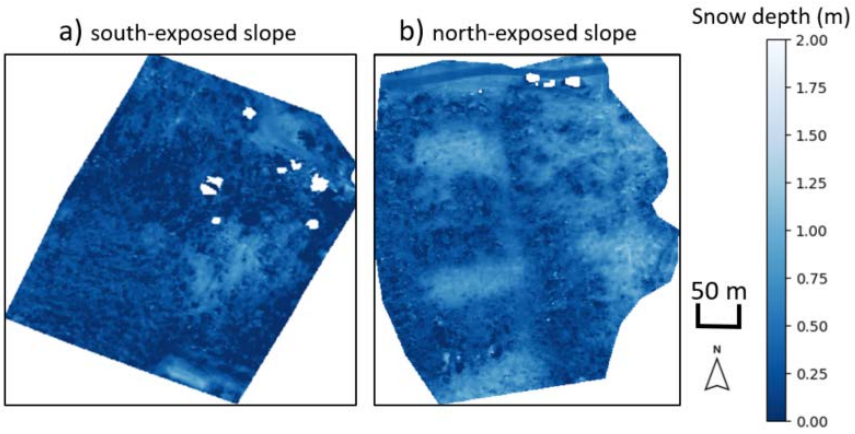

Figure 4: Snow depth maps for the south (a) and north (b) exposed steep slopes.

2.2.9 Snow depth maps validation

The in-situ measurements acquired as described in section 2.2.2 were used to validate the extracted snow depth maps.

For the flat forest, a canopy height model (CHM) of 0.5m resolution was applied to the snow-off PC using the lasheight tool from LAStools. The lasheight tool was applied to the snow-off ground classified PC to estimate each point's relative height above ground. Therefore, all the ground points were assigned zero Z coordinate and the vegetation points were assigned as Z coordinate their relative height above ground. This relative height above the ground of the vegetation point represented the canopy height per point and was gridded into a 0.5 m pixel size raster
The snow probe measurements' locations could be identified within the CHM by measuring their distances to the canopy edges. To compare point values with pixel values of an area of 0.5 by 0.5 meters, we created a buffer of 3 meters around the estimated snow probe location/pixel in the CHM. The final snow depth value that we were using to compare with the snow probe measurement at the specific location was the mean value of all the pixels perpendicular to the identified snow probe location/ pixel on the buffer's snow depth maps.

The RMSE between the snow probe measured and LiDAR-derived snow depth values were calculated for all the 74 locations within the five transects. The RMSE was calculated separately using both the C2C and DoD-derived snow depth maps and the results were compared to evaluate the efficiency of the two algorithms.

For the steep forested slopes, a canopy height model was also calculated with 0.5m pixel size using the lasheight tool. The snow depth sticks' position could be identified within the point cloud of the 1st of April since the hemispheres were placed in the middle of each bamboo stick. Hence, the coordinates of their locations were derived from the PC. The coordinates were afterward matched with the corresponding pixels on the snow depth maps. Hence, every stick's location was assigned to one pixel within the snow depth maps.

The measured value on each stick as well as the measured snow depths in the middle of the hemispheres were compared with the snow depth value of the corresponding pixel on the snow depth maps. These differences were expressed in terms of RMSE.
Since the steep forests were characterized by more complex accessibility that limited the in-situ measurements as well as by the lack of snow-free areas that could act as a reference as described in section 2.2.8, we followed an additional validation step. The measured snow depth values on the sticks and on the hemispheres were used to apply a vertical offset to each of the snow depth grids. The offset was calculated as the average difference between in-situ and LiDAR-derived snow depths at the corresponding pixels.

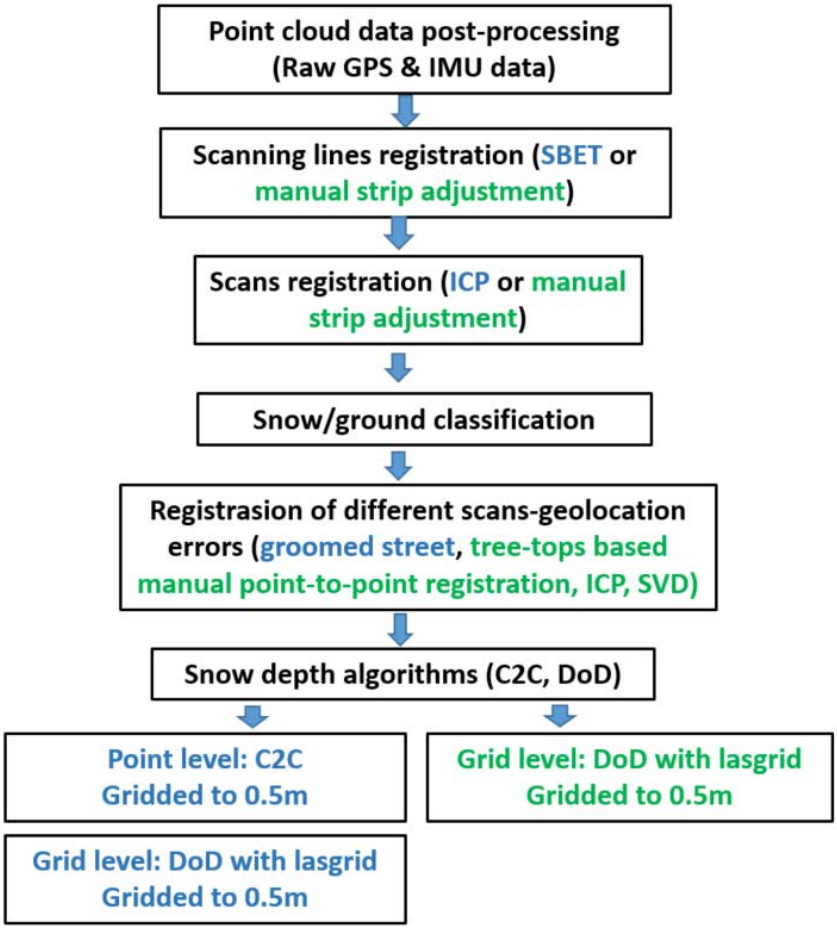

Figure 5: Schematic workflow of all the processing steps followed until the extraction of the snow depths maps. In blue the algorithms for the flat forest and in green the one for the steep forests.

2.3 Results and discussions

2.3.1 UAV data acquisitions in forested environments

The UAV operation in the forested Alpine environment proved challenging with respect to UAV flight planning, piloting, and data processing. The flight planning in the steep terrain was much more demanding than that in flat terrain, as it required the adjustment of the flying altitude to the elevation changes at every location. In addition to the challenging UAV operation over steep

forested terrain, the flying altitude adjustment forced the UAV to consume more battery capacity, resulting in a smaller surveyed area. In this terrain, restricted site accessibility due to avalanche danger also limited our capability to acquire ground-validation measurements, with further implications for data processing and evaluation (see section 2.3.2.2).

2.3.2 Registration of strips and scans

2.3.2.1 Evaluation of the manual strip adjustment

The manual strip adjustment proposed in this study proved to work efficiently for registering overlapping scanning lines and scans from different acquisitions. It can be applied alternatively when registration algorithms such as the ICP algorithm are inefficient due to low point densities, high noise, and limited spatial overlap. Note that this step demands many quality checks in different parts of the registered PCs after applying the 3D transformation matrix. Due to the lower accuracy of the LiDAR system in the borders due to smaller overlapping areas and lower point densities, a transformation matrix derived from points in the middle of the PCs may not appropriately represent the borders. Therefore, a quality check including all the parts of the PCs is recommended.

The increased error in the strip adjustment on the data of the steep forests that was observed can be due to the IMU's difficulty operating accurately when the UAV was changing elevations within two neighboring scanning lines to follow the topography.

2.3.2.2 Evaluation of the PC registration algorithms on the steep forests

As mentioned in section 2.2.8, both feature-based coarse and fine registration methods were used for the steep forests based on the tree points. Regarding the feature-based methods, the forested environments that were snow-covered and the lack of human-made constructions did not allow us to apply feature-based algorithms that are using standard features as tie points (e.g., corners of the buildings). Therefore, we were restricted to the use of the tree points for the implementation of any registration algorithm. The point-to-point manual registration based on tree points selected by the user proved unable to assign a uniform transformation matrix to the whole PC.

Regarding the fine registration algorithms, the ICP algorithm applied to the tree points could not effectively perform on our data. The ICP algorithm is highly dependent on the accuracy of the PCs in terms of noise and point densities. The ICP algorithm's inefficiency in operating on our data can be due to the low point density in the trees.

This means that the algorithm could not correctly identify the pairing points on the trees due to the beam's very low possibility to hit the exact same point at every scan. This was also why the manual point-to-point registration method did not work sufficiently well: It was difficult to identify precisely the same points in both PCs.

The rigid 3D registration workflow proposed by Ferraz et al., 2018 was also not applicable to our data, despite its promising application in cases where stable features on the surface are missing. The vectors between corresponding points in the two scans did not have the same orientation

throughout the whole PCs. This caused the inability of the used singular value decomposition (SVD)-based least-square fitting approach to extract a global rotation and translation matrix for the whole PC. The geolocation inaccuracies that we tried to quantify and minimize through scans were not uniform. The non-uniform inaccuracies within scans also restricted us from extracting differential snow depth grids. The mismatches in the relative positions between two consecutive scans were higher in the borders but difficult to quantify and eliminate. The non-uniformity in the inaccuracies between scans can be due to the decreased accuracy of the LiDAR IMU in the steep forests.

2.3.3 Snow depth maps validation

The snow-free pixels corresponding to the groomed road allowed the evaluation of the snow depth maps at the flat forest site. However, the road was occupying only a part of the east side of the forest. For the remaining areas, no snow-free features were present. Despite the snow probe measurements in the middle of the forest, there were no snow-free features in the west part of the field site, and neither snow probe measurements were acquired. Therefore, the snow depth map quality could not be evaluated within the whole area of the project. That leads to the conclusion that the intensive in-situ measurements and the snow-free areas that can act as a reference for the extraction of the snow depths are of high importance in snow depth mapping studies.
Additionally, the soil during June was wet due to the already-started snow melting. This introduced a systematic error in the snow probe measurements due to the probe's penetration into the soil. This error could not be quantified and therefore subtracted from the snow depth values as we did in the case of the snow depth stakes. Yet, despite the use of the average snow depth values of all the pixels within the 3m buffer to achieve the best representation of the snow probe measurements, the comparison between values in specific locations with the averaged values of an area of almost 3 m^2 introduced inaccuracies.

The same limitations in the validation process occurred in the steep forested slopes, mainly because of the limited number of validation measurements (only 8 per acquisition) due to the accessibility restrictions. The inaccuracies introduced by the comparison between snow depth values at specific locations with areas of 0.25m^2 were more substantial in the steep than in the flat forest due to the complex micro-topography. Therefore, we placed the snow depth sticks in comparably flat locations with limited micro-topography, so that the snow depths were expected to be uniform around these areas.

2.3.4 Snow/ground classification

While the snow/ground classification was revealed to be one of the major challenges for both of our studies, the classification in the case of the steep forests was significantly more complicated. This was due to the integration of the increased vertical inaccuracies of the LiDAR system on top of the IMU performance.

In the case of the steep forests, the lasground algorithm had to deal with the elevation changes within each step. More precisely, it had to identify whether the different elevations for points within the same cell are due to the steepness of the terrain or because they belong to different classes (ground/snow or vegetation).

The IMU-related inaccuracies that were increased in the steep forests, despite the ground classification procedure, led to fluffy snow and ground surface. To address this, a thinner snow/ground surface is recommended to be created to include only the snow points into a ‘‘median’’ snow surface, as proposed by Martin Isenburg (2021). This workflow is analyzed by Koutantou et al. (in preparation), where we present a snow/ground classification workflow for reducing the fluffiness of the snow surface, using the same data over the steep forests.

For the flat forest, the classified snow/ground surface was characterized by much less fluffiness. This can be associated with better IMU performance, already noticed on the strip adjustment processing step. Therefore no extra processing step, including the thinning of the classified ground/snow surface was applied to the data of the flat forest.

2.3.5 Evaluation of the snow depth algorithms and snow depth grids

2.3.5.1 The case study of the flat forest

As presented in Figure 6, based on the R^2 values, both C2C and DoD methods resulted in snow depths close to the in-situ measured. The RMSE for all the 74 points within the five transects is between 10-19 cm for the C2C and between 5-18 cm for the DoD method.

We see that in most transects, the lasgrid snow depths are closer to the in-situ ones. The C2C distance algorithm calculates Euclidean distances between identified pairing neighboring points. The Euclidean distances differ from the actual (vertical) distances that correspond to snow depths, and this explains the differences between in-situ and C2C-derived snow depths. Low densities can cause the identification of wrong neighboring points.

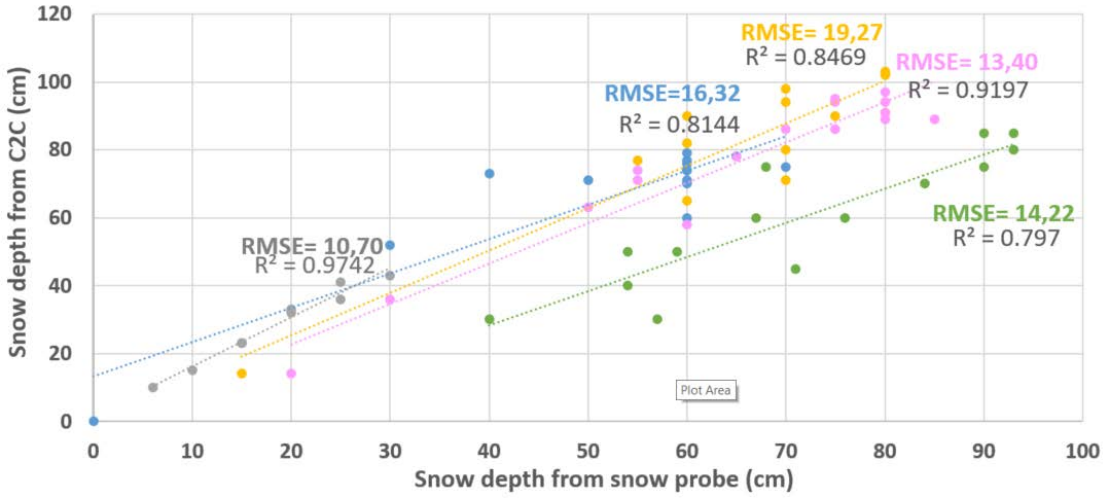

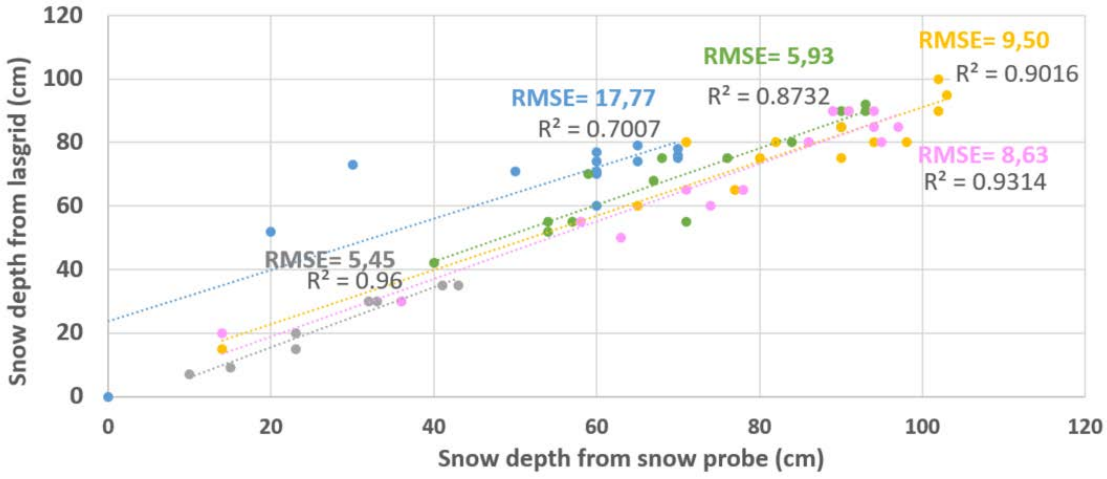

Figure 6: Linear correlations and RMSE for snow depths derived from C2C and DoD lasgrid algorithm. The different colors correspond to the five different transects.

Figure **7** reveals that for one transect within the forest, both C2C and DoD snow depths increase when moving from the canopy edges toward the open gaps. The same was noticed for the rest of the four transects. Also, the in-situ snow depth values in most locations are bigger than those extracted from both algorithms. This overestimation is probably due to the systematic error imposed by the snow probe's penetration into the soil. Both C2C and DoD methods proved to work in flat forests and complement the results based on studies in open sites.

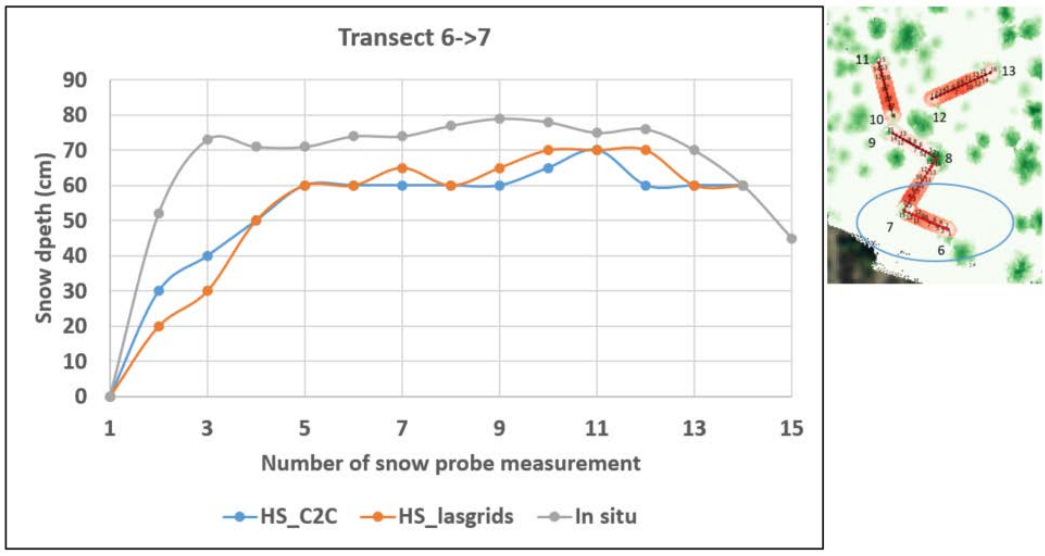

Figure 7: Snow depths within a transect, comparing in-situ observations with measurements derived from the PC's using different methodologies.

2.3.5.2 Steep forests

The C2C distance algorithm yielded high errors in the case of the steep forests. The data in the steep forests have increased low noise in addition to low point densities. Additionally, due to the terrain's steepness, the differences between estimated (Euclidean) and actual distances are even higher (

Figure 8).

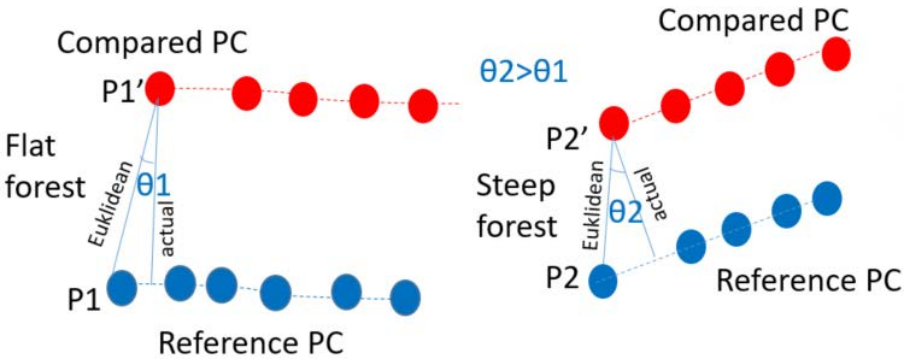

Figure 8: Effect of the slope on the estimation of the C2C Euclidean distances.

Alternatively, we used the local modeling technique on CloudCompare on the reference-snow-off PC to have a better model around the identified nearest point and extract distances closer to the actual (vertical) ones. Similarly, we also applied the cloud-to-mesh (C2M) distance algorithm on CloudCompare. Both the local modeling and the mesh-based methods showed high errors, especially in the forests' steeper parts and areas with lower densities, such as those close to the canopies. More advanced point-based algorithms, such as multiscale model-to-model cloud comparison (M3C2) have not been tested yet in steep forested terrain to our knowledge A first attempt to apply the M3C2 plugin on CloudCompare in our data was made with the default parameters. The algorithm's performance was similar to the performances of the C2C, local modeling, and point-to-mesh methods. A more advanced application of the M3C2 algorithm still needs to be tested and evaluated in steep forests.

Therefore, the grid-based snow depth extraction in steep terrain is more robust than point-based algorithms. Depending on the selected gridding resolution and the gridding value (i.e., an average of all elevations), it can lead to satisfying results. The DoD technique is the most common one for snow mapping studies, and our conclusion is compatible with studies already conducted in open sites. Lower resolutions could also eliminate
part of the noise during the snow/ground classification process.

Validation measurements of the absolute and relative snow depth values between LiDAR-derived snow depth grids and in-situ measurements showed an RMSE of 4-16cm for both steep sites (Figure 9) before implementing the offset. The implemented offset that was used reduced the RMSE at every snow depth stake location, as expected.

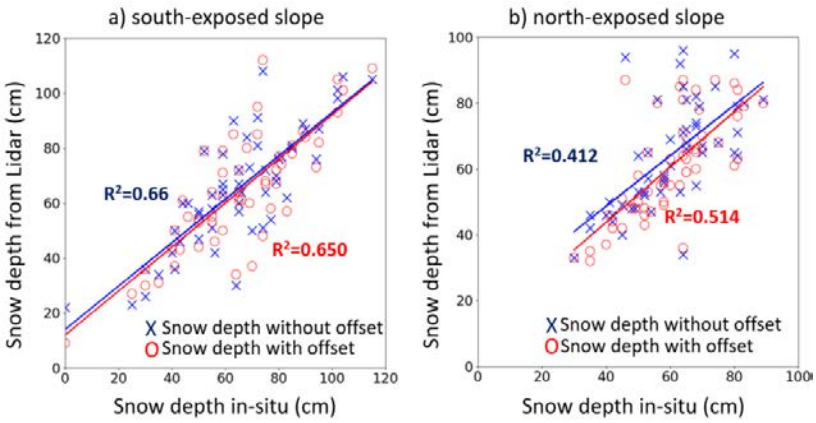

Figure 9: Snow depths before and after the application of the offset for the south (a) and north (b) exposed slopes.

The snow depth maps for the two forested slopes provide interesting data to investigate the distribution of the snow patterns relative to the canopy structure and topography (Koutantou et al., 2022).

2.4 Conclusions

This study presented the first application of UAV-based LiDAR specifically aimed at assessing its performance for mapping snow depth on flat versus sloped forested terrain. UAV-based LiDAR proved to be an efficient technology in capturing snow depths below canopies in flat and steep forests with a fine scale of 0.5m. Mapping steep forests included more challenges, from the accessibility of the sites to the data post-processing workflows in the point cloud and grid levels. Higher vertical inaccuracies are identified for the data over steep forests even after the PPK post-processing of the IMU and GPS data. The lower quality of the IMU performance in the steep forests imposed implications in the strip adjustment and in the snow/ground classification processes.
Comparing the 3D registration algorithms used, the manual strip adjustment introduced in our study worked efficiently in both terrains. Coarse and fine registration algorithms that were applied alternatively on the treetops of the steep forests were inefficient due to lower point densities and low noise that made the identification of pairing points very difficult.

Regarding the snow depth mapping, both C2C and DoD methods worked efficiently in the flat forest, with the DoD performing better. Evaluating the C2C algorithm in steep terrain for the first time yielded high errors due to the above-mentioned data restrictions (low densities and surface fluffiness). Thus, the grid subtraction method (DoD) proved to be more robust over the steep terrain.

Overall, our results confirmed UAV LiDAR as a promising tool for forest snow mapping in complex forested terrain, but they also revealed that many technical challenges still need to be overcome.

References

Applanix, 2019. POSPac UAV, Version 8.3, licensed. https://www.applanix.com/products/pospac-mms.htm

Baltsavias E.P., 1999. Airborne laser scanning: basic relations and formulas. ISPRS Journal of Photogrammetry & Remote Sensing, 54(2-3):199-214.

Broxton, P. D., Harpold, A. A., Biederman, J. A., Troch, P. A., Molotch, N. P., Brooks, P.D., 2015. Quantifying the effects of vegetation structure on snow accumulation and ablation in mixed-conifer forests, Ecohydrology, 8(6), 1073-1094. doi.org/10.1002/eco.1565

CloudCompare, 2020. Version 2.11 rc1, GPL software. http://www.cloudcompare.org/

Currier, W. R., Pflug, J., Mazzotti, G., Jonas, T., Deems, J. S., Bormann, K. J., et al., 2019. Comparing aerial LiDAR observations with terrestrial LiDAR and snow-probe transects from NASA's 2017 SnowEx campaign. Water Resources Research, 55, 6285– 6294. https://doi.org/10.1029/2018WR024533

Einhorn B**.,** Eckert N**.,** Chaix C**.,** Ravanel L**.,** Deline P**.,** Gardent M**.,** Boudières V**.,** Richard D**.,** Vengeon J.M**.,** Giraud G., Schoeneich P., 2015. Climate change and natural hazards in the Alps , *Journal of Alpine Research | Revue de géographie alpine* ,103-2 | 2015. doi.org/10.4000/rga.2878

Ferraz, A.; Saatchi, S.; Bormann, K.J.; Painter, T.H., 2018. Fusion of NASA Airborne Snow Observatory (ASO) LiDAR Time Series over Mountain Forest Landscapes. *Remote Sens.*, *10*, 164. https://doi.org/10.3390/rs10020164

Harder, P., Pomeroy, J. W., Helgason, W. D., 2020. Improving sub-canopy snow depth mapping with uncrewed aerial vehicles: LiDAR versus structure-from-motion techniques, The Cryosphere, Copernicus Publications 1994-0424. doi.org/10.5194/tc-14-1919-2020

Hopkinson, C., Sitar M., Chasmer, L., Treitz P., 2004. Mapping Snowpack Depth 704 beneath Forest Canopies Using Airborne LiDAR, Photogrammetric Engineering and Remote 705 Sensing, 70(3). doi.org/10.14358/PERS.70.3.323

Jacobs, J. M., Hunsaker, A. G., Sullivan, F. B., Palace, M., Burakowski, E. A., Herrick, C., Cho E., 2021. Snow depth mapping with unpiloted aerial system LiDAR observations: a case study in Durham, New Hampshire, United States, The Cryosphere, 15, 1485–1500, doi.org/10.5194/tc-15-1485-2021

Isenburg M., LAStools - efficient LiDAR processing software, version 190812, 2019, licensed, http://rapidlasso.com/LAStools

Isenburg Martin, 2021. Generating DTM for "fluffy" Livox MID-40 LiDAR via "median ground" points, https://rapidlasso.com/2021/04/08/generating-dtm-for-fluffy-livox-mid-40-LiDAR-via-median-ground-points/

Koutantou, K., Mazzotti, G., Jonas T., Webster C., & Brunner, P. (2022). Exploring snow distribution dynamics in steep forested slopes with UAV-borne LiDAR. Cold Regions Science and Technology, Volume 200, 103587. https://doi.org/10.1016/j.coldregions.2022.103587

Mazzotti, G., Currier, W.R., Deems, J.S., Pflug, J. M., Lundquist, J. D., Jonas, T.,2019. Revisiting snow cover variability and canopy structure within forest stands: Insights from airborne LiDAR data. Water Resources Research, 55, 6198– 6216. doi.org/10.1029/2019WR024898

Michele Dalponte, 2018. ItcSegment package, Version 0.8, GPL software. https://cran.rproject.org/package=itcSegment

Rockafellar, R. T.l*;* Wets, R. J-B*., 2005. Variational Analysis. Springer-Verlag. p. 117.* ISBN 3-540-62772-3.

Safieh J., Rebwar D., Forough J., 2020. Climate Change Scenarios and Effects on Snow-Melt Runoff. Civil Engineering Journal. 6. 1715-1725. 10.28991/cej-2020-03091577

Thornton J.M., Brauchli T., Mariethoz G., Brunner P., 2021.
Efficient multi-objective calibration and uncertainty analysis of distributed snow simulations in rugged alpine terrain, Journal of Hydrology,126241, ISSN 0022-1694, https://doi.org/10.1016/j.jhydrol.2021.126241

YellowScan CloudStation, 2021. Version 1.18.0-efd8deed, licensed

3. Exploring snow distribution dynamics in steep forested slopes with UAV-borne LiDAR

Publication:
Koutantou, K., Mazzotti, G., Jonas T., Webster C., & Brunner, P. (2022). Exploring snow distribution dynamics in steep forested slopes with UAV-borne LiDAR. Cold Regions Science and Technology, Volume 200, 103587.
DOI: https://doi.org/10.1016/j.coldregions.2022.103587

Highlights

- First time series of UAV-LiDAR based snow depth maps on two opposed forested slopes in the Alps
- At the north-exposed slope snow depth was correlated to canopy closure until mid-ablation
- Sun exposure throughout the season led to complex snow patterns at the south-exposed slope
- Recommendations on the use of UAV-based LiDAR for forest snow studies in complex terrain are provided

Abstract

Mapping snow in forests is important for understanding the snow cover dynamics in these environments in view of hydrological applications and water resources management. Today, Uncrewed Aerial Vehicles (UAVs) are widely used for snow studies due to their rather cheap and flexible operation. UAV-borne Light detection and ranging (LiDAR) systems are a promising technology for sub-canopy snow mapping at high temporal resolutions, concurrently providing information on both the canopy and the below-canopy snow surface. In this pilot study, we used a UAV-LiDAR system to investigate the snow cover dynamics within two steep forested slopes of opposing aspects in the Swiss Alps at both high spatial resolution and unprecedented temporal resolution. Using a Distance to Canopy Edge (DCE) algorithm to characterize local forest structure, snow depth was analyzed in terms of relative position within variable forest cover. The north-exposed site had higher mean snow depths throughout the season compared to the south-exposed site, especially in canopy gaps. Whereas snow depletion rate was consistent throughout the north-exposed site, snow depletion was much faster in the gaps at the south-exposed slope. Correlation coefficients between snow depths and local canopy closure were weaker at the south-exposed (between -0.5 and -0.7) than at the north-exposed site (between -0.7 and -0.9), and rapidly deteriorated right after the peak of winter at the south-exposed slope. This indicates shortwave radiation dominates snowmelt processes at this site, which was thought to be spatiuncorrelated

to local canopy cover, unlike accumulation and melt processes on the north-exposed slope that generated snow patterns with a high spatial correlation to local canopy cover throughout the entire season. Calculations of incoming sub-canopy shortwave radiation (SWR) for both sites confirmed this assumption. While our findings encourage the use of UAV-borne LiDAR for further investigations of snow cover dynamics in steep forested slopes, we also outline and discuss technical challenges specific to this application. Our insights allow deriving useful recommendations for future studies using UAV-borne LiDAR over a similar environment.

Keywords
UAV; LiDAR; Snow depth mapping; Steep forests; Canopy structure; Canopy radiative transfer

3.1 Introduction

Forests cover around 30% of the surface of Switzerland (Hunziker et al., 2012), and a large extent of the Northern Hemisphere is forested and features a seasonal snow cover (Essery et al., 2009). Snowmelt runoff originating from forests has a significant impact on hydrology, ecology, and climate (Javadinejad et al., 2020). Especially in Alpine regions, numerous studies have demonstrated the effect of snow cover dynamics on water resources (Farinotti et al., 2012; Thornton et al., 2021), natural hazards such as avalanches and floods (Einhorn et al., 2015; Björk & Molau, 2007), ecology (Nöthiger & Elsasser, 2004; Wipf et al., 2009) as well as tourism (Rixen et al., 2011; Elsasser & Bürki, 2002). As forests cover large areas that overlap with seasonal snow, forest snow cover dynamics need to be represented in models simulating snow cover dynamics in these environments (Mazzotti et al., 2020b; Mazzotti et al., 2021).

Spatially heterogeneous forest canopy causes correspondingly heterogeneous accumulation and melt patterns in both space and time (Lundquist et al., 2013; Currier & Lundquist, 2018; Mazzotti et al., 2019b). Snow cover dynamics in forests are thus usually more complex than in open sites (Clark et al., 2011). Accumulation patterns are affected by snow interception by the canopy (Hedstrom & Pomeroy, 1998a). The intercepted snow either sublimates, melts, or falls on the below-canopy snow surface (MacKay & Bartlett, 2006). Snowmelt is driven by a combination of processes such as the turbulent exchange of heat and water and the transfer of shortwave (SWR) and longwave radiation (LWR) to the snow surface (Jonas & Essery, 2011). The existence of trees decelerates wind and interferes with the turbulence exchange of heat and moisture at the snow surface. Trees shade the snow surface from SWR (Hardy et al., 2004; Malle et al., 2019) and canopy litter on the snow surface absorb higher amounts of incoming SWR (Perrot et al., 2011). Additionally, the trees are emitters of LWR, thereby enhancing incoming LWR to the snow surface relative to non-forested areas (Hedstrom & Pomeroy, 1998a; Webster et al., 2016). All these processes are strongly influenced by the local canopy structure and therefore feature complex spatiotemporal dynamics (Clark et al., 2011; Jonas & Essery, 2011). Within alpine regions, forest structure impacts on snow cover dynamics are superimposed by respective topographic effects. Therefore, the interplay of forest structure and topography must be considered for snow models

to be suitable for application in Alpine countries such as Switzerland. Hence, there is a need to understand snow cover dynamics in forested slopes to develop, validate and improve existing models for these environments (Mazzotti et al., 2019a; Clark et al., 2011).

Snow mapping in Alpine and especially in steep terrain is challenging due to difficult accessibility, avalanche danger, and the frequency of rough weather conditions. Traditional in situ measurements, either manually acquired or from automatic weather stations, are largely limited to flat terrain and only representative of point locations (Bründl et al., 2004; Egli, 2008). This circumstance has triggered significant interest in modern remote sensing technologies for mapping snow distribution over continuous, large, and difficult to access areas (Kim et al., 2017). However, for snow depth mapping within forests, the use of remote sensing technology is currently still mostly limited to Light detection and ranging (LiDAR) (Mazzotti et al., 2019a; Broxton et al., 2015; Currier & Lundquist, 2018; Zheng et al., 2016; Currier et al., 2019), while other sensors (e.g. optical) cannot "see" below the canopy. The potential of LiDAR for capturing fine-scale snow patterns within forests of different canopy types and structures has previously mainly been explored and demonstrated based on Airborne Laser Scanning (ALS) data (Hopkinson et al., 2004; Currier et al., 2019; Deems et al., 2013). As an active scanning technology that operates at high frequency, where each laser pulse has a very small footprint, LiDAR can penetrate even small canopy gaps. Moreover, given its ability to record multiple returns per shot, LiDAR provides information from the canopy itself as well as from the below-canopy ground surface. These characteristics make it an ideal technology to explore how snow patterns relate to canopy structure. However, one of the major drawbacks of ALS is the fact that data acquisitions come with high costs and logistic efforts, therefore on-demand campaigns at high temporal resolution are often unfeasible. Additionally, some remaining data gaps in sub-canopy areas have been reported (Mazzotti et al., 2019a; Broxton et al., 2015; Currier & Lundquist, 2018; Zheng et al., 2016; Currier et al., 2019). These errors are enhanced by terrain-related factors such as the slope and by the presence of understory vegetation (Deems et al., 2013; Hyyppä et al., 2005; Su & Bork, 2006; Tinkham et al., 2012, Hopkinson et al., 2004). They are further influenced by survey parameters, including scanning angle, pulse density, pulse size (footprint), or the operational flying height (Deems et al., 2013; Goodwin et al., 2006; Tinkham et al., 2012). Many forests in alpine regions are located on slopes, because land-use practices have led to deforestation in most flat areas (Bebi et al., 2017). Weaknesses in ALS from crewed aircraft in collecting snow depth datasets is an impediment to the improvement of the understanding of snow cover dynamics in alpine forests.

In contrast to crewed aircraft, UAVs are cheaper and more flexible options. They enable data acquisition at higher temporal resolutions and much lower costs, however, the spatial extent they can cover is more limited. So far, UAVs have been widely used with optical sensors to map snow in open areas using photogrammetric techniques (structure from motion) for mapping snow in high resolutions (Bühler et al., 2016; Vander Jagt et al., 2015; Avanzi et al., 2018). The studies yielded satisfactory results in the open but were unable to obtain accurate below-canopy information. For forest snow mapping, UAV-borne LiDAR is a promising technology, combining the flexibility of UAVs and the capabilities of LiDAR systems. Yet, the use of UAV-borne LiDAR is only emerging: Until now,

only three studies using this technology to investigate forest snow have been conducted (Harder et al., 2020; Jacobs et al., 2021; Cho et al., 2021), none of which is focused on steep terrain.

In fact, only a few studies on forest snow on steep slopes are available to date. Ellis et al. (2011) used a manually acquired dataset with high temporal resolution but only presented data from one individual site. The study exclusively focused on the snowmelt period and did not cover accumulation dynamics. Broxton et al. (2020) presented a larger dataset obtained with ALS over steep terrain, but with limited temporal resolution. Other studies investigating the relation between snow pattern evolution and canopy structure were either based on data from terrestrial laser scanners (Hojatimalekshah et al., 2021**;** Uhlmann et al., 2018**;** Zheng et al., 2018) or ALS **(**Mazzotti et al., 2019a; Moeser et al., 2020**;** Broxton et al., 2015**;** Trujillo et al., 2007) and were largely limited to flat forests.

This paper presents a study conducted in the European Alps, which is to the best of our knowledge the first that explores the use of repeated UAV-borne LiDAR acquisitions to investigate the full seasonal cycle of snow cover dynamics in forested slopes. The goal was to obtain a high-resolution time series of snow depth maps on two opposing (north and south-exposed) slopes and analyze these in the context of variable forest structure to characterize the snow cover dynamics of a typical alpine forest. Given the limited community experience with UAV-borne LiDAR applications, we further report our experiences with this technology, building on the insights of Harder et al. (2020) and Jacobs et al. (2021) aiming at facilitating the use of this novel technology for future snow studies in areas where forest cover and complex terrain overlap.
We present datasets acquired throughout one winter in Davos, Switzerland, focusing our analysis on:

- A comparison of the snow accumulation and melt dynamics between the two opposing slopes.
- The links between snow depth distribution canopy structure descriptors as well as topographic influences in steep forested slopes.
- Evaluation of the UAV-borne LiDAR technology for mapping forest snow in complex terrain at high spatio-temporal resolution.

3.2 Data

3.2.1 Study sites

Data were collected over two forested slopes with opposing orientations in Davos Dorf, in the Swiss Alps. The south-exposed site, Wariwald, is exposed to direct insolation throughout the whole winter season. The other site, Abiwald, is oriented towards the North and thus predominately shaded. The sites are located within 400 m horizontal distance of each other, at approximately 46.810°, 9.856°, 1650 m.a.s.l. (Figure 10). Each field site encompasses an area of heterogeneous forest of 200 by 200 meters, including both dense canopy and gaps. The average slopes are 20° and 35° for Wariwald and Abiwald, respectively. The dominant tree species is spruce, with few

individual larches. For ease of interpretation, the sites are referred to as Wariwald-sunny and Abiwald-shaded.

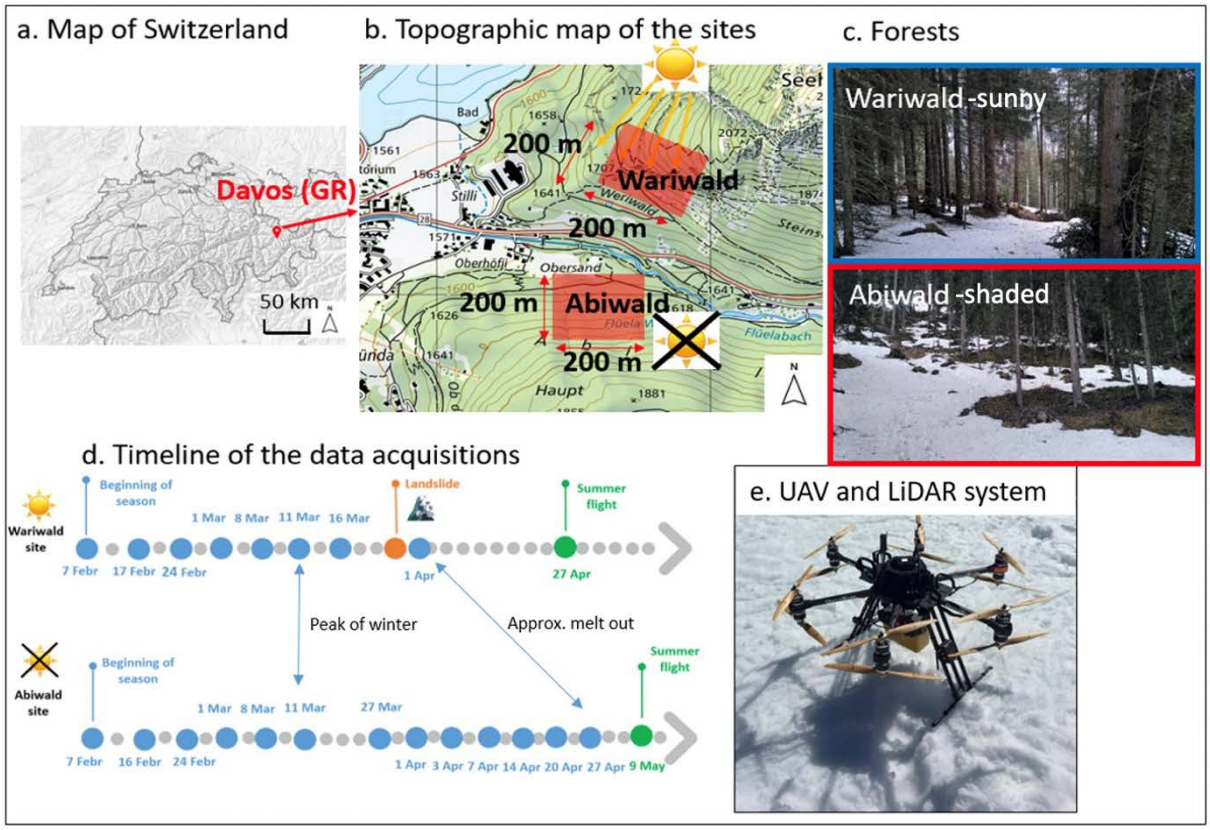

Figure 10: The two forest slopes of our study show a) on the map of Switzerland (source: https://map.geo.admin.ch/) and b) on a topographic map (source: https://map.geo.admin.ch/); c) photographs of the forested slopes; d) timeline of the data acquisitions for both sites; e) UAV system with the LiDAR scanner.

3.2.2 Equipment and LiDAR data acquisition

Data were acquired using a Yellowscan Mapper II LiDAR scanner mounted on a twelve-motor multicopter from Altigator SA. The UAV can lift payload up to 12 kg and maintains stability even during windy conditions. The LiDAR scanner operates in the near-infrared range (905nm). It has field of view of 100°, with about 18500 shots per second and up to three returns per shot with a precision of 10 cm. Its integrated Applanix APX-15 Inertial Navigation System (INS) offers accuracies after post-processing up to 5cm for positioning, 0.015m/sec for velocity, 0.025 degrees for roll and pitch, and 0.080 degrees for true heading. The operation at the specific wavelength of 905 nm is suitable for retrievals of snow, given the high backscattering intensity from the canopies or the snow surface at this wavelength.

The sites were covered with four Interlaced scan patterns consisting of four flight strips each (see Figure 11), the combination of which is hereafter referred to as one acquisition. This acquisition structure was chosen to achieve a high point density, as well as to increase the sub-canopy returns by scanning the same area from different angles. The latter is aimed at increasing the LiDAR returns from the below-canopy areas, especially in the denser parts of the forests. The flight trajectories

were programmed to follow the topography, to ensure a constant elevation of 70-80 meters above ground, at a constant flying speed of 3m/s. These specific survey parameters led to an average return density of 30 points/m^2 per flying pattern.

All the flights were performed during calm weather conditions and minimal wind to reduce power consumption, to allow safe operation of the UAV, and to maximize positioning accuracy by minimizing INS drift. The flight duration was limited to approximately 13 minutes. The relatively short flying time was influenced by the increased power consumption at the high altitude as well as the reduced battery performance at cold temperatures. When possible, data acquisition was restricted to periods without snow intercepted by the canopy to maximize the occurrence of laser pulses penetrating the canopy.

Data acquisition commenced at the beginning of February at both sites when the seasonal snowpack began to build up. It comprised eight winter (hereafter snow-on) acquisitions over Wariwald-sunny and thirteen acquisitions over Abiwald-shaded over the same number of days (i.e. one acquisition at each site per date in Figure **10**). Summer (hereafter snow-off) acquisitions were carried out at the end of April (Wariwald-sunny) and mid-May (Abiwald-shaded). A landslide event at the end of March close to the Wariwald-sunny site inhibited further acquisitions on a regular basis, as permission to access the site was only granted for two more data acquisitions. For this reason, only limited data is available for the final snowmelt period at Wariwald-sunny compared to Abiwald-shaded. Luckily, the dataset still includes acquisitions before, at, and after the peak of winter, allowing the characterization of snow cover dynamics over the season.

3.2.3 Auxiliary data acquisition

Snow depth stakes were established at five locations within each of the field sites to obtain ground truth data for the LiDAR acquisitions. The selection of stake locations was constrained by accessibility, steepness of the terrain, avalanche danger, and the necessity to limit disturbance to the snow surface. Stakes were installed before the first flight in February and removed when the sites became snow-free. Snow depth at all stakes at both sites was recorded on the same day as all winter data acquisitions.

Further auxiliary data was retrieved from the meteorological station of the IMIS network (Interkantonales Mess- und Informationssystem) in Davos and the co-located snow depth measurement site. These data included hourly open-site solar radiation data used for sub-canopy radiation modeling (section 3.3.4), as well as daily snow depth measurements used as open-site reference values.

3.3 Methods

Information on both canopy characteristics and snow distribution can be extracted from LiDAR point clouds. Snow depth maps are obtained by differencing digital elevation models (DEMs) of

snow-off and snow-on acquisitions, while LiDAR returns from vegetation can be rasterized into canopy height models or used as input to radiation transfer models. The following sections outline the workflows applied for these purposes.

3.3.1 UAV-borne LiDAR point cloud data processing

Prior to creating any gridded product, several LiDAR point cloud post-processing steps were required. These included 1) registration workflows to create optimally georeferenced point clouds, and 2) point classification algorithms to allow discriminating between snow/ground and vegetation points, used to derive the snow depths and canopy structure datasets, respectively.

3.3.1.1 Post-Processing Kinematic correction and point cloud registration

The position and attitude recordings of the INS were merged with the raw LiDAR returns and processed to georeferenced point clouds within the licensed CloudStation software (YellowScan Version 1.18.0, 2021). To further improve the positioning accuracy, the flight trajectory was post-processed using the data of a Global Navigation Satellite System (GNSS) base station from the continuously operating reference stations (CORS) of the Swiss positioning system (SWIPOS). The base station chosen was within approximately 1km of the two sites. This post-processing kinematic (PPK) correction was performed using the third-party licensed software POSPac UAV (Applanix, Version 8.3, 2019). The outcome of the PPK correction was the post-processed Smoothed Best Estimate Trajectory (SBET) that was then used for improving the geolocation of the point clouds.
The SBET-based correction of point clouds was assessed based on the alignment accuracy of the four strips for each individual scan, as illustrated in Figure 11. For further improving alignment accuracy where necessary, we applied a manual strip adjustment workflow to neighboring strips as follows: A vertical profile in the overlapping area of the point clouds corresponding to the two strips (e.g. the orange and green lines in Figure 11a) was considered, and one was manually registered to the other to minimize offsets between the two, where the latter one remained static as reference. The 3D transformation matrix derived from this manual registration was then applied to the whole strip.

The next step was the registration of all the four scans into one point cloud. Each individual LiDAR scan includes inaccuracies that might generate from GPS or INS drifts, the PPK correction, or during the manual adjustment of the strips of each scan. The resulting geolocation errors should be minimized by the registration of the individual scans. We applied the same manual adjustment workflow as for the strips' registration, now using the whole scans instead of individual strips. The result was one combined point cloud for each data acquisition. These combined point clouds featured return densities of approximately 120 pts / m2. The snow-on and snow-off point clouds were not fully registered to each other, despite the numerous registration algorithms we tested (see Discussions section). However, the misalignments between snow-on and snow-off point clouds were minimized through the previous steps and further fine-tuning of the so-far alignment procedure was not considered beneficial at this point.

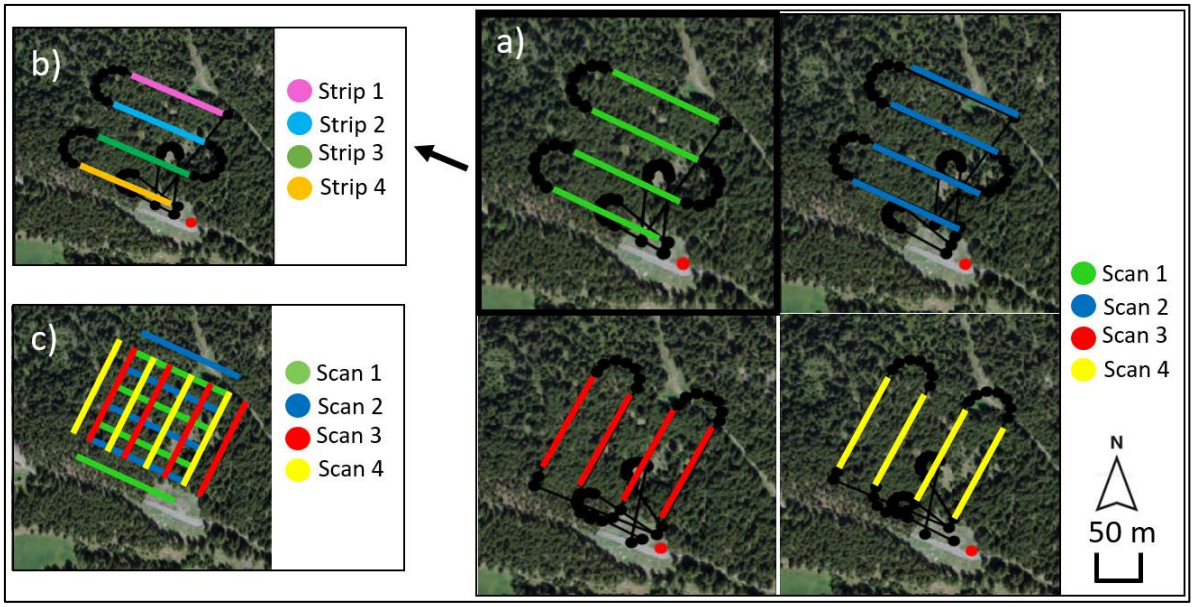

Figure 11: Illustration of the scans and strips designed for Wariwald-sunny field site: interlaced scans (a), 4 strips of one of the scans (b), and all the four interlaced scans for one data acquisition (c).

3.3.1.2 Point cloud classification

The classification of each of the LiDAR point clouds into ground and non-ground points is an essential prerequisite for deriving any gridded product from the point clouds. In our case, this classification served to discriminate between returns from the snow or bare-earth surface (in snow-on and snow-off acquisitions, respectively), and returns from the vegetation (understory and trees). For snow mapping studies, a robust ground point classification is especially critical, as errors will translate into inaccuracies in snow depths. However, forested slopes represent a particularly challenging terrain for classification algorithms, as elevation differences between neighboring points can occur either because the ground is sloped, or because they belong to different classes (snow/ground or vegetation).

We used the lasground tool from LAStools software (Licensed Academic Version 190812, 2019) that classifies points into ground and non-ground points. The most satisfying results, based on visual inspection, were obtained with the settings “step = 3m” and “offset = 1m” (for both sites). To account for any remaining noise within the classified point clouds, we performed additional filtering using the lasthin tool (LAStools). In the case of snow-on acquisition, we kept “snow points” that were between the 50th and 60th percentiles of all elevation values within a 20 cm by 20 cm horizontally moving window, similar to the approach applied in Mazzotti et al. (2019a).

In the case of the snow-off point clouds, the main challenge was the separation between bare-earth and understory vegetation points (Riaño et al., 2007; Spaete et al., 2011; Streutker & Glenn, 2006). Understory vegetation at our sites consisted mainly of tall grasses and blueberry bushes, which are completely buried and pushed down by the snow and hence do not represent an issue during winter acquisition. However, in the case of snow-off flights, returns from understory vegetation are possible and could be misclassified as ground points, resulting in an overestimation of the elevation of the bare earth surface, and an eventual underestimation of the snow depths

(Currier et al., 2019; Hopkinson et al., 2004; Tinkham et al., 2012). To minimize the occurrence of such artifacts, we slightly adapted the filtering with the lasthin tool, keeping "ground" points that were between the 40th and 50th percentiles of all elevation values within a 20 cm by 20 cm horizontally moving window.

The classified point clouds obtained with the above workflow constituted the basis for extracting snow depth grids (Figure 12/section 3.3.2), as well as for producing the canopy height models and corresponding canopy structure descriptor derivatives (Figure 13/section 3.3.3).

3.3.2 Snow depth data processing

The workflow to obtain snow depth maps is summarized in Figure 12. Following the classification of point clouds, snow or bare-ground returns for each acquisition were rasterized into 1 m DEMs, producing maps of snow depth (snow-on DEMs) or bare-earth (snow-off DEMs) respectively. We applied the lasgrid tool (LAStools) to every individual snow-on and snow-off point cloud, where each pixel in the DEM was calculated as the average elevation of all points contained within that pixel. The resulting grids contained gaps corresponding to the below-canopy areas where no returns were captured.

To fill these gaps, we applied the procedure suggested by Mazzotti et al. (2019a) which relies on the las2dem tool from LAStools. This tool triangulates LiDAR returns by using a temporary triangulated irregular network (TIN) and then rasterizes the TIN into a grid of 1m resolution. During the TIN creation, all triangles bigger than 10 meters were discarded and these areas remained as gaps in the final DEMs. Subsequently, the las2dem-derived DEMs were used to fill the gaps in the lasgrid-derived DEMs. To remove the high-frequency noise present in the DEMs, we smoothed the DEMs by applying a 3 by 3 kernel low-pass filter.

Snow depth grids were calculated by differencing each snow-on DEM to the relevant snow-off DEM. The TIN-based gap-filling process of the DEMs led to a small number of artifacts that could be detected as unrealistic snow depth values in the snow depth grids. We removed these by masking out the snow depth pixels with values higher than 1.5 m and lower than -0.5 m to minimize these artifacts. The upper limit was chosen since no accumulation higher than 1.5m was observed at our field sites. The remaining negative snow depth values (-0.5 – 0 m) were not removed at this stage.

Because our sites lacked permanently snow-free areas that could have served as zero snow depth reference, snow depths measured at the five stakes following each data acquisition flight were used as a final step to calibrate the snow depth raster datasets. We calculated a bulk calibration offset for each snow depth grid by averaging the difference between the in-situ snow depths measured on the snow stakes and the LiDAR-derived snow depth values at the same pixel locations.

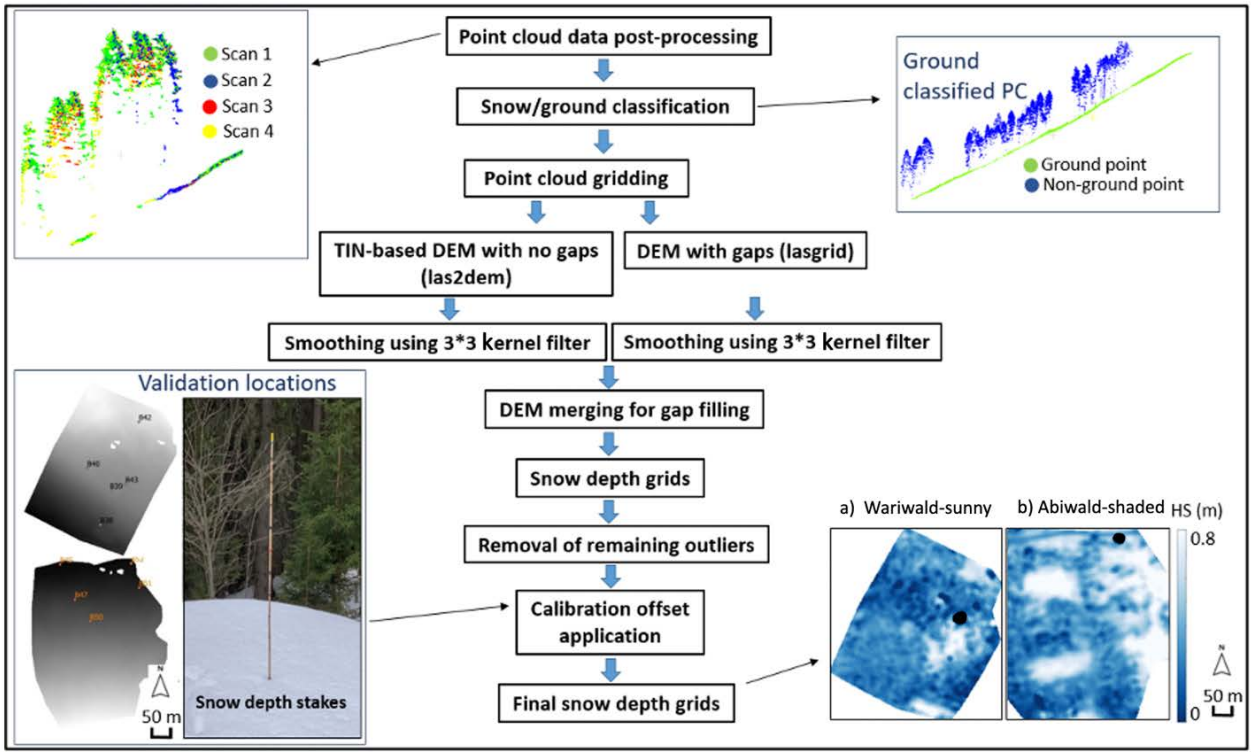

Figure 12: Workflow to obtain snow depth maps from the raw INS data and the LiDAR returns.

3.3.3 Canopy structure data processing

The snow-off point clouds were used to create 1 m resolution canopy height models for both sites. To this end, the snow-off point clouds were first height-normalized then rasterized by the maximum normalized z-value of all the points within each 1m pixel. The resulting canopy height model was further converted into a binary canopy map, where all pixels with canopy height >= 2 m were considered canopy pixels and all pixels with canopy height < 2 m were considered non-canopy pixels. This binarization threshold is consistent with existing literature (Mazzotti et al., 2019; Currier & Lundquist, 2018; Harpold et al., 2014) and was found to be sufficient for filtering understory vegetation. The binary canopy map provided the basis for the extraction of further canopy descriptors used in this study (see Figure 13). We focus our analysis on canopy descriptors that characterize the local canopy structure, especially the canopy density around each pixel. The motivation for this choice is that local canopy density exerts a primary control on the amount of snow intercepted by the canopy, and, consequently, on snow accumulation patterns below the canopy (Broxton et al., 2015; Moeser, et al., 2015; Moeser et al., 2020).

3.3.3.1 Distance from canopy edge (DCE)

The Distance to Canopy Edge (DCE, Mazzotti et al., 2019a) algorithm was used to delineate different regions within the site, representing different small-scale canopy structure categories. The DCE algorithm is an edge-detection routine, which is applied on a binary canopy map. It outputs a map at the same resolution as the binary canopy height model, where every pixel is given the value of its distance to the nearest canopy edge (DCE), with negative values denoting values inside the

canopy and positive values denoting values outside the canopy, respectively (Figure 13). The DCE maps were used to define five canopy structure classes characterizing the forest stand as follows: under canopy, far from edge; under canopy, near edge; at canopy edge; canopy gap, near edge; and canopy gap, far from edge. The corresponding DCE thresholds are reported in Figure 13.

3.3.3.2 Canopy closure (CC)

Canopy closure (CC), defined as the percentage of canopy pixels divided by the total number of pixels around a specific pixel location within a given radius, quantifies the vertical projection of canopy cover around a point. It was derived to provide a spatially continuous quantitative measure of local canopy density at each point within the site. It is thus a second canopy descriptor, which complements the categorical DCE-based classes. In the context of this study, a radius of 5m was chosen to compute CC (Figure 13), since this metric was shown to have the highest spatial correlation with forest snow depth in an earlier study conducted at nearby sites with heterogeneous canopy structures (Mazzotti et al., 2020a). We chose CC as a simple and established canopy structure metric that is linked to process variability across our sites, such as the interception of snow in the canopy. It should be noted that an analogous analysis in forests with mixed species (evergreen and broadleaf) may have required the use of more sophisticated metrics (including canopy height and/or foliage density).

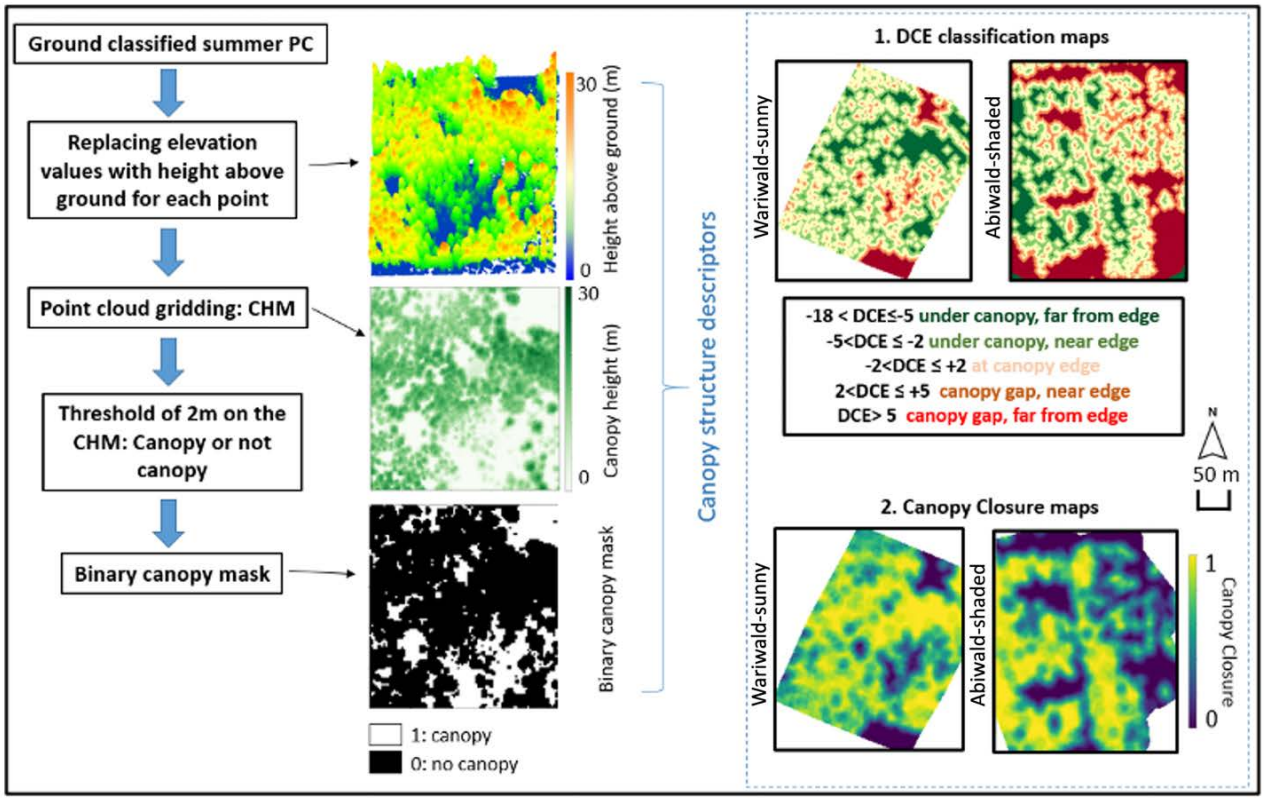

Figure 13: Workflow illustrating the steps for the extraction of the canopy height models from the snow-off point clouds (left) as well as the two canopy structure descriptors that were estimated from the canopy height models (right).

3.3.4 Radiation modeling

To explore the links between snow distribution and ablation processes, we further assessed sub-canopy irradiance patterns at our sites. Sub-canopy SWR and LWR are the two main drivers of snowmelt in forests, and both feature strong spatio-temporal variability (Lundquist et al., 2013b; Musselman et al., 2015). The spatial distribution of sub-canopy incoming LWR is mainly dictated by sky-view fraction (V_f), which determines the patterns of LWR enhancement by the trees relative to above-canopy incoming LWR (Mazzotti et al., 2019b; Webster et al., 2017). Sub-canopy incoming LWR patterns are thus approximately constant in time. In contrast, SWR transmission is a highly complex three-dimensional process, where sub-canopy incoming SWR at any location depends on the (changing) position of the sun relative to the overhead canopy (Jonas et al., 2020; Webster et al., 2020). While V_f (and therefore incoming LWR) is itself correlated to CC (Moeser et al., 2015), incoming SWR is not. For this reason, it was of particular interest for this study to investigate the complex spatiotemporal structure of SWR input to the snow surface at our sites, in addition to CC.

SWR was assessed by applying the radiation modeling workflow described in Webster et al. (2020). This radiation model computes V_f and direct-pulse transmissivity (τ_{dir}) at each modeled location based on synthetic hemispherical images derived from LiDAR using the method from Jonas et al. (2020). Incoming SWR at a point is controlled by all canopy and terrain within a 180° hemispherical view and can be influenced by canopy up to 100 m away (Moeser et al., 2015), and terrain up to 10 km away. To include all canopy and terrain influences on measured snow depth within the field areas, the radiation model was run using ALS data collected in 2017 (Mazzotti et al., 2019a). A visual comparison between the 2017 data and the point clouds collected in this study showed no changes in canopy structure between the two data acquisitions. The model included both canopy and terrain effects on SWR transmission.

Total sub-canopy incoming SWR is given by the sum of above-canopy direct and diffuse SWR components multiplied by τ_{dir} and V_f, respectively. We used the open-site SWR data recorded at the Davos meteorological station (section 3.2.3) as a proxy for the above-canopy SWR. To partition the total above-canopy incoming solar radiation into diffuse and direct components, we used the scheme presented in Erbs et al. (1982), which estimates this partitioning based on atmospheric transmissivity. The calculation of the atmospheric transmissivity requires the solar zenith angle, which we computed with the parameterization developed by NOAA (https://www.esrl.noaa.gov/gmd/grad/solcalc/calcdetails.html).

Total sub-canopy SWR was calculated at every pixel and for hourly timesteps between December 1st 2019 and the end of our observation period. Additionally, the cumulative SWR input between the beginning of December and each flight date was computed. The workflow is shown in Figure **14**, yielding cumulative sub-canopy SWR input maps at 1m resolution for both sites and each data acquisition date. Note that our approach only allowed to infer the spatio-temporal variability of incoming radiation components, contrary to studies such as Mall et al. (2019) and Hotovy and Jenicek (2020) who were able to quantify net radiative fluxes owing to the measurement of the

upwelling radiation components. Such data were unavailable at our site; analysis of spatio-temporal variation in net snowpack energy fluxes was thus beyond the scope of this study.

3.4 Results

3.4.1 Snow depth maps accuracies

Manually measured and LiDAR-derived snow depths were compared and the coefficients of determination (R^2) were calculated for both sites separately, before and after the implementation of the calibration offset (Figure 15a and b). Based on these graphs, a systematic bias can be excluded and mismatches between the manual measurements and the LiDAR data mainly attributed to noise. The match between the manual measurements and the LiDAR data was quantified in terms of root mean squared error (RMSE) for all the dates. The RMSE fluctuates between 5-17 cm and 5-10 cm for Wariwald-sunny and 5-21 cm and 4-20 cm for Abiwald-shaded before and after applying the calibration offset (Figure 15c). The average RMSEs for all the dates presented in Figure **15**c is 13 cm and 11 cm for Abiwald-shaded and 11 cm and 8 cm for Wariwald-sunny (before/after the calibration offset). The comparison of the RMSE values for both sites reveals that in Wariwald-sunny the accuracies are higher than in Abiwald-shaded. This is in accordance to the expected increased vertical biases of a LiDAR system in steeper terrain since Abiwald-shaded is steeper than Wariwald-sunny on average. Note that data acquired at Abiwald-shaded on the 3rd and 27th of April had to be discarded from our analysis due to an unacceptable level of noise despite following the workflow outlined in section 3.3.1.

3.4.2 Spatio-temporal snow distribution dynamics relative to canopy structure

This section relates snow distribution patterns to the canopy structure at the two sites. In the first sub-section, snow depth distribution is qualitatively compared to the canopy height models. In the second sub-section, a more quantitative exploration of snow depth evolution in the context of the DCE-based canopy classes is presented.

3.4.2.1 Qualitative overview of snow depth pattern evolution

Figure 16 presents the snow depth patterns at the two sites for three representative dates corresponding to roughly the beginning (7th February) and the end of the accumulation phase (i.e. peak of winter, 11th March), and the middle of the ablation phase (1st of April). The canopy height models of the two sites are displayed for reference. Overall, these data reveal that the highest snow depths were consistently found in forest gaps, while snow amounts in the below- and close-to-canopy areas were generally lower. The snow depths reached their highest values on the 11th of March for both sites throughout the forest.

However, comparing the two sites also highlights some important differences: The gaps in Abiwald-shaded featured deeper snow depths during the three depicted dates than the gaps in Wariwald-sunny. The gaps in Abiwald-shaded retained snow depths up to 80 cm even at the beginning of

April whereas the snow depths were close to zero under dense canopy. In contrast, gaps at Wariwald-sunny had less snow throughout the season and retained less snow at the beginning of April

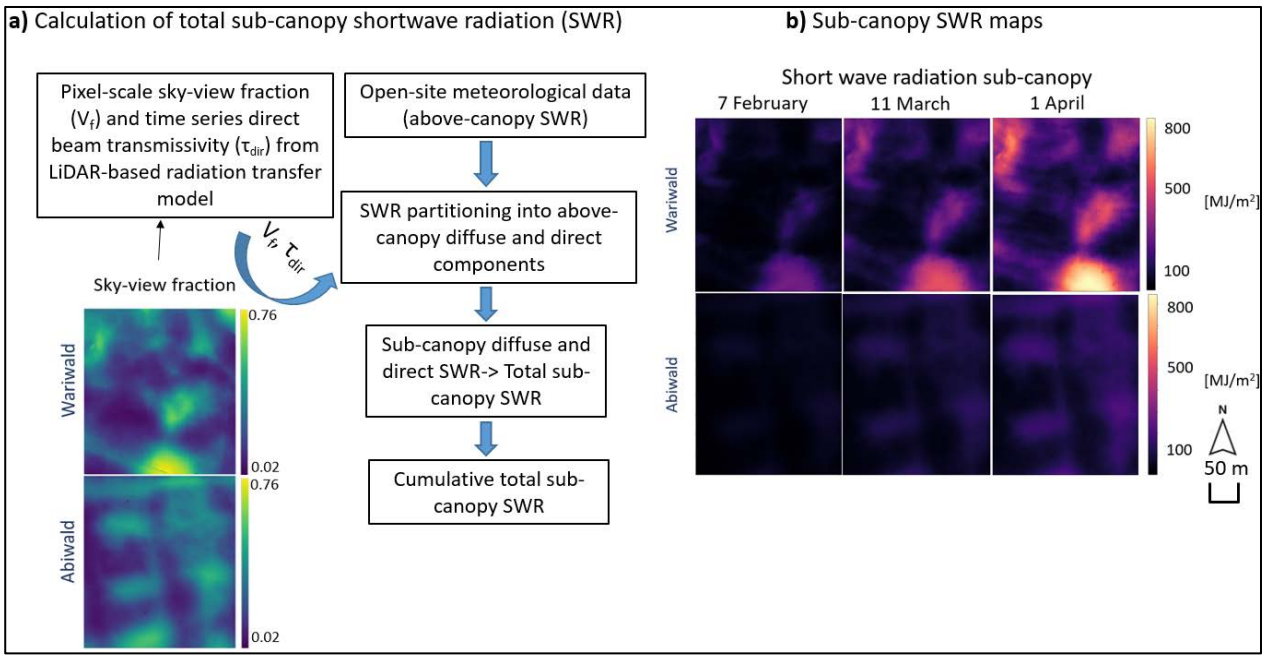

Figure 14: (a) Workflow for the calculation of the incoming sub-canopy cumulative SWR that reaches the snow surface from the 1st of December until each flying date; (b) SWR maps for three representative dates.

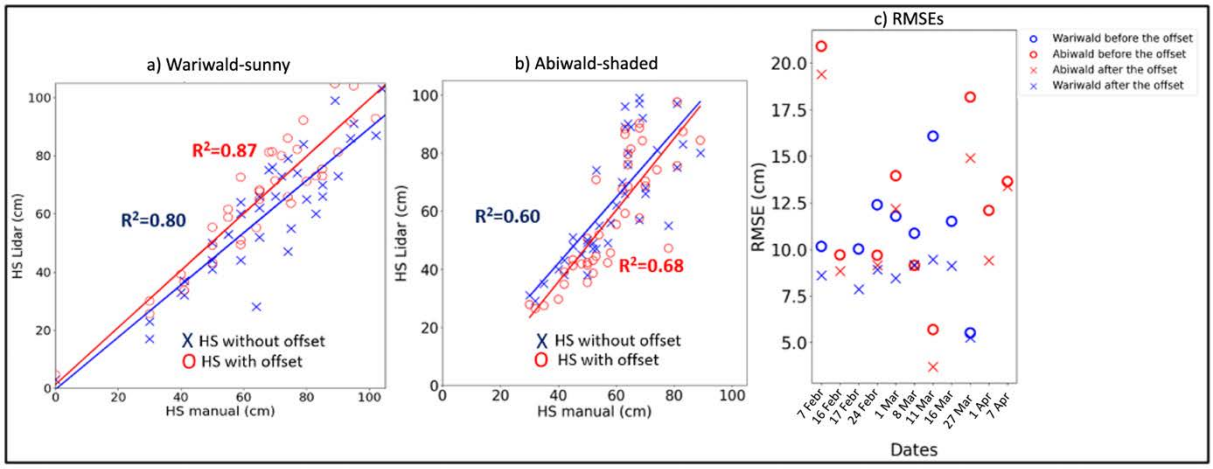

Figure 15: Scatterplots of manual against LiDAR-derived snow depths for Wariwald-sunny (a) and Abiwald-shaded (b); RMSE for all the dates and both sites, after applying the calibration offset on each snow depth grid (c).

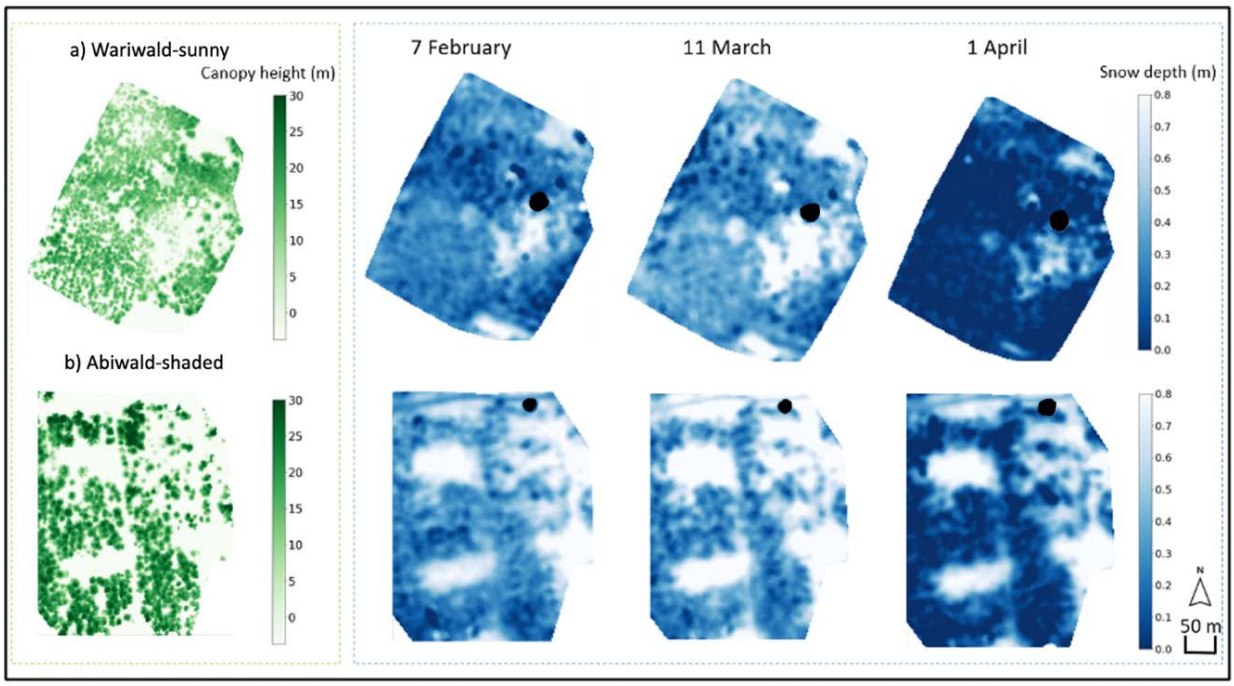

Figure 16: Snow maps for the two sites for three representative dates (right) where black shading denotes no data, and the respective canopy height models (left).

compared to Abiwald-shaded. The snow patterns for the three dates also show that Wariwald-sunny became snow-free earlier than Abiwald-shaded, especially in the areas below canopies which were already almost snow-free at the beginning of April. Notably, the gap on the lower-south part of the forest was almost snow-free by that time as well.

3.4.2.2 Snow depth evolution for the DCE-based classes

For a more quantitative assessment of snow depth dynamics relative to canopy structure, the evolution of the mean snow depth per DCE-based class for both sites is presented in Figure **17**. These plots confirm the general increase in snow depth from dense canopies towards large gaps identified in section 3.4.2.1. Comparing both sites, there was more snow at Abiwald-shaded than at Wariwald-sunny for DCE each class and acquisition, and the differences between the two sites increased throughout the ablation period. In the canopy gaps (see corresponding DCE classes), snow depths did not exceed 70 cm at Wariwald-sunny, with the highest average of the respective classes found on the 11th of March (peak of winter). On the same date, the corresponding mean snow depth value reached almost 1m in the gaps at Abiwald-shaded. During all the dates, the mean snow depths at Wariwald-sunny remained between 20 and 60 cm in the gaps, whereas for all the corresponding dates at Abiwald-shaded the snow depths in the gaps had higher values, between 20-80 cm.

We further observed a different temporal evolution of the mean snow depth per class at the two sites: In Abiwald-shaded the mean snow depth increased steadily from the two under-canopy classes to the gaps away from the canopy edges, and this behavior was consistent throughout the season. Wariwald-sunny showed the same behavior, but in this case, there was no discernible difference in the mean snow depths between the two DCE classes below-canopy and in the gaps.

Furthermore, the data at Wariwald-sunny suggest a faster snow depletion rate in gaps than below canopy right after the peak of snow. As the first acquisitions after peak snow still featured 100% snow coverage, this finding indicates that the slower depletion in areas with, on average, less snow, was not only an effect of partial snow cover.

Mean snow depths for each class at both sites are further compared to the snow depths measured at the reference open site (
Figure **17**; black lines in lower panels). In Wariwald-sunny, the snow accumulation in the open site was almost 20 cm higher than in the gaps. On the contrary, in Abiwald-shaded there was almost the same amount of snow in the gaps compared to the open site during accumulation. After the onset of snowmelt (11th of March onwards), this trend shifted and the canopy gaps at Abiwald-shaded retained, on average, greater snow depths than the open site. Consequently, melt-out at the open site (April 20th) occurred earlier than for any DCE class in Abiwald-shaded, but later than in Wariwald-sunny, which was largely snow-free by that time.

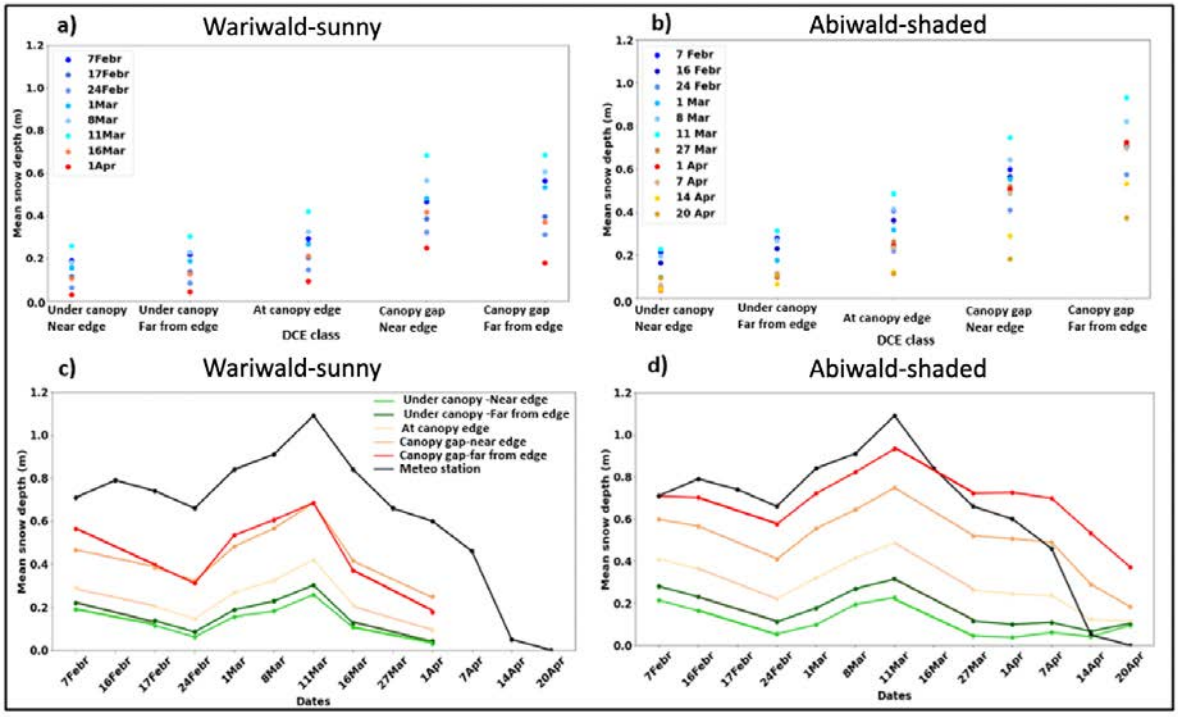

Figure 17: Overview of snow depths per DCE class at the two slopes over the entire season (a and b) and mean snow depths per DCE class for all the dates and both sites (c and d).

3.4.3 Spatio-temporal dynamics of sub-canopy incoming SWR

To provide context to the between-sites differences identified by the results presented in section 3.4.2, this section provides an analysis of sub-canopy incoming SWR dynamics relative to canopy structure at the two sites. Figure 18 presents the evolution of cumulative sub-canopy incoming SWR for both sites. Figure 18a shows the site-averaged snow depth for all flight dates throughout

the whole data acquisition period. The cumulative average sub-canopy SWR input increased steadily over time at both sites, but it is larger for Wariwald-sunny than for Abiwald-shaded for all the dates. While this finding was expected due to the orientation of the two sites, it is worth noting since the average CC at Abiwald-shaded was lower (0.55) than Wariwald-sunny (0.71).

Within-site differences in cumulative incoming sub-canopy SWR are visualized in Figure 18b, expressed as average sub-canopy incoming SWR within each DCE-based class for three representative dates (see Figure 16). All the five different classes at Wariwald-sunny received more SWR than the corresponding classes at Abiwald-shaded, for all three dates. For reference, the class-average of cumulative sub-canopy incoming SWR in the largest gaps at Abiwald-shaded on April 1st was of comparable magnitude to cumulative sub-canopy incoming SWR under the dense canopy at Wariwald-sunny for the same date. At the same time, it was still lower than cumulative sub-canopy incoming SWR for the same canopy class at Wariwald-sunny on February 7th.

Both differences between classes for the same site and between sites for the same class increased over the season, mainly due to increasing cumulative above-canopy incoming SWR. However, due to its exposure to direct insolation, Wariwald-sunny featured a stronger increase in sub-canopy incoming SWR over time than Abiwald-shaded, which resulted in larger between-class differences. At Abiwald-shaded, in contrast, given the lack of direct insolation, the differences between classes only reflected spatial variation in sub-canopy diffuse SWR, which is controlled by V_f. Overall, this analysis illustrates how the controls of terrain (i.e. exposure) on incoming solar radiation to the snow surface can be of similar or larger magnitude as controls exerted by the canopy.

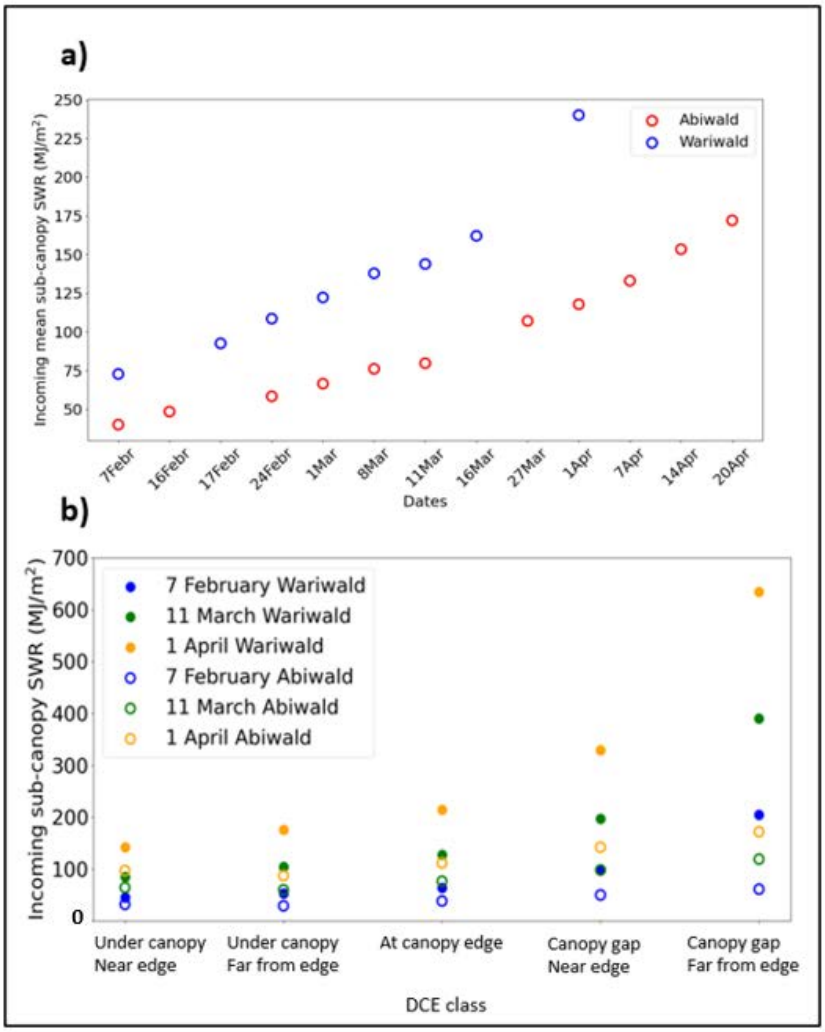

Figure 18: Mean cumulative sub-canopy incoming SWR starting from the 1st of December (a) for all the dates and (b) per DCE class for three representative dates for both sites.

3.4.4 Correlations between snow distribution and local canopy structure

We finally combine findings from sections 3.4.2 and 3.4.3 to explain correlation patterns between snow depth distribution and local canopy structure, and how they varied in time between the two sites. Figure 19a shows the temporal evolution of the correlations between local CC and snow depths, which is further illustrated by the density scatterplots of CC versus snow depth for the three representative dates at both sites (Figure 19c). The evolution of the correlation coefficients is further compared to the evolution of mean snow depth at each site throughout the season (Figure 19b). Two key observations follow from these graphs. Firstly, the negative correlation between local CC and snow depth was consistently stronger for Abiwald-shaded than for Wariwald-sunny: In fact, the Pearson correlation coefficient at Abiwald-shaded reached values around -0.8 for a large part of the season (around -0.85 on the 11th March which was the date with the strongest correlation), while the strongest correlation coefficients varied between -0.6 and -0.7 at Wariwald-sunny. Secondly, this correlation persisted for a longer time at Abiwald-shaded than at Wariwald-sunny. At Abiwald-shaded, correlations were still strong for part of the ablation season and only weakened for the two last campaigns as snow cover started to become partial. In contrast,

the correlation strength deteriorated right at the peak of winter at Wariwald-sunny (R = -0.5 on March 16).

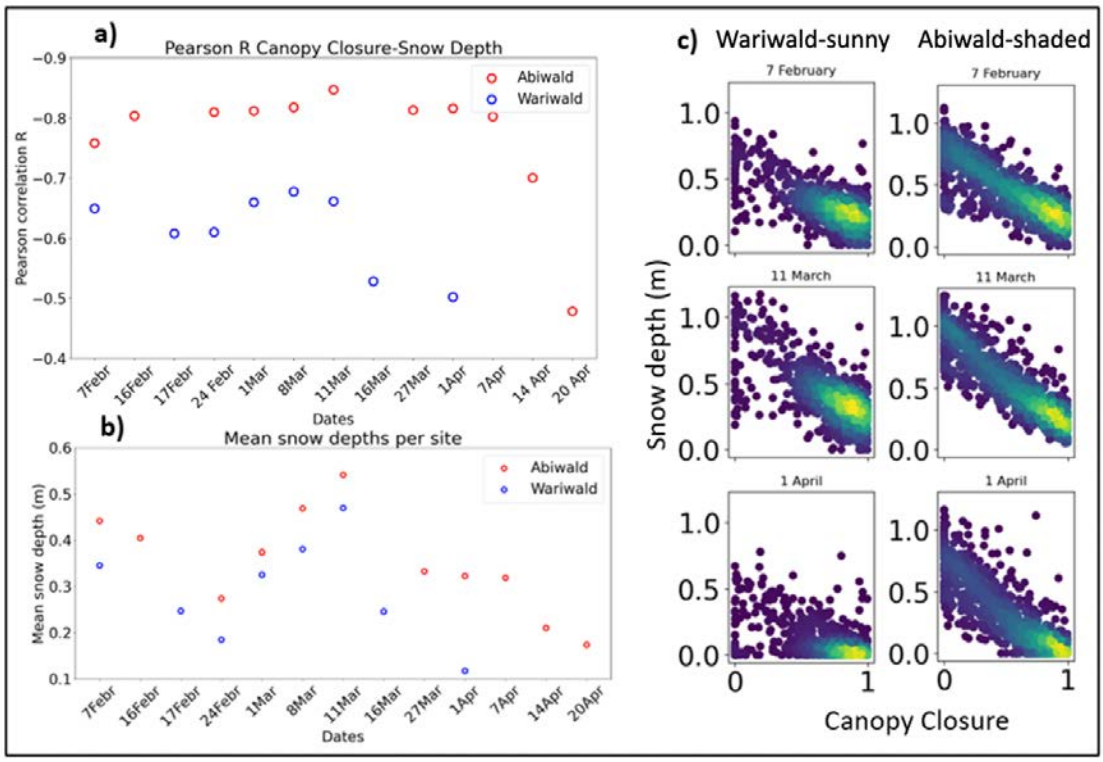

Figure 19: Pearson Correlation coefficient between CC and snow depth in time for both sites (a); Evolution of the mean snow depths per site and for all the dates (b); Density scatterplots between CC and snow depth for three representative dates for both sites (c).

The vertically projected local canopy cover, here quantified by way of CC, is influential to processes driving sub-canopy snow accumulation and depletion dynamics, such as interception/throughfall and LWR. SWR represents an important exception: As a three-dimensional process, its complex spatiotemporal dynamics did not exhibit a direct dependence on a local and purely two-dimensional canopy descriptor. Based on our analyses, we can thus suggest an interpretation of the difference in snow distribution dynamics between the two sites in terms of the varying relative importance of different physical processes at the two sites.

Snow depth distribution early in the snow season was majorly affected by accumulation processes. At our sites, interception patterns were the main driver of snow cover dynamics during this phase, supported by the strongest correlations of snow depth and CC generally occurring during accumulation at both sites. The weaker correlations observed for Wariwald-sunny compared to Abiwald-shaded, however, were likely caused by the different exposure to direct SWR experienced by the two sites. Wariwald-sunny received much more sun already during the accumulation period (see Figure 18), resulting in superimposed interception and insolation patterns at Wariwald-sunny but not at Abiwald-shaded. Additionally, stronger insolation also leads to more settling and/or midwinter melt, which also explains the lower average snow depths at Wariwald-sunny compared to Abiwald-shaded observed already during accumulation.

After the peak of winter, ablation processes can either exacerbate or diminish the initial correlation between snow distribution and local CC, depending on whether or not the ablation patterns themselves are spatially correlated with CC. No precipitation event occurred after March 11th. At Wariwald-sunny the process of insolation that already superimposed the accumulation processes immediately became the dominant control on snow distribution. At Abiwald-shaded, SWR input was likely too weak to disrupt the patterns created by accumulation processes, shown by the continually strong correlations between snow depth and CC into the ablation period. Due to the lack of direct insolation, LWR was likely the main driver of snow ablation at this site.

Overall, these findings reveal a higher complexity of the snow distribution dynamics and its relationship to canopy structure characteristics at Wariwald-sunny. As shown by our analysis, this is linked to the longer and stronger exposure to the sun at this south-exposed side, as this entails the concurrent influence of processes that feature dissimilar canopy structure dependencies throughout the season.

3.5 Discussion

3.5.1 The interplay between canopy structure and topography shapes snow distribution dynamics in forested slopes

The dataset presented in this study allowed a detailed comparison of forest snow dynamics and their spatio-temporal evolution at two opposing slopes using a UAV-borne LiDAR system. Snow cover dynamics were not only linked to a static canopy structure descriptor as in earlier studies (Broxton et al., 2015; Hojatimalekshah et al., 2021; Moeser et al., 2020), but also to detailed sub-canopy SWR. The SWR dynamics at the two slopes exhibited substantial differences due to different topographic shading. Hence, our analysis enabled interesting insights into how topography and canopy structure interact to alter the relative importance of processes shaping snow cover dynamics at opposed slopes. These interactions, in turn, were shown to create distinctly different snow distribution pattern evolution at the two slopes.

The general snow depth decrease from gaps to the dense canopy, which was shown using DCE-based classes, confirming findings of previous studies of Broxton et al. (2015), Mazzotti et al. (2019a), Moeser et al. (2015). However, our data also revealed generally higher mean snow depths in the shaded slope (Abiwald) compared to the sunny slope (Wariwald) throughout the season, particularly in the gaps. The close vicinity of the two sites means that any considerable differences in precipitation input and wind can be excluded, meaning accumulation processes at both sites adhere to the meteorological patterns. With SWR being the only highly variable meteorological input between sites, it is likely that SWR is the main driver of the differences in snow distribution patterns between the two sites. These findings support earlier observations by Golding & Swanson (1986) and Ellis et al. (2011), who established that the snow accumulation in forest clearings is affected by the exposure to solar radiation. Smaller mean snow depths in dense canopy areas than in open areas and accelerated melt at south-exposed forested slopes were also reported by

Cartwright et al. (2020). Broxton et al. (2020), focusing on water equivalent estimations found accumulation around 20-30% higher in gaps than in under-canopy areas and ablation rates at south-exposed slopes increased up to 15-30% relative to the north-exposed slopes. Zheng et al. (2016) found canopy strcuture and topographic characteristics to be relevant explanatory variables of snow distribution, using LiDAR-derived snow depths and regression analysis over a site in the Sierra Nevada. Very recently, the combined impact of canopy structure and topography was evidenced in a study by Safa et al. (2021), who applied machine learning algorithms to several LiDAR-derived snow distribution datasets from the Western US.

Between-site differences throughout the season, illustrated by the different evolutions of the correlations between snow depth and CC at the two sites, demonstrate that discrepancies in snow cover dynamics between slopes of different aspects already build up during the accumulation and not only during the ablation period. This is in line with the study of Grünewald et al. (2010), conducted in open terrain, which showed that areas of different aspects were characterized by different accumulation rates and also had differential depletion over the entire season. Schirmer & Pomeroy (2020) also highlighted that solar irradiance input in areas with different aspects causes different ablation rates and differences in early-season melting. Kostadinov et al. (2019) found higher fractional snow cover for below-canopy areas compared to open areas on south-exposed slopes at high elevation, confirming the dominant role of radiative processes in shaping snow distribution patterns during ablation.

Our results have important implications in the context of forest snow modeling. Latest hyper-resolution models that account for small-scale canopy structure and its influence on accumulation processes and radiation patterns (Broxton et al., 2015; Moeser et al., 2020) should be inherently capable of resolving differences in snow cover dynamics between slopes. However, most models operate at coarser resolution and need to capture variability induced by canopy structure at the sub-grid level, either by parametrizations (Luce & Tarboton, 2004) or sub-tiling schemes (Currier & Lundquist, 2018). As suggested e.g. by Dickerson-Lange et al. (2015) and Mazzotti et al. (2021), sub-grid parametrizations specifically tailored to forested areas should be a priority of future research in the field. Our findings, indicate that such parametrizations would need to incorporate both, canopy structure and topography information, due to the distinct snow distribution patterns created by the two. Forest snow distribution maps as presented in this study could provide the basis for the sub-grid parametrizations, however, it should be kept in mind that the TIN-based gap filling method applied here likely overestimates snow depth under canopies and should be revisited in the context of LiDAR-derived forest snow maps.

While providing meaningful insights, our analysis disregarded some factors that may additionally impact snow distribution patterns. Firstly, it should be pointed out that our findings are specific to the meteorological characteristics typical of our alpine sites. For instance, accumulation patterns were unaffected by wind, due to generally low wind speeds given the location of our sites within larger forest stands (Mazzotti et al., 2020b), as well as relatively warm temperatures during snowfall events leading to limited wind transport (Mott et al., 2018). Studies conducted in colder and windier climates of the Western United States (Currier & Lundquist, 2018; Webb et al., 2020)

have reported substantial snow redistribution by wind, which created accumulation patterns that were not directly linked to CC. Also, the ablation season in our study was characterized by fine weather and long periods of clear sky conditions. Under these conditions, direct solar radiation prevails, maximizing differences due to topography, and the range of LWR enhancement is largest, maximizing the link between LWR-driven ablation and CC (Mazzotti et al., 2019b). Prevalence of cloudy conditions would have shifted the radiation patterns to more homogeneous LWR enhancement and stronger impact of diffuse radiation (i.e. negative correlation to CC). Such meteorological conditions would therefore likely have led to a faster decay of the correlation between snow depth and CC at Abiwald-shaded during the ablation season, and smaller differences between the two sites. Consequently, and as suggested in existing literature (e.g. Mazzotti et al., 2021), any upcoming sub-grid forest snow parametrization should account for different controls relevant in different climates, and only be applied in the context of the climatic conditions for which it has been developed.

Secondly, and also as pointed out in previous literature, micro-topography (Hopkinson et al., 2011; Cho et al., 2021), as well as the ground roughness (Lehning et al., 2011; Cho et al., 2021), are additional controls on snow distribution that may confound canopy structure and topography effects. The forest floor at our sites indeed featured a considerable degree of roughness, due to rocks, fallen logs, and shrubs. However, initial attempts to characterize ground roughness from the snow-off LiDAR point cloud were unsuccessful, which hampered us from investigating its influence on snow cover dynamics. Finally, our data was only able to capture snow depth distribution and could not resolve spatial differences in snow density, which does exhibit considerable variability in forests (Broxton et al., 2020; Raleigh & Small, 2017). While still providing insightful findings of the relative importance of different processes, our study cannot offer a full assessment of canopy and topographic impacts on snow water resources in terms of snow water equivalent. Canopy-class-specific snow density surveys at the two slopes would have been a useful complement to our dataset for this purpose. Unfortunately, accessibility restrictions made such efforts unfeasible.

3.5.2 Technical challenges, lessons learned, and recommendations for future UAV-borne LiDAR forest snow studies in steep slopes

The flexibility and the cost-effectiveness of UAVs make them an attractive tool for snow distribution surveying at high spatio-temporal resolutions. Given the unique assets of UAV-borne LiDAR compared to other platforms (e.g. LiDAR from crewed aircraft or UAV-borne optical sensors), it is a suitable choice for snow mapping studies on forested slopes. While a thorough accuracy assessment of this technology was beyond the scope of this study, the comparison against ground truth data (section 3.4.1) suggests that measurement errors were in the same order of magnitude as those observed for ALS-based studies in flat forests (Currier et al., 2019; Mazzotti et al., 2019a; Harder et al., 2020; Jacobs et al., 2021). However, our experience revealed that UAV-borne LiDAR technology is not straightforwardly applicable and that it comes with many challenges related both to the field data acquisition and the subsequent data processing. Specific challenges we faced are discussed below followed by recommendations for future applications of this promising technology.

The LiDAR-integrated INS proved to have operational difficulties, which became evident when analyzing misalignments between strips that persisted even after the PPK corrections. This could have been due to a changing flying height along the individual flight lines, which was implemented to maintain a fixed height above the terrain. Since no such difficulties were encountered with the same system when maintaining a constant flying height above flat terrain (see Koutantou et al., 2021), we conclude that higher-grade INS may be beneficial for such terrain-following applications for surveying in steep terrain.

The return density of 30 pts/m^2 granted by our LiDAR system is sufficient for resolving forest snow patterns at the meter scale and was comparable to other studies investigating snow depth distribution with ALS data (e.g. 18 pt/m^2 in Currier et al. (2019), 5-30 pt/m^2 in Mazzotti et al. (2019a) and 10-15 pt/m^2 in Broxton et al. (2020)). However, occlusion turned out to be a limiting factor. Despite the manufacture-stated ability to record up to three returns per pulse, an inspection of our datasets revealed that most pulses yielded one return only, which meant that oftentimes the LiDAR pulse did not manage to penetrate the canopy. The overlapping flight patterns that yielded point densities of around 120 pts/m^2 were designed to compensate for this circumstance and allowed us to restrict data gaps below the canopy to an acceptable level. However, this required strategy substantially reduced the area we could cover with our set of batteries. The resulting trade-off between spatial extent covered and point density achieved may have been avoided with a different LiDAR system, e.g. a system able to output the full waveform data to allow identifying even weak returns, e.g. such as the system used by Harder et al. (2020). Considering the amount of data gaps below dense canopy areas we still faced despite the high point densities reached by overlapping flight plans, we strongly advocate a careful choice of LiDAR system and survey parameters for forest snow studies, as these have different data requirements than typical applications of LiDAR. High pulse frequency, small pulse divergence and multi-angular scanning, as well as the possibility to post-process full waveform data would improve the concurrent capture of both canopy and the below-canopy surface. Where data gaps cannot be avoided, more sophisticated gap filling algorithms could be explored to avoid the likely overestimation of snow depth caused by the TIN-based gap-filling method used here. While already suggested by Mazzotti et al. (2019), the enhancement of this algorithm was beyond the scope of this study as it would require substantially more ground validation measurements.

The manual registration adjustment procedure we had to apply to compensate for a lack of positioning accuracy of the INS is not considered part of a standard processing workflow. In fact, such a step is not reported by either Jacobs et al. (2021), Harder et al. (2020) or Cho et al. (2021). Yet, it was indispensable in our case, as misalignment issues and data gaps not only affected the accuracy of our data but substantially inhibited the application of subsequent processing algorithms. As discussed in detail in Koutantou et al. (2021) numerous existing algorithms were unsuccessfully tested prior to adopting the manual registration workflow. A major limitation to the use of these algorithms was the lack of stable objects at our sites that could have been used as tie points in feature-based registration algorithms. Since our acquisitions only occurred in the absence of wind and snow intercepted in the canopies, we even tested the use of treetops as stable features

within our sites, as proposed by Ferraz et al. (2018), but failed to extract a global rotation and translation matrix applicable to the whole point cloud.

A large set of Ground Control Points (GCPs) would have facilitated the registration procedures. We strongly recommend that future forest snow studies involve permanently installed GCPs that are evenly distributed across the site, to allow minimizing geolocation errors homogeneously across the entire point cloud. Snow depth measurements on the GCPs could be also useful for the validation of the snow depth maps. As with the GCPs, an even distribution of the validation stakes across the sites is recommended (Bühler et al., 2015, 2016; Vander Jagt et al., 2015; Avanzi et al., 2018). This was not possible at our sites due to accessibility issues; disturbance of the snow surface needed to be minimized, and especially at Abiwald-shaded, accessibility was only granted at the lower end of the slope for avalanche safety reasons. An alternative solution could be the placement of stakes with cameras oriented towards them to avoid necessitating direct access to them on each campaign day. Where snow-free areas are present, a combination of the LiDAR datasets with optical imagery could be used to delineate these for later use to facilitate the registration of snow-on and snow-off point clouds, as in the workflow applied by the Airborne Snow Observatory (Painter et al., 2016). Snow-free features could also provide a more robust validation target than point measurements from snow stakes.

3.6 Conclusions

This study presented, for the first time, an analysis of spatio-temporal snow dynamics in two heterogeneous forests on slopes of opposing aspects, based on repeated UAV-borne LiDAR surveys. Snow depth maps at 1m resolution derived from the point clouds were analyzed in conjunction with canopy structure information and detailed maps of sub-canopy incoming shortwave radiation obtained with a LiDAR-based radiation transfer model.

Analysis of co-registered snow and canopy structure data revealed a strong correlation between spatial patterns of snow depth and local canopy closure early in the season. This correlation was stronger and persisted longer for the north-exposed site, but was weaker and decayed immediately after the peak of winter at the south-exposed site. The temporal evolution of the correlation between snow depth and local canopy closure suggests that at the shaded slope, snow distribution patterns were mainly governed by interception patterns formed during accumulation, and were not significantly altered during ablation. These consistent snow depth distribution patterns through the ablation period suggest longwave radiation was the dominant radiation flux at the shaded site. In contrast, direct insolation was the dominant radiation flux at the south-exposed slope, and its complex spatio-temporal patterns lead to snow distribution dynamics that exhibit a less well-defined link to the local structure throughout the ablation period.

These findings corroborate the complexity of the snow processes in forests and the important role both local canopy cover and topography play in shaping them. Approaches to parametrize the sub-

grid variability of forest snow in coarse-resolution models will thus need to account for both, and such approaches must be tested in a variety of topographic settings and meteorological conditions. In general, the UAV-borne LiDAR system proved efficient in mapping snow cover dynamics with a high spatial and temporal resolution. However, we identified technical challenges specific to applying this technology to forested slopes. Future application of UAV-borne LiDAR to snow studies in forested complex terrain should carefully consider system specifications and the use of GCPs to facilitate subsequent data processing. Concurrent acquisition of snow density measurements would further allow extending this snow depth-based analysis to snow water equivalent in view of a more accurate quantification of snow water resources.

Acknowledgments

The UAV and LiDAR systems were funded by the Swiss National Science Foundation (SNF, project 206021_170753). Kalliopi Koutantou and Philip Brunner were supported by the University of Neuchatel, Giulia Mazzotti, Clare Webster and Tobias Jonas by WSL/SLF. The authors would like to thank the Snow Hydrology team from SLF for their assistance in the field whenever needed, as well as the members of the electronics team from SLF that were assisting with the UAV technical issues. The acquisition of LiDAR and validation data would not have been possible without the help of Laurent Fasnacht and Eliane Brändle, for assisting with the UAV flight plans and for being the main copilot during the UAV flights, respectively. Finally, the authors would like to thank two anonymous reviewers and the editors for their constructive comments.

References

Applanix. (2019). POSPac UAV, Version 8.3, licensed

Avanzi, F., Bianchi, A., Cina, A., De Michele, C., Maschio, P., Pagliari, D., Passoni, D., Pinto, L., Piras, M., & Rossi, L. (2018). Centimetric Accuracy in Snow Depth Using Uncrewed Aerial System Photogrammetry and a MultiStation. *Remote Sensing*, 10(5), 765. https://doi.org/10.3390/rs10050765

Baltsavias, E. P. (1999). Airborne laser scanning: Basic relations and formulas. *ISPRS Journal of Photogrammetry and Remote Sensing*, 54(2–3), 199–214. https://doi.org/10.1016/S0924-2716(99)00015-5

Bebi, P., Seidl, R., Motta, R., Fuhr, M., Firm, D., Krumm, F., Conedera, M., Ginzler, C., Wohlgemuth, T., & Kulakowski, D. (2017). Changes of forest cover and disturbance regimes in the mountain forests of the Alps. *Forest Ecology and Management*, 388, 43–56. https://doi.org/10.1016/j.foreco.2016.10.028

Björk, R. G., & Molau, U. (2007). Ecology of Alpine Snowbeds and the Impact of Global Change. *Arctic, Antarctic, and Alpine Research*, 39(1), 34–43. https://doi.org/10.1657/1523-0430(2007)39[34:EOASAT]2.0.CO;2

Broxton, P. D., Harpold, A. A., Biederman, J. A., Troch, P. A., Molotch, N. P., & Brooks, P. D. (2015). Quantifying the effects of vegetation structure on snow accumulation and ablation in mixed-conifer forests. *Ecohydrology*, *8*(6), 1073–1094. https://doi.org/10.1002/eco.1565

Broxton, P. D., Leeuwen, W. J. D., & Biederman, J. A. (2020). Forest cover and topography regulate the thin, ephemeral snowpacks of the semiarid Southwest United States. *Ecohydrology*, *13*(4). https://doi.org/10.1002/eco.2202

Bründl, M., Etter, H.-J., Steiniger, M., Klingler, Ch., Rhyner, J., & Ammann, W. J. (2004). IFKIS - a basis for managing avalanche risk in settlements and on roads in Switzerland. *Natural Hazards and Earth System Sciences*, *4*(2), 257–262. https://doi.org/10.5194/nhess-4-257-2004

Bühler, Y., Adams, M. S., Bösch, R., & Stoffel, A. (2016). Mapping snow depth in alpine terrain with uncrewed aerial systems (UASs): Potential and limitations. *The Cryosphere*, *10*(3), 1075–1088. https://doi.org/10.5194/tc-10-1075-2016

Bühler, Y., Marty, M., Egli, L., Veitinger, J., Jonas, T., Thee, P., & Ginzler, C. (2015). Snow depth mapping in high-alpine catchments using digital photogrammetry. *The Cryosphere*, *9*(1), 229–243. https://doi.org/10.5194/tc-9-229-2015

Cho, E., Hunsaker, A. G., Jacobs, J. M., Palace, M., Sullivan, F. B., & Burakowski, E. A. (2021). Maximum entropy modeling to identify physical drivers of shallow snowpack heterogeneity using unpiloted aerial system (UAS) LiDAR. *Journal of Hydrology*, *602*, 126722. https://doi.org/10.1016/j.jhydrol.2021.126722

Clark, M. P., Hendrikx, J., Slater, A. G., Kavetski, D., Anderson, B., Cullen, N. J., Kerr, T., Örn Hreinsson, E., & Woods, R. A. (2011). Representing spatial variability of snow water equivalent in hydrologic and land-surface models: A review: REPRESENTING SPATIAL VARIABILITY OF SWE IN MODELS. *Water Resources Research*, *47*(7). https://doi.org/10.1029/2011WR010745

Currier, W. R., & Lundquist, J. D. (2018). Snow Depth Variability at the Forest Edge in Multiple Climates in the Western United States. *Water Resources Research*, *54*(11), 8756–8773. https://doi.org/10.1029/2018WR022553

Currier, W. R., Pflug, J., Mazzotti, G., Jonas, T., Deems, J. S., Bormann, K. J., Painter, T. H., Hiemstra, C. A., Gelvin, A., Uhlmann, Z., Spaete, L., Glenn, N. F., & Lundquist, J. D. (2019). Comparing Aerial LiDAR Observations With Terrestrial LiDAR and Snow-Probe Transects From NASA's 2017 SnowEx Campaign. *Water Resources Research*, *55*(7), 6285–6294. https://doi.org/10.1029/2018WR024533

Deems, J. S., Painter, T. H., & Finnegan, D. C. (2013). LiDAR measurement of snow depth: A review. *Journal of Glaciology*, *59*(215), 467–479. https://doi.org/10.3189/2013JoG12J154

Dickerson-Lange, S. E., Lutz, J. A., Martin, K. A., Raleigh, M. S., Gersonde, R., & Lundquist, J. D. (2015). Evaluating observational methods to quantify snow duration under diverse forest canopies. *Water Resources Research*, *51*(2), 1203–1224. https://doi.org/10.1002/2014WR015744

Egli, L. (2008). Spatial variability of new snow amounts derived from a dense network of Alpine automatic stations. *Annals of Glaciology*, *49*, 51–55. https://doi.org/10.3189/172756408787814843

Ellis, C. R., Pomeroy, J. W., Essery, R. L. H., & Link, T. E. (2011). Effects of needleleaf forest cover on radiation and snowmelt dynamics in the Canadian Rocky Mountains. *Canadian Journal of Forest Research*, *41*(3), 608–620. https://doi.org/10.1139/X10-227

Erbs, D. G., Klein, S. A., & Duffie, J. A. (1982). Estimation of the diffuse radiation fraction for hourly, daily and monthly-average global radiation. *Solar Energy*, *28*(4), 293–302. https://doi.org/10.1016/0038-092X(82)90302-4

Essery, R., Rutter, N., Pomeroy, J., Baxter, R., Stähli, M., Gustafsson, D., Barr, A., Bartlett, P., & Elder, K. (2009). SNOWMIP2: An Evaluation of Forest Snow Process Simulations. *Bulletin of the American Meteorological Society*, *90*(8), 1120–1136. https://doi.org/10.1175/2009BAMS2629.1

Farinotti, D., Usselmann, S., Huss, M., Bauder, A., & Funk, M. (2012). Runoff evolution in the Swiss Alps: Projections for selected high-alpine catchments based on ENSEMBLES scenarios. *Hydrological Processes*, *26*(13), 1909–1924. https://doi.org/10.1002/hyp.8276

Ferraz, A., Saatchi, S., Bormann, K., & Painter, T. (2018). Fusion of NASA Airborne Snow Observatory (ASO) LiDAR Time Series over Mountain Forest Landscapes. *Remote Sensing*, *10*(2), 164. https://doi.org/10.3390/rs10020164

Golding, D. L., & Swanson, R. H. (1986). Snow distribution patterns in clearings and adjacent forest. *Water Resources Research*, *22*(13), 1931–1940. https://doi.org/10.1029/WR022i013p01931

Goodwin, N. R., Coops, N. C., & Culvenor, D. S. (2006). Assessment of forest structure with airborne LiDAR and the effects of platform altitude. *Remote Sensing of Environment*, *103*(2), 140–152. https://doi.org/10.1016/j.rse.2006.03.003

Grünewald, T., Schirmer, M., Mott, R., & Lehning, M. (2010). Spatial and temporal variability of snow depth and ablation rates in a small mountain catchment. *The Cryosphere*, *4*(2), 215–225. https://doi.org/10.5194/tc-4-215-2010

Harder, P., Pomeroy, J. W., & Helgason, W. D. (2020). Improving sub-canopy snow depth mapping with uncrewed aerial vehicles: LiDAR versus structure-from-motion techniques. *The Cryosphere*, *14*(6), 1919–1935. https://doi.org/10.5194/tc-14-1919-2020

Hardy, J. P., Melloh, R., Koenig, G., Marks, D., Winstral, A., Pomeroy, J. W., & Link, T. (2004). Solar radiation transmission through conifer canopies. *Agricultural and Forest Meteorology*, *126*(3), 257–270. https://doi.org/10.1016/j.agrformet.2004.06.012

Harpold, A. A., Guo, Q., Molotch, N., Brooks, P. D., Bales, R., Fernandez-Diaz, J. C., Musselman, K. N., Swetnam, T. L., Kirchner, P., Meadows, M. W., Flanagan, J., & Lucas, R. (2014). LiDAR-derived snowpack data sets from mixed conifer forests across the Western United States. *Water Resources Research*, *50*(3), 2749–2755. https://doi.org/10.1002/2013WR013935

Hedstrom, N. R., & Pomeroy, J. W. (1998). Measurements and modelling of snow interception in the boreal forest. *Hydrological Processes*, *12*(10–11), 1611–1625. https://doi.org/10.1002/(SICI)1099-1085(199808/09)12:10/11<1611::AID-HYP684>3.0.CO;2-4

Hojatimalekshah, A., Uhlmann, Z., Glenn, N. F., Hiemstra, C. A., Tennant, C. J., Graham, J. D., Spaete, L., Gelvin, A., Marshall, H.-P., McNamara, J. P., & Enterkine, J. (2021). Tree canopy and snow depth relationships at fine scales with terrestrial laser scanning. *The Cryosphere*, 15(5), 2187–2209. https://doi.org/10.5194/tc-15-2187-2021

Hopkinson, C., Sitar, M., Chasmer, L., & Treitz, P. (2004). Mapping Snowpack Depth beneath Forest Canopies Using Airborne LiDAR. Photogrammetric Engineering & Remote Sensing, 70(3), 323–330. https://doi.org/10.14358/PERS.70.3.323

Hopkinson, Chris & Pomeroy, John & Debeer, C. & Anderson, Axel. (2012). Relationships between snowpack depth and primary LiDAR point cloud derivatives in a mountainous environment. *IAHS Publications*. 352, 2012. 352. 354-358.

Hotovy, O., Jenicek, M. (2020). The impact of changing subcanopy radiation on snowmelt in a disturbed coniferous forest. *Hydrological Processes, 34*, 5298-5314. https://doi.org/10.1002/hyp.13936

Hunziker, M., von Lindern, E., Bauer, N., Frick, J. (2012). Das Verhältnis der Schweizer Bevölkerung zum Wald. Waldmonitoring soziokulturell: Weiterentwicklung und zweite Erhebung – WaMos 2. *Birmensdorf, Eidg. Forschungsanstalt für Wald, Schnee und Landschaft WSL. 180 S.*

Hyyppä, H., Yu, X., Hyyppä, J., Kaartinen, H., Kaasalainen S., Honkavaara, E., Rönnholm, P. (2004). Factors Affecting the Quality of DTM Generation in Forested Areas. *Int. Arch. Photogramm. Remote Sens. Spat. Inf. Sci. 36.*

Jacobs, J. M., Hunsaker, A. G., Sullivan, F. B., Palace, M., Burakowski, E. A., Herrick, C., & Cho, E. (2021). Snow depth mapping with unpiloted aerial system LiDAR observations: A case study in Durham, New Hampshire, United States. The Cryosphere, 15(3), 1485–1500. https://doi.org/10.5194/tc-15-1485-2021

Javadinejad, S., Dara, R., & Jafary, F. (2020). Climate Change Scenarios and Effects on Snow-Melt Runoff. Civil Engineering Journal, 6(9), 1715–1725. https://doi.org/10.28991/cej-2020-03091577

Jonas, T., & Essery, R. (2011). Snow cover and snowmelt in forest regions. In V. P. Singh, P. Singh, & U. K. Haritashya (Eds.), Encyclopedia of Earth Sciences Series. Encyclopedia of Snow, Ice and Glaciers (pp. 1033-1036). https://doi.org/10.1007/978-90-481-2642-2_499. 4

Jonas, T., Webster, C., Mazzotti, G., & Malle, J. (2020). HPEval: A canopy shortwave radiation transmission model using high-resolution hemispherical images. *Agricultural and Forest Meteorology, 284*, 107903. https://doi.org/10.1016/j.agrformet.2020.107903

Kostadinov, T.S., Schumer, R., Hausner, M., Bormann, K. J., Gaffney, R., McGwire, K., Painter, T. H., Tyler, S., Harpold, A. A. (2019). Watershed-scale mapping of fractional snow cover under conifer forest canopy using LiDAR, *Remote Sensing of Environment*, *222,* 34-49. https://doi.org/10.1016/j.rse.2018.11.037

Koutantou, K., Mazzotti, G., & Brunner, P. (2021). UAV-BASED LIDAR HIGH-RESOLUTION SNOW DEPTH MAPPING IN THE SWISS ALPS: COMPARING FLAT AND STEEP FORESTS*. The International Archives of the Photogrammetry, Remote Sensing and Spatial Information Sciences, XLIII-B3-2021*, 477–484. https://doi.org/10.5194/isprs-archives-XLIII-B3-2021-477-2021

LAStools, academic version 190812, 2019, licensed

Luce, C. H., & Tarboton, D. G. (2004). The application of depletion curves for parameterization of subgrid variability of snow. *Hydrological Processes*, *18*(8), 1409–1422. https://doi.org/10.1002/hyp.1420

Lundquist, J. D., Dickerson-Lange, S. E., Lutz, J. A., & Cristea, N. C. (2013b). Lower forest density enhances snow retention in regions with warmer winters: A global framework developed from plot-scale observations and modeling: Forests and Snow Retention. *Water Resources Research*, *49*(10), 6356–6370. https://doi.org/10.1002/wrcr.20504

MacKay, M. D., & Bartlett, P. A. (2006). Estimating canopy snow unloading timescales from daily observations of albedo and precipitation. *Geophysical Research Letters*, *33*(19). https://doi.org/10.1029/2006GL027521

Malle, J., Rutter, N., Mazzotti, G., & Jonas, T. (2019). Shading by Trees and Fractional Snow Cover Control the Subcanopy Radiation Budget. *Journal of Geophysical Research: Atmospheres*, *124*(6), 3195–3207. https://doi.org/10.1029/2018JD029908

Mazzotti, G., Currier, W. R., Deems, J. S., Pflug, J. M., Lundquist, J. D., & Jonas, T. (2019a). Revisiting Snow Cover Variability and Canopy Structure Within Forest Stands: Insights From Airborne LiDAR Data. *Water Resources Research*, *55*(7), 6198–6216. https://doi.org/10.1029/2019WR024898

Mazzotti, G., Malle, J., Barr, S., & Jonas, T. (2019b). Spatially Continuous Characterization of Forest Canopy Structure and Subcanopy Irradiance Derived from Handheld Radiometer Surveys. *Journal of Hydrometeorology*, *20*(7), 1417–1433. https://doi.org/10.1175/JHM-D-18-0158.1

Mazzotti, G., Essery, R., Moeser, C. D., & Jonas, T. (2020a). Resolving Small-Scale Forest Snow Patterns Using an Energy Balance Snow Model With a One-Layer Canopy. *Water Resources Research*, *56*(1). https://doi.org/10.1029/2019WR026129

Mazzotti, G., Essery, R., Webster, C., Malle, J., & Jonas, T. (2020b). Process-Level Evaluation of a Hyper-Resolution Forest Snow Model Using Distributed Multisensor Observations. *Water Resources Research*, *56*(9), e2020WR027572. https://doi.org/10.1029/2020WR027572

Mazzotti, G., Webster, C., Essery, R., & Jonas, T. (2021). Increasing the Physical Representation of Forest-Snow Processes in Coarse-Resolution Models: Lessons Learned From Upscaling Hyper-Resolution Simulations. *Water Resources Research*, *57*(5). https://doi.org/10.1029/2020WR029064

Moeser, C. D., Broxton, P. D., Harpold, A., & Robertson, A. (2020). Estimating the Effects of Forest Structure Changes From Wildfire on Snow Water Resources Under Varying Meteorological Conditions. *Water Resources Research*, *56*(11). https://doi.org/10.1029/2020WR027071

Moeser, D., Stähli, M., & Jonas, T. (2015). Improved snow interception modeling using canopy parameters derived from airborne LiDAR data. *Water Resources Research*, *51*(7), 5041–5059. https://doi.org/10.1002/2014WR016724

Mott, R., Vionnet, V., & Grünewald, T. (2018). The Seasonal Snow Cover Dynamics: Review on Wind-Driven Coupling Processes. *Frontiers in Earth Science*, *6*, 197. https://doi.org/10.3389/feart.2018.00197

Musselman, K. N., Pomeroy, J. W., & Link, T. E. (2015). Variability in shortwave irradiance caused by forest gaps: Measurements, modelling, and implications for snow energetics. *Agricultural and Forest Meteorology*, *207*, 69–82. https://doi.org/10.1016/j.agrformet.2015.03.014

Nöthiger, C., & Elsasser, H. (2004). Natural Hazards and Tourism: New Findings on the European Alps. *Mountain Research and Development*, *24*(1), 24–27. https://doi.org/10.1659/0276-4741(2004)024[0024:NHATNF]2.0.CO;2

Painter, T. H., Berisford, D. F., Boardman, J. W., Bormann, K. J., Deems, J. S., Gehrke, F., Hedrick, A., Joyce, M., Laidlaw, R., Marks, D., Mattmann, C., McGurk, B., Ramirez, P., Richardson, M., Skiles, S. M., Seidel, F. C., & Winstral, A. (2016). The Airborne Snow Observatory: Fusion of scanning LiDAR, imaging spectrometer, and physically-based modeling for mapping snow water equivalent and snow albedo. *Remote Sensing of Environment*, *184*, 139–152. https://doi.org/10.1016/j.rse.2016.06.018

Perrot, D., Pugh, E., Molotch, N., & Small, E. (2011). Effects of forest litter and aeolian dust deposition on snow surface albedo. *AGU Fall Meeting Abstracts*, 0458

Raleigh, M. S., & Small, E. E. (2017). Snowpack density modeling is the primary source of uncertainty when mapping basin-wide SWE with LiDAR. *Geophysical Research Letters*, *44*(8), 3700–3709. https://doi.org/10.1002/2016GL071999

Riaño, D., Chuvieco, E., Ustin, S. L., Salas, J., Rodríguez-Pérez, J. R., Ribeiro, L. M., Viegas, D. X., Moreno, J. M., & Fernández, H. (2007). Estimation of shrub height for fuel-type mapping combining airborne LiDAR and simultaneous color infrared ortho imaging. *International Journal of Wildland Fire*, *16*(3), 341. https://doi.org/10.1071/WF06003

Rixen, C., Teich, M., Lardelli, C., Gallati, D., Pohl, M., Pütz, M., & Bebi, P. (2011). Winter Tourism and Climate Change in the Alps: An Assessment of Resource Consumption, Snow Reliability, and Future Snowmaking Potential. *Mountain Research and Development*, *31*(3), 229–236. https://doi.org/10.1659/MRD-JOURNAL-D-10-00112.1

Safa, H., Krogh, S. A., Greenberg, J., Kostadinov, T. S., & Harpold, A. A. (2021). Unraveling the controls on snow disappearance in montane conifer forests using multi-site LiDAR. *Water Resources Research, 57*, e2020WR027522. https://doi.org/10.1029/2020WR027522

Schirmer, M., & Pomeroy, J. W. (2020). Processes governing snow ablation in alpine terrain – detailed measurements from the Canadian Rockies. *Hydrology and Earth System Sciences*, *24*(1), 143–157. https://doi.org/10.5194/hess-24-143-2020

Spaete, L. P., Glenn, N. F., Derryberry, D. R., Sankey, T. T., Mitchell, J. J., & Hardegree, S. P. (2011). Vegetation and slope effects on accuracy of a LiDAR-derived DEM in the sagebrush steppe. *Remote Sensing Letters*, *2*(4), 317–326. https://doi.org/10.1080/01431161.2010.515267

Streutker, D. R., & Glenn, N. F. (2006). LiDAR measurement of sagebrush steppe vegetation heights. *Remote Sensing of Environment*, *102*(1), 135–145. https://doi.org/10.1016/j.rse.2006.02.011

Su, J., & Bork, E. (2006). Influence of Vegetation, Slope, and LiDAR Sampling Angle on DEM Accuracy. *Photogrammetric Engineering & Remote Sensing*, *72*(11), 1265–1274. https://doi.org/10.14358/PERS.72.11.1265

Thornton, J. M., Brauchli, T., Mariethoz, G., & Brunner, P. (2021). Efficient multi-objective calibration and uncertainty analysis of distributed snow simulations in rugged alpine terrain. *Journal of Hydrology*, *598*, 126241. https://doi.org/10.1016/j.jhydrol.2021.126241

Tinkham, W. T., Smith, A. M. S., Hoffman, C., Hudak, A. T., Falkowski, M. J., Swanson, M. E., & Gessler, P. E. (2012). Investigating the influence of LiDAR ground surface errors on the utility of derived forest inventories. *Canadian Journal of Forest Research*, *42*(3), 413–422. https://doi.org/10.1139/x11-193

Trujillo, E., Ramírez, J. A., & Elder, K. J. (2007). Topographic, meteorologic, and canopy controls on the scaling characteristics of the spatial distribution of snow depth fields: SPATIAL SCALING OF SNOW DEPTH. *Water Resources Research*, *43*(7). https://doi.org/10.1029/2006WR005317

Uhlmann, Z., Glenn, N. F., Spaete, L. P., Hiemstra, C., Tennant, C., & McNamara, J. (2018). Resolving the Influence of Forest-Canopy Structure on Snow Depth Distributions with Terrestrial Laser Scanning. *IGARSS 2018 - 2018 IEEE International Geoscience and Remote Sensing Symposium*, 6284–6286. https://doi.org/10.1109/IGARSS.2018.8517911

Vander Jagt, B., Lucieer, A., Wallace, L., Turner, D., & Durand, M. (2015). Snow Depth Retrieval with UAS Using Photogrammetric Techniques. *Geosciences*, *5*(3), 264–285. https://doi.org/10.3390/geosciences5030264

Webb, R. W., Raleigh, M. S., McGrath, D., Molotch, N. P., Elder, K., Hiemstra, C., Brucker, L., & Marshall, H. P. (2020). Within-Stand Boundary Effects on Snow Water Equivalent Distribution in Forested Areas. *Water Resources Research*, *56*(10), e2019WR024905. https://doi.org/10.1029/2019WR024905

Webster, C., Rutter, N., Zahner, F., & Jonas, T. (2016). Modeling subcanopy incoming longwave radiation to seasonal snow using air and tree trunk temperatures: MODELING SUBCANOPY LONGWAVE RADIATION. *Journal of Geophysical Research: Atmospheres*, *121*(3), 1220–1235. https://doi.org/10.1002/2015JD024099

Webster, C., Rutter, N., & Jonas, T. (2017). Improving representation of canopy temperatures for modeling subcanopy incoming longwave radiation to the snow surface. *Journal of Geophysical Research: Atmospheres*, *122*(17), 9154–9172. https://doi.org/10.1002/2017JD026581

Webster, C., Mazzotti, G., Essery, R., & Jonas, T. (2020). Enhancing airborne LiDAR data for improved forest structure representation in shortwave transmission models. *Remote Sensing of Environment*, *249*, 112017. https://doi.org/10.1016/j.rse.2020.112017

Wipf, S., Stoeckli, V., & Bebi, P. (2009). Winter climate change in alpine tundra: Plant responses to changes in snow depth and snowmelt timing. *Climatic Change*, *94*(1–2), 105–121. https://doi.org/10.1007/s10584-009-9546-x

YellowScan CloudStation. (2021). Version 1.18.0, licensed

Zheng, Z., Kirchner, P. B., & Bales, R. C. (2016). Topographic and vegetation effects on snow accumulation in the southern Sierra Nevada: A statistical summary from LiDAR data. *The Cryosphere*, *10*(1), 257–269. https://doi.org/10.5194/tc-10-257-2016

Zheng, Z., Ma, Q., Qian, K., & Bales, R. (2018). Canopy Effects on Snow Accumulation: Observations from LiDAR, Canonical-View Photos, and Continuous Ground Measurements from Sensor Networks. *Remote Sensing*, *10*(11), 1769. https://doi.org/10.3390/rs1011

4. Validation of NASA Sea Surface Temperature Satellite Products using Saildrone data

Publication:
Koutantou, K., Brunner, P., & Vazquez-Cuervo, J. Validation of NASA Sea Surface Temperature Satellite Products using Saildrone data. *Remote Sens. 2023, 15*, 2277. https://doi.org/10.3390/rs15092277

Abstract

Sea Surface Temperature (SST) is at the core of many processes in the oceans. Various remote sensing platforms have been used to obtain SST products of different scales, but their validation remains a topic of ongoing research. One promising platform is an uncrewed surface vehicle called Saildrone. We use the data from the 8 Saildrone deployments of the 2019 West Coast campaign to validate MODIS level-2 and Multi-scale Ultra-high Resolution (MUR) level-4 satellite SST products at 1km spatial resolution and to assess the robustness of the quality levels of MODIS level-2 products over the California Coast. Pixel-based SST comparisons between Saildrone and the satellite products were performed, as well as thermal gradient comparisons computed both at the pixel-base level and using kriging interpolation. The results generally showed better accuracies for the MUR products. The characterization of the MODIS quality level proved to be valid in areas covered by bad-quality MODIS pixels but less valid in areas covered by lower-quality pixels. The latter implies possible errors in the MODIS quality level characterization and MUR interpolation processes. We have demonstrated the ability of the Saildrones to accurately validate nera-shore satellite SST products and provide important information for the quality assessment of satellite products.

4.1. Introduction

The sea surface temperature (SST) is a key state variable for studying and predicting the interaction between the ocean and the atmosphere (O'Carroll et al., 2019) and an indicator of global climate change [2–4]. Its accurate mapping is critical for the understanding of ocean phenomena such as coastal upwelling, which is characterized by spatial thermal gradients. The ability to extract accurate SST and its gradients is essential for the study of coastal processes (Vazquez-Cuervo et al., 2023) and a better understanding of the mesoscale and sub-mesoscale coastal dynamics (Gruber et al., 2011). Satellites offer the opportunity to map SST at large scales. Compared to in situ measurements, they provide better spatial coverage of the ocean SST (Cao et al., 2021). However, the coarse spatiotemporal resolution of the available satellite data may not be adequate for small-scale assessments of ocean phenomena. In addition, coastal areas are often covered by clouds

resulting in data gaps within the satellite data, so full spatial coverage is not available. For many applications, the data gaps have to be interpolated, increasing the uncertainty of the final satellite product. The problem of cloud cover in coastal areas is dominant in our study area, the California Coast (Clemesha et al., 2016; Iacobellis and Cayan, 2013). In California, the term June Gloom is used to describe the cloudy, overcast sky and the cool temperatures of late spring and early summer (en.wikipedia.org/wiki/June_Gloom).

Satellite SST data are provided to the users with quality flags for each pixel, typically based on a quality assessment of the atmospheric correction, atmospheric conditions at the time of acquisition, cloud cover, etc. These quality flags are used to set the quality levels on a scale from 0 to 4 or 5. Zero indicates a complete failure or masked pixel and the highest number indicates the best quality that a pixel can have within the SST product (https://oceancolor.gsfc.nasa.gov/atbd/sst/flag/). These per-pixel quality levels are also provided to the users within the SST product. The quality levels are very important as they are used to indicate which pixel will be used for the next processing step up to the extraction of the final SST gridded product (level-4).

Therefore, the validation of satellite-derived SST products in terms of assessing their quality levels is of critical importance. The extent to which the available satellite data can contribute to our understanding of coastal processes depends on the quality of the satellite products and the reliability of the quality flags.

Many satellites map SST at different spatial resolutions (1-25 km) using thermal infrared bands (Minnett et al., 2019). The most commonly used infrared sensors for SST are the Visible Infrared Imaging Radiometer Suite (VIIRS) instrument onboard the NOAA/NASA Suomi NPP satellite, the Moderate Resolution Imaging Spectroradiometer (MODIS) onboard the NASA Earth Observing System (EOS) Terra and Aqua satellites, the Advanced Very High-Resolution Radiometer (AVHRR) on NOAA's Polar-orbiting Operational Environmental Satellites (POES), the Along-Track Scanning Radiometer (ATSR) on the European Remote Sensing Satellite (ERS-2) and the Geostationary Operational Environmental Satellite (GOES) Imager. However, these infrared sensors are highly affected by scattering from atmospheric vapor, leading to uncertainties and data gaps in cloud-covered areas (Cao et al., 2021; Guan and Kawamura, 2003; Liu et al., 2017).

Satellite microwave sensors are also used to measure SST (Stammer et al., 2003; Wentz et al., 2000). The microwave sensors record the energy emitted by the atmosphere, reflected or emitted by the ocean, or the radiance transmitted from the subsurface ($SST_{sub\text{-}skin}$), and these data are converted into temperature information. Unlike thermal infrared radiation, longer wavelength microwave radiation can penetrate through clouds, haze, and precipitation**,** providing SST data in all weather conditions and at night. However, the derived spatial resolution is about 25km which may be insufficient to detect submesoscale and mesoscale variability. Some examples of microwave sensors include the Scanning Multichannel Microwave Radiometer (SMMR) carried on the Nimbus-7 and Seasat satellites, the Tropical Rainfall Measuring Mission (TRMM) Microwave Imager (TMI), the Advanced Microwave Scanning Radiometer (AMSR) instrument on the NASA's EOS Aqua satellite and the Japanese Advanced Earth Observing Satellite (ADEOS II). However,

microwave data have coarser spatial resolution and lower accuracy than infrared data, and are also sensitive to surface roughness and precipitation (Alerskans et al., 2020; Gentemann et al., 2010).

In situ measurements to validate satellite products of SST are typically made using buoys (Atkinson et al., 2013; Castro et al., 2016) and Argo floats (Moteki, 2022). However, there are significant practical limitations (Emery et al., 2001; Hansen and Poulain, 1996; Xu and Ignatov, 2014). They only measure at a specific geographic location and they are, therefore, unable to document mesoscale and sub-mesoscale variability (Chin et al., 2017; Xiu et al., 2018). Another difference is that in situ measurements typically measure SST at a depth of a few centimeters below the surface (bulk SST/SST_{depth}), rather than a skin or sub-skin temperature ($SST_{sub\text{-}skin}$), as is the case with thermal infrared and passive microwave sensors, respectively. The differences between SST_{skin} and SST_{bulk} increase under wind-free conditions or when large amounts of incoming solar radiation reach the ocean surface.

As a result, there may be differences between skin temperature and temperatures at several meters depth. These differences should be taken into account when validating satellite measurements derived from either thermal infrared or passive microwave sensors.

A recently developed uncrewed surface vehicle (USV) technology called Saildrone, samples the ocean surface every minute and provides multiple measurements of the ocean surface, including the skin (SST_{skin}) and the SST a few centimeters below the surface (bulk SST or SST_{depth}) (https://www.saildrone.com/). The ability of the Saildrone to sample the ocean surface with high temporal resolution and increased spatial coverage due to its autonomous, rapid navigation allows for a better comparison with satellite data than the traditional in situ measurements mentioned above. Saildrones also allow the extraction of spatial gradients of the ocean parameter of interest due to their high spatiotemporal resolution (Cokelet et al., 2015; Meinig et al., 2019; Mordy et al., 2017).

To observe dynamic coastal phenomena such as the upwelling at small scales, a combination of infrared, microwave, and in situ data is promising. In this context, NASA's Multi-scale Ultra-high Resolution (MUR) SST product of the Group for High-Resolution Sea Surface Temperature (GHRSST) combines data from different sources. The current version of MUR (Version 4.1, http://dx.doi.org/10.5067/GHGMR-4FJ04) combines MODIS SST retrievals at high spatial resolution of about 1 km, Advanced Very High-Resolution Radiometer (AVHRR) infrared SST retrievals at a medium resolution of 4 to 8.8 km, and microwave SST retrievals at a coarser spatial resolution of 25 km. This combination aims to fill the data gaps in areas where only infrared or microwave data are available (Chin et al., 1998). The approach used in the MUR data maximizes the use of the infrared data, where available, from MODIS (level-2 product) and AVHRR. MUR is globally gridded at 1 km resolution and available in daily maps using an objective interpolation technique based on a wavelet decomposition (Chin et al., 1998).

This paper presents a validation of MODIS level-2 (L2P) and MUR level-4 SST products over the California Coast. We also examine the MODIS level-2 quality levels characterization along the

California Coastal region. This is the first study to compare MODIS level-2 (L2P) with MUR level-4 SST products over the California Coast. It is also the first study to attempt to validate MODIS level-2 (L2P) data from a spatio-temporal perspective by applying the different quality levels off the California Coast. MODIS L2P data are the main input for the production of the level-4 gridded SST MUR products and therefore the validation of their quality is crucial. Their quality is documented by the quality levels that have been established during the primary data processing. MUR uses only the MODIS pixels of good-quality (quality level 5). Otherwise, the interpolation to fill the pixels where no MODIS data were found, or where quality level 5 pixels are not available, is done using data of coarser spatial resolution. More specifically, it uses AVHRR data from 4km to 8.8km or microwave data from the Advanced Microwave Scanning Radiometer (AMSR-E), the WindSat Polarimetric Radiometer, and the Advanced Microwave Scanning Radiometer 2 (AMSR2), as well as in situ data (Chin et al., 2017) are used.

Assessing the quality levels of MODIS level-2 data is important because incorrectly characterizing a pixel as ‘‘bad-quality’’ or ‘‘good-quality’’ will lead to incorrect exclusion or inclusion of that particular pixel from the final SST product. In the former case, erroneous exclusion can lead to data interpolation in pixel areas that are not needed, thus reducing the accuracy of the final SST product. The validation of both MODIS level-2 and MODIS level-4 as well as of the quality levels of MODIS level-2 was carried out using the Saildrone data due to its ability to sample the sea surface of coastal areas at high spatial and temporal resolution. Validation was performed at the pixel level. Gradients were also calculated to test the ability of 1km satellite products to correctly estimate thermal gradients. The gradients are of particular importance because of their importance in understanding coastal SST patterns and the associated upwelling phenomena. Despite the rapid coverage of large areas that Saildrones provide, they are often only launched close to the coast. Therefore, the ability to interpolate Saildrone-based SST values in unsampled areas outside the coast can help to validate satellite products over a larger spatial extent. To achieve this, this study used kriging interpolation to predict the Saildrone SST values in unsampled locations, by taking into account the spatial correlation between sampled SST values (Chin et al., 2017).

The choice of the California Coast as the study area was made because it is a highly productive coastal ecosystem due to the California Current (Huyer, 1983; Xiu et al., 2018). Coastal upwelling is the dominant physical phenomenon affecting production in the California Current system. It occurs from April to September when strong northerly winds blow along the Oregon and Washington coasts. This seasonal cold water is associated with high production by phytoplankton, the base of the food chain, attracting large numbers of consumers and leading to one of the most productive fisheries in the world. These fisheries play a key role in the economy and culture of the California Current (https://ecowatch.noaa.gov/regions/california-current).

In this current study, we focus specifically on:

- Per-pixel validation of SST values from satellite products using Saildrone data
- Assessing the quality levels of MODIS level-2 data

- Estimation of the SST gradients using pixel-based and kriging approaches from the Saildrone data and comparison with those estimated directly from the satellite products

In the following sections, we present the methods we used for the SST and gradient validations, as well as a description of the results and discussion in relation to previous studies.

4.2. Study area and data

4.2.1 Study area

The study area covers part of the North Pacific Ocean along the California Coast, from 46.783603, -126.339794 north to 24.178057, -116.711086 south, in geographic coordinates (see Figure 20a). The area includes the coastline from Washington to Baja California, where the dominant coastal upwelling occurs.

4.2.2 In situ measurements

In this study, as a reference for the validation of the satellite products we used the data from the Saildrone USA West Coast 2019 campaign, which integrates eight deployments along the California Coast (see Figure 20c). The USA West Coast 2019 deployment spatially covers the area from 31.78 to 48.5 degrees latitude and -127.62 to -118.36 degrees longitude. Data collection took place from mid-June to mid-September (2019-06-18 to 2019-09-16). The eight Saildrone deployments follow different trajectories between each other, continuously sampling the ocean surface every minute for the entire period between 2019-06-18 to 2019-09-16. We selected only the Saildrone measurements for each deployment corresponding to the dates of 27 and 30 of June, 7th of July, and 11th of August (from 0:00 to 23:59 p.m. for each date), as these are the dates of the satellite data used for this study (see next section).

We used the bulk SST/SST_{depth} measurements at 0.6m below the sea surface level (TEMP_CTD_RBR_MEAN value of SST) because at the time of the current study the Saildrone sensor measuring bulk SST/SST_{depth} has proven to be more accurate than the one measuring SSTskin. The instrumentation on Saildrone is not new technology but is based on the application of standard Conductivity/Temperature/Depth measurements. These instruments have been used extensively in ships, buoys, etc. The infrared radiometers on Saildrone were not used in the study, because there are still calibration issues. Thus, for this study, only the CTD sensors were used. CTD sensors are used on the global ARGO array as a reference for many data sets, including satellite-derived sea surface temperature and salinity (Gentemann et al., 2010).

4.2.3 Satellite Sea Surface Temperature products

We used two different SST satellite products at 1 km spatial resolution over the California Coast for the dates of the 27th and 30th of June, the 7th of July, and the 11th of August 2019, which coincide with the Saildrone data. More specifically, the two datasets used are as follows:

The first dataset is the GHRSST level-2P Global Skin Sea Surface Temperature from the Moderate Resolution Imaging Spectroradiometer (MODIS) on the NASA Aqua satellite. This skin SST product is produced from both day and night observations, derived from the long-wave IR 11- and 12-micron wavelength channels of Aqua MODIS (https://podaac.jpl.nasa.gov/dataset/MODIS_A-JPL-L2P-v2019.0). In addition to the skin SST data, we used the quality level information that accompanies the MODIS level-2P products, which includes information on how good/trustworthy the SST value of each pixel is. Higher values correspond to better-quality pixels. This information is very useful because bad-quality pixels (e.g. cloud covered pixels) are masked out and only the good-quality pixels (quality level 5) are used during the interpolation process to produce the final gridded MUR product (level-4 SST map).

The second dataset is the GHRSST level-4 MUR Global foundation SST product, which combines nighttime GHRSST L2P skin and sub-skin SST observations from several instruments, including the NASA Advanced Microwave Scanning Radiometer-EOS (AMSR-E), the JAXA Advanced Microwave Scanning Radiometer 2 on GCOM-W1, the MODIS on the NASA Aqua and Terra platforms, the US Navy WindSat microwave radiometer, the AVHRR on several NOAA satellites, and in situ SST observations from the NOAA iQuam project (Chin et al., 2017). The iQuam data are used to for bias correction. The level-4 product is a daily global map gridded at 0.01° spatial resolution (https://podaac.jpl.nasa.gov/dataset/MUR-JPL-L4-GLOB-v4.1).

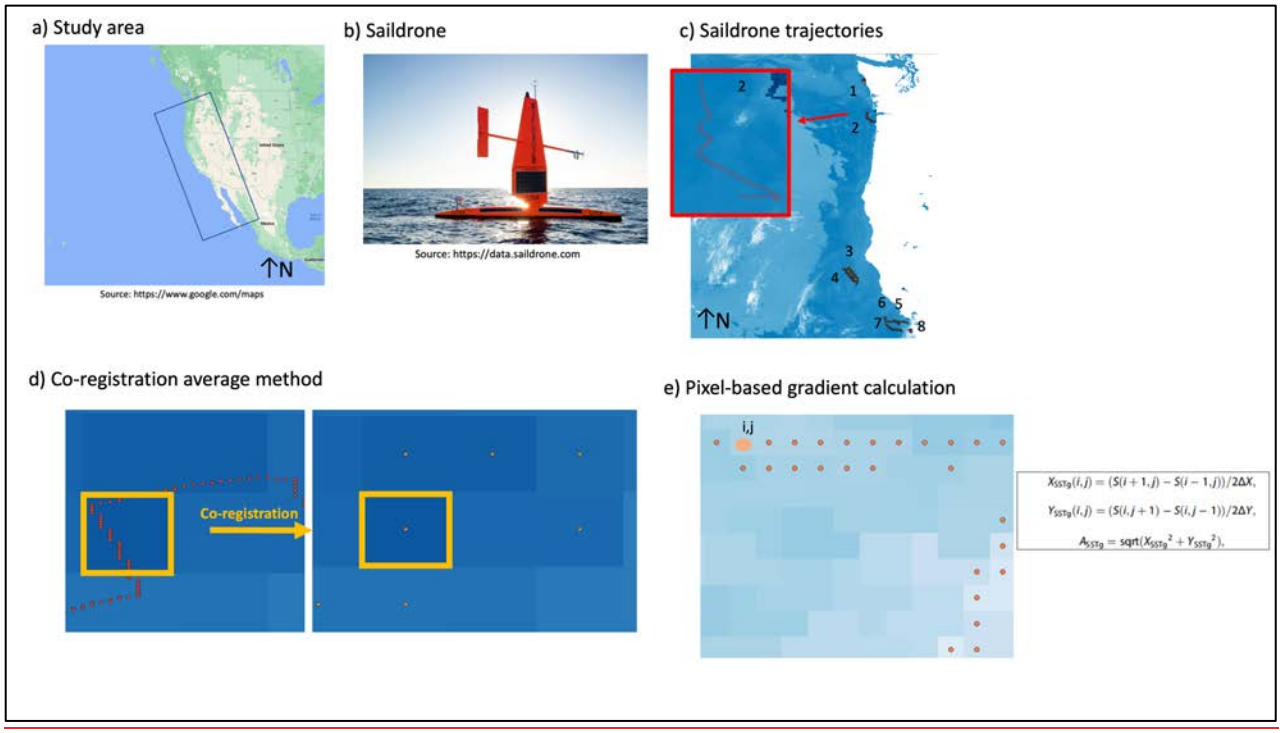

Figure 20: Study area (a); Saildrone vehicle (b); The eight West Coast 2019 Saildrone trajectories along the study area(c); Co-registration average method for the pixel-based SST calculation(d); Formula for pixel-based gradient calculation along each of the pixels within the Saildrone trajectory (e)

4.3. Methods

4.3.1 Sea Surface Temperature

To validate the satellite products using the Saildrone data, we performed a pixel-based comparison of the SST values of the three datasets, as well as a validation of the MODIS level-2 quality levels for each MODIS pixel.

To perform these two tasks, the three datasets had to be georeferenced to each other to eliminate spatial discrepancies between the datasets. As the MODIS level-2 product is not georeferenced (coordinates are on the native satellite swath grid), we registered it to the MUR level-4 product within the SeaDAS software provided by NASA (https://seadas.gsfc.nasa.gov/). Due to the high temporal sampling resolution of the Saildrone (1 minute), many Saildrone points fell within the same MODIS and MUR pixel.

Therefore, a further step was to co-register the Saildrone points with the satellite products. The co-registration was performed using the average of all Saildrone SST point values falling into each MODIS and MUR pixel (Vazquez-Cuervo et al., 2017) (see Figure 20d). After the co-registration of the three datasets, we performed the pixel-based comparisons of the SST values, and their discrepancies were quantified in terms of root mean squared error (RMSE) and mean absolute error (MAE).

4.3.2 Thermal gradients

Two different workflows were used to calculate and compare the gradients between the three datasets, which are described in the following two sections.

4.3.2.1 Pixel-based approach

The first approach is based on a pixel-based comparison between the gradients calculated on the Saildrone pixels (pixels along each Saildrone trajectory) and the gradients calculated on the corresponding pixels in the satellite products (see Figure 20e).

To perform this comparison, we calculated the magnitude of the SST spatial gradient at each pixel location i,j for all three datasets using a finite central differences [29]. The formula is as follows:

$$\begin{aligned} X_{SSTg}(i,j) &= (S(i+1,j)-S(i-1,j))/2\Delta X \\ Y_{SSTg}(i,j) &= (S(i,j+1)-S(i,j-1))/2\Delta Y \\ A_{SSTg} &= \sqrt{XSSTg(i,j)^2 + YSSTg(i,j)^2} \end{aligned} \qquad (1)$$

The terms X_{SSTg} and $Y_{SSTg}(i,j)$ denote the corresponding gradient (in K/km) in the longitudinal and latitudinal directions, respectively, and $S(i,j)$ denotes the SST pixel value of each product after its

co-registration (MODIS, MUR, Saildrone) at location i (longitude), j(latitude) along the Saildrone trajectory. The terms ΔX and ΔY are the distances in km the longitudinal and latitudinal directions between neighboring pixels. A_{SSTg} is the magnitude of the SST gradient at the given pixel at the given i, j location.

The discrepancies between the pixel-based calculated gradients for each of the satellite products and the Saildrone were quantified in terms of RMSE and MAE.

4.3.2.2. Kriging-based approach

The second approach was based on a kriging interpolation workflow for predicting Saildrone SST in unsampled locations [30]. This interpolation workflow is used to predict the SST in a larger spatial area around the sampled pixels where in-situ data were not available. This allows us to generate in situ data in unsampled areas and thus validate the satellite products in larger spatial areas. For the interpolation, we chose the ordinary kriging method. Kriging interpolation allows the spatial correlation between the sampled values to be taken into account and is therefore particularly useful in the case of our application.

More precisely, spatial correlation simply refers to the fact that neraby pixels are expected to have more similar SST values than those further away. Therefore, the interpolation is based on the spatial arrangement of the empirical observations (in our case the SST sampled Saildrone values), rather than using an assumed model of spatial distribution.

More specifically, the SST Saildrone data were used to derive the experimental variogram. The full workflow for the kriging interpolation is shown in
Figure **21**. The experimental variogram is a discrete function calculated using a measure of the variability between pairs of points at different distances. In other words, it describes how the data are correlated with distance.

As the experimental variogram does not provide information for all possible directions and distances between points, we fitted a variogram model to approximate the experimental variogram. In a subsequent step, the kriging interpolation was performed to predict the SST values at the unsampled locations using the fitted variogram. The prediction was made in the spatial area/window around the pixels of each Saildrone trajectory, as described in the previous paragraph.

The standard deviation of the interpolated SST values was also estimated at each predicted pixel location. Based on the standard deviation, and considering that SST estimations closer to the locations of the sampled data are more accurate, a mask was created. The mask included pixels with a standard deviation less than a defined threshold (see Figure 20d, e). This threshold was chosen to retain only the pixels with the smallest standard deviation, i.e. pixels close to the sampled locations/pixels. Gradients were then calculated for the valid pixels within the mask using formula 1.

Using the same mask, gradients were calculated for the same pixels on each satellite product using formula 1. The differences between these and those calculated on the kriging-based predicted SST pixel values as described above were expressed in terms of RMSE.

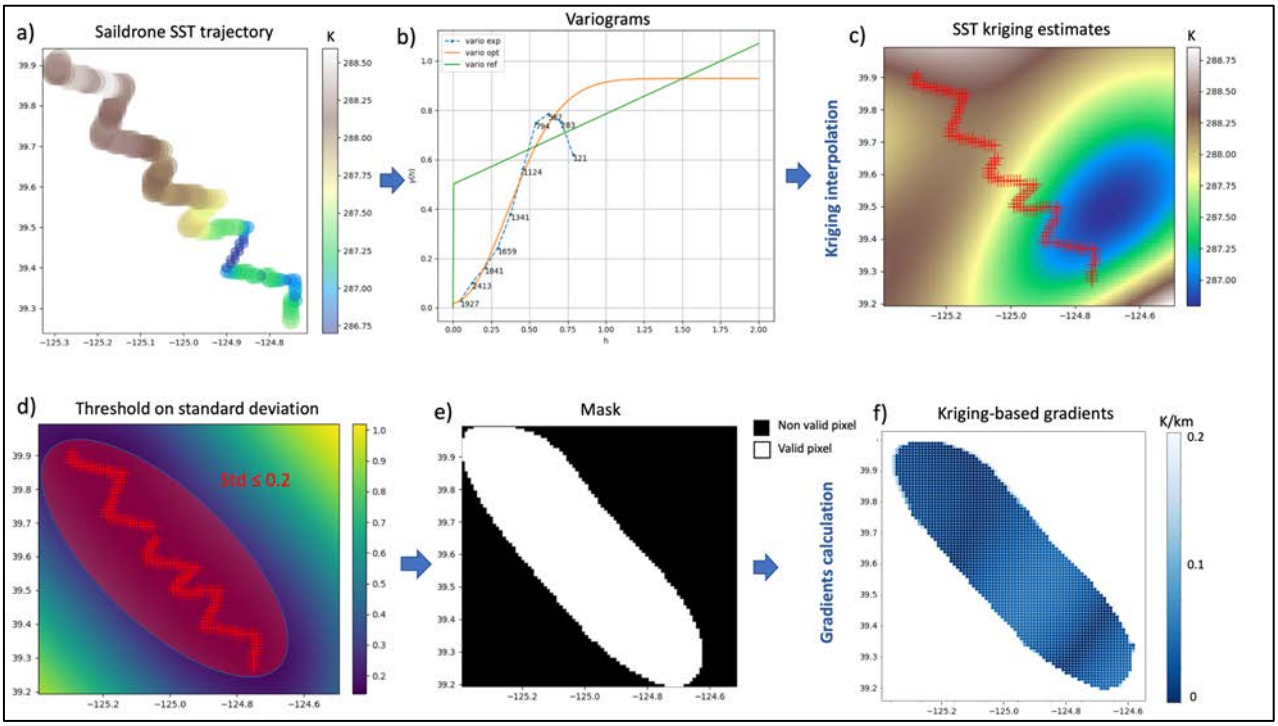

Figure 21: Workflow for the kriging interpolation using the Saildrone SST values for one of the trajectories

4.4 Results

4.4.1 Sea Surface Temperature

The comparisons between Saildrone and the two satellite products are summarized in the following two sections: In the first one, the accuracies in terms of RMSE and MAE are analyzed for all the Saildrone trajectories and are compared between the two products. The analysis is done with respect to the quality level of the corresponding MODIS product. The second section shows the SST maps for all the dates for both products, as well as the quality level of each pixel of the corresponding MODIS product. In addition, in this second section we show the evolution of the SST for both products along two characteristic trajectories, as well as the per-pixel value of each MODIS pixel along these two trajectories. The second section aims to understand the differences between the three datasets in space.

Each of the Saildrone trajectories was classified based on the number of bad-quality MODIS pixels it contained. As mentioned in the previous section, MODIS pixels of quality level one is defined as ‘‘bad-quality pixels’’. Pixels of quality levels three and four are defined as ‘‘medium-quality pixels’’ and pixels of quality level five are mentioned as ‘‘good-quality pixels’’. The percentage of bad-quality MODIS pixels for each trajectory is relative to all the pixels along each trajectory.

In the following, trajectories containing only bad-quality MODIS pixels (100%) are defined as ‘‘bad-quality trajectories’’. Trajectories containing more than 30% and less than 100% bad-quality MODIS

pixels are defined as ‘‘medium-quality trajectories’’, trajectories containing equal or less than 30% bad-quality MODIS pixels are defined as ‘‘good-quality trajectories’’. These classification thresholds are derived from the data in order to have a very well-defined separation between the three classes. The trajectories classified above are colored in red, orange, and green, respectively in the graphs and maps of the following sections.

4.4.1.1 Pixel-based Sea Surface Temperature comparisons

Figure 22a and Figure 22b show the RMSE and MAE between the Saildrone and the two satellite products for all 23 Saildrone trajectories. Figure 22c shows the percentage of bad-quality pixels for each of the trajectories. Bad, medium, and good-quality trajectories are shown in red, orange, and green colors respectively, according to the classification described at the beginning of Section 4.1. From all the quality trajectories, we extracted a mean RMSE of 0.86 and 4.64 K (Kelvin; hereafter K stands for Kelvin) for MUR and MODIS, respectively.

For all of the bad-quality trajectories, Figure 22a, b shows that the MODIS RMS1E and MAE are higher than the corresponding RMSE and MAE for the MUR. In particular, in some cases the MODIS RMSE and MAE reach very high values (number 3, 7), even almost 50 K. This result indicates the very poor-quality of the MODIS level-2 product, especially in areas close to the coast. However, since the other trajectories have much lower RMSE and MAE values than the 50 K value, we can consider this value as an outlier.

For the medium-quality trajectories, the RMSE and MAE values for the two products are more similar. Thus, as the quality of the MODIS product increases, its accuracy does not differ much from that of the corresponding level-4 interpolated MUR product. In particular, for one of the medium-quality trajectories (number 10), the accuracy of the MODIS product is better than that of the MUR.

However, for the medium-quality trajectories (number 5, 10, 23), the MUR products have higher inaccuracies than other bad-quality trajectories, even though they contain better-quality MODIS pixels. The same is true for the MODIS product for trajectory number 23. This specific result implies either the existence of errors during the interpolation process to extract the level-4 MUR product or the misclassification of MODIS pixels with respect to their quality level. In the latter case, bad-quality MODIS pixels may have been misclassified as medium-quality pixels and therefore the medium-quality trajectories contain fewer bad-quality pixels than they actuallydo.

For the good-quality trajectories, the RMSE and MAE values are generally lower for both products and more similar for both products, as can be seen in Figure 22a,b. Especially for the MODIS products, the accuracies are much better than the accuracies of the bad-quality trajectories

Therefore, as the quality of the MODIS products increases, MUR and MODIS have more similar RMSE and MAE values. There are cases of two trajectories (number 12, 13) where the MODIS is more accurate than the MUR. However, as in the case of the medium-quality trajectories, some good-quality trajectories appear to have higher RMSE and MAE values for the MUR products than other medium and bad-quality trajectories (such as numbers 12, 13). Also, for the MODIS products,

some good-quality trajectories (such as numbers 6, 8, 13) are less accurate than the medium-quality trajectory number 10. These last results confirm the similar finding derived for the medium-quality trajectories described in the previous paragraph regarding the potential errors within the processes of MODIS quality level characterization and MUR level-4 interpolation (see more in the Discussion section).

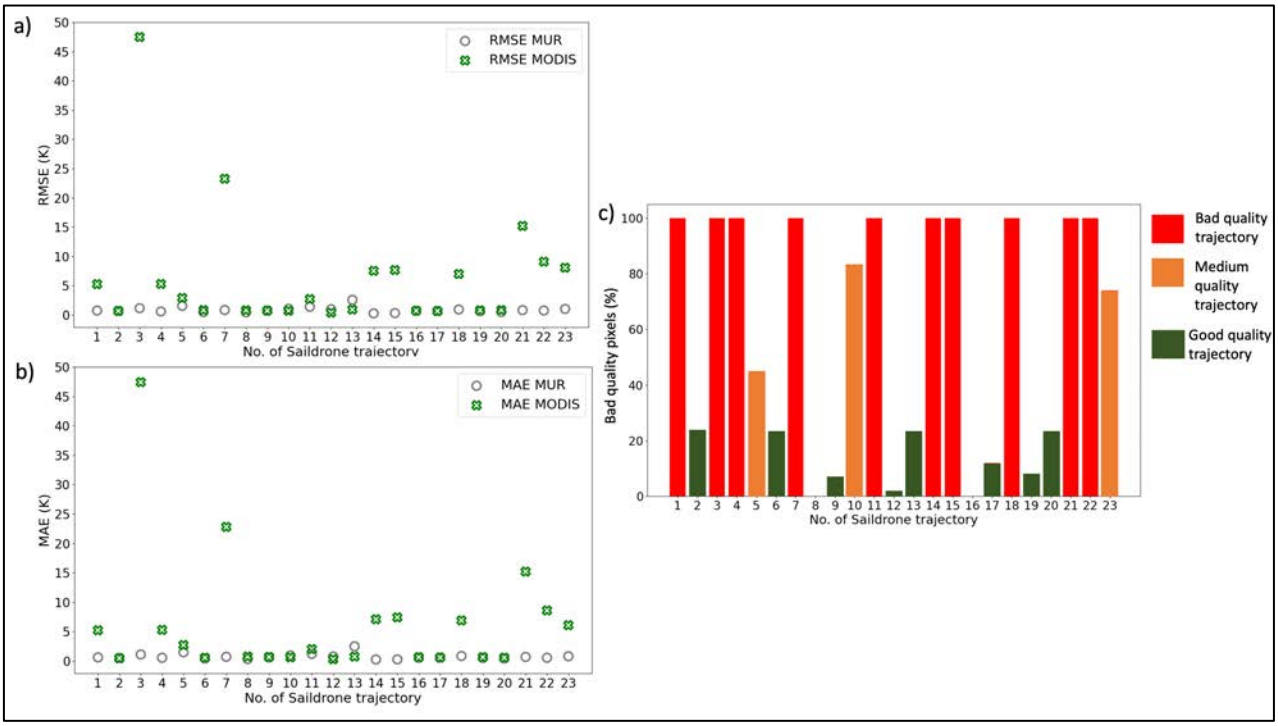

Figure 22: RMSE (a) and MAE (b) plot for both products and all the trajectories; percentage of bad-quality MODIS pixels for all the trajectories: in red, orange, and green the bad, medium, and good-quality trajectories, respectively (c).

4.4.1.2 Sea Surface Temperature maps

In Figure 23 there are the MODIS and MUR SST maps and the Saildrone SST trajectories for all the trajectories. It also includes the quality level map for the same area, where good-quality MODIS pixels are in red, medium-quality MODIS pixels are in orange, and good-quality MODIS pixels are in green. The numbering of the trajectories follows the numbering of the trajectories in the plots of the previous section.

Comparing the MODIS and MUR maps and using the quality level maps for all the dates, we see that the differences between the SST values within the products are greater in areas of bad-quality pixels (red areas). These areas are mainly near the coast (land is shown in black). Interestingly, the MODIS SST values appear to be underestimated in these red areas, as they are smaller than the corresponding MUR values (white areas within the MODIS maps). Therefore, the MODIS products seem to be less accurate in the red areas. The differences between the two products become smaller (more similar pixel colors) in the medium and good pixel areas, shown in orange and green colors respectively. Especially in the green areas, the two products seem to have the smallest

differences in SST, even though they are spatially limited. Consequently, the visual interpretation of the maps in Figure 23 confirms the results analyzed above on the basis of Figure 22.

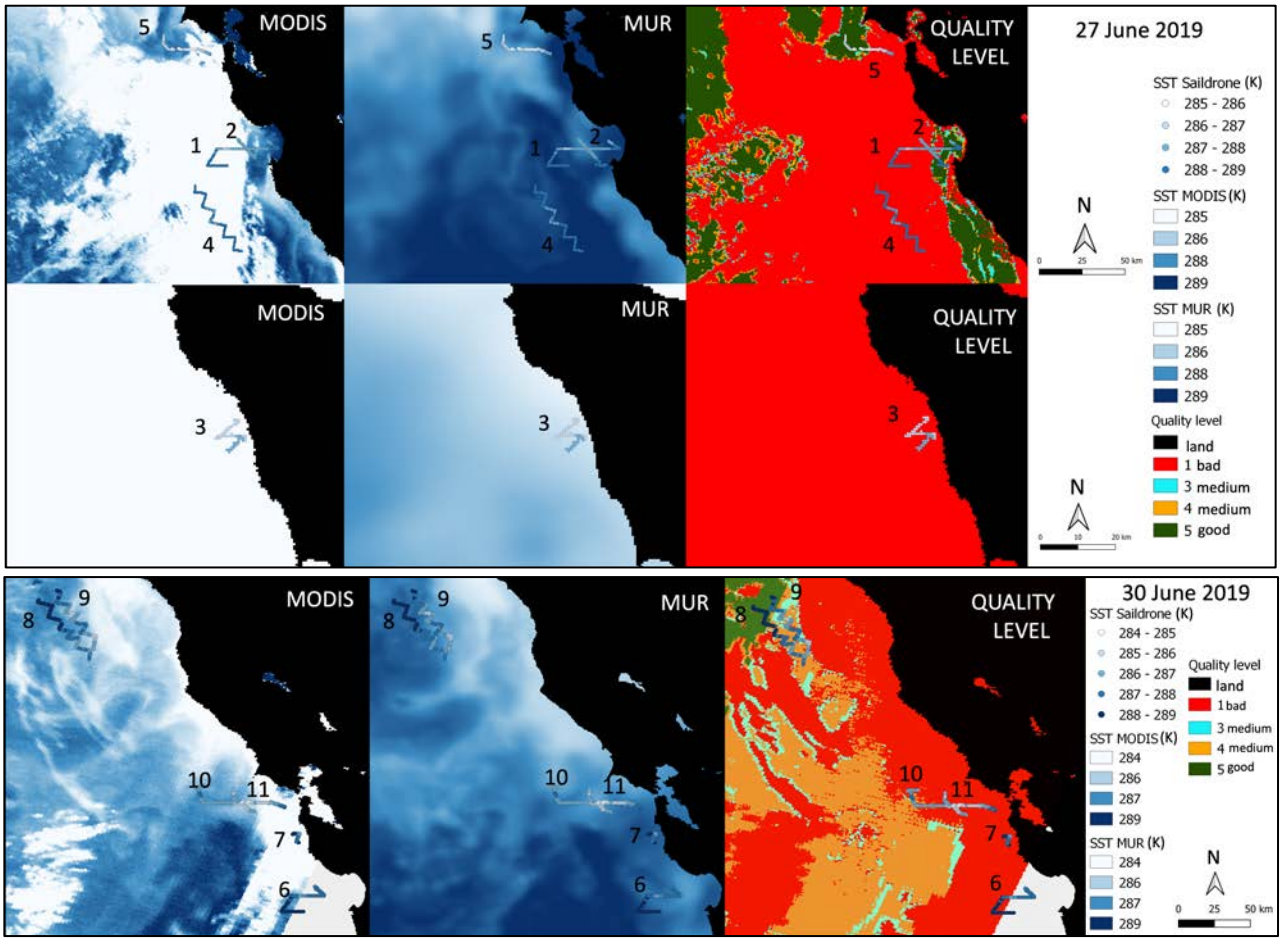

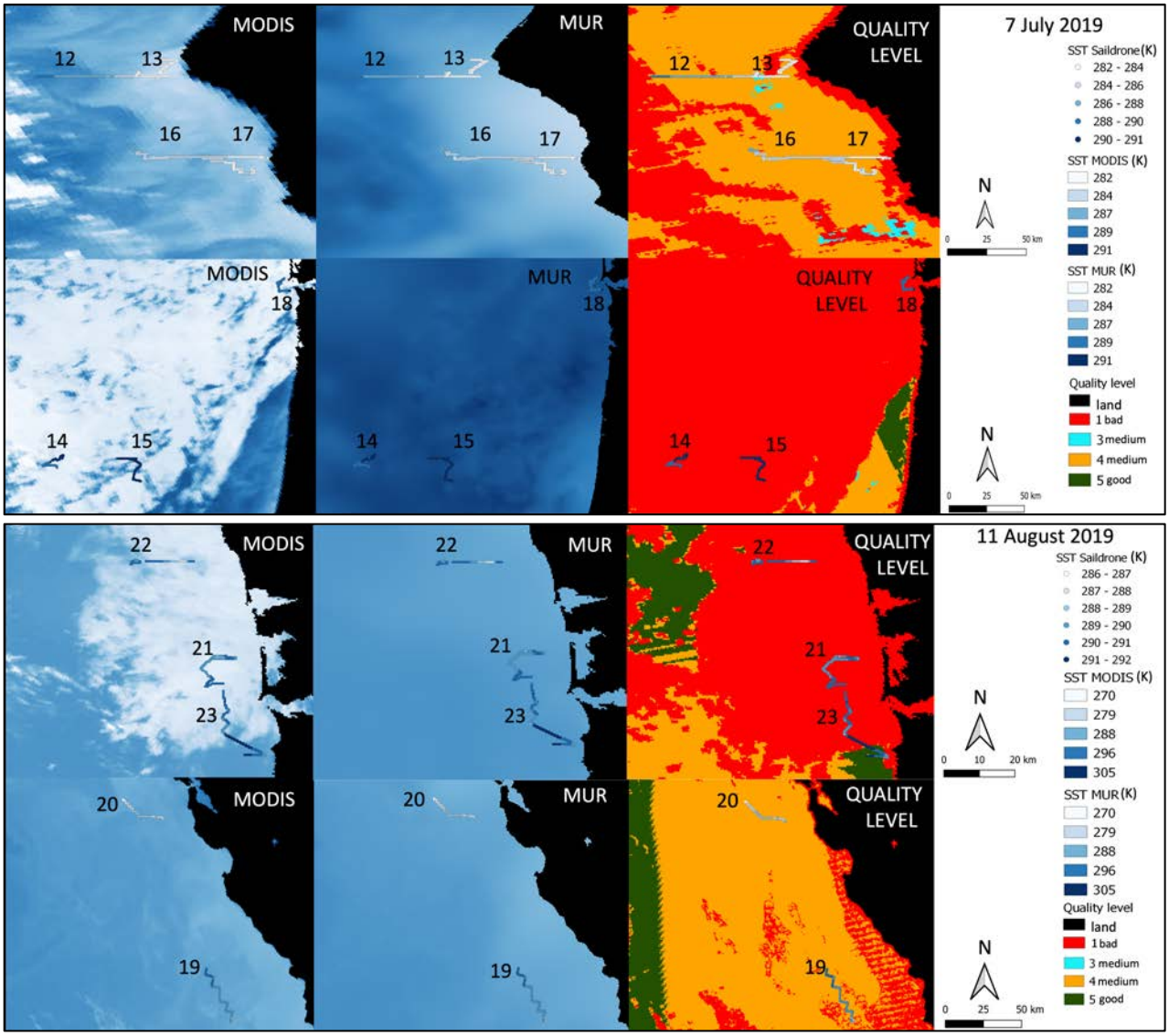

Figure 23: SST and quality level maps for all the dates and the three datasets. The SST maps depict the SST values for the two satellite products and the Saildrone trajectories in degrees Kelvin. The quality level maps correspond to the quality level (from 1 to 5) for each MODIS pixel.

4.4.1.3 Sea Surface Temperature evolution within trajectories

The plots in Figure 24 show the evolution of the SST for the three datasets along two Saildrone trajectories during the 11th of August (plots 1a, 2a). The quality level of each MODIS pixel along each of the trajectories is also shown in plots 1b and 2b. The trajectories are shown on a map showing the MODIS quality levels of each pixel in the surrounding area. The first trajectory (plot 1) shows a medium-quality trajectory, as it contains 74% of bad-quality pixels. The second trajectory (plot 2) shows a good-quality trajectory, containing only 8% bad-quality pixels.

Firstly, the MUR SST values (green color in plots 1a,1b) are closer to the Saildrone reference SST values (in blue) than to the MODIS values (in orange) over most of the trajectory and for both trajectories. Secondly, the MODIS signal is noisier than the MUR throughout the entire trajectory for both whole trajectories.

Plots 1b and 2b show for both trajectories that the mismatch between MODIS and Saildrone increases for pixel locations that corresponding to bad-quality level MODIS pixels (quality level 1). These areas are marked with red boxes in plots 1b, and 2b.

For the medium-quality trajectory, the mismatch between Saildrone and MODIS increases at the end of the trajectory where only bad pixels exist, and reaches about 20 K. For the good-quality trajectory, the largest mismatch is found at the beginning of the trajectory (around 3 K), where the bad pixels are mainly located. For the medium-quality trajectory, the mismatch between Saildrone and both products becomes smaller at the locations of good-quality level pixels which are shown in green color in map 1c. These good-quality areas are located at the beginning of the trajectory. In the case of the good-quality trajectory, there are mismatches between both products and Saildrone along the entire trajectory. However, The mismatche decrease at the locations of the medium-quality level pixels, as shown in orange in map 2c.

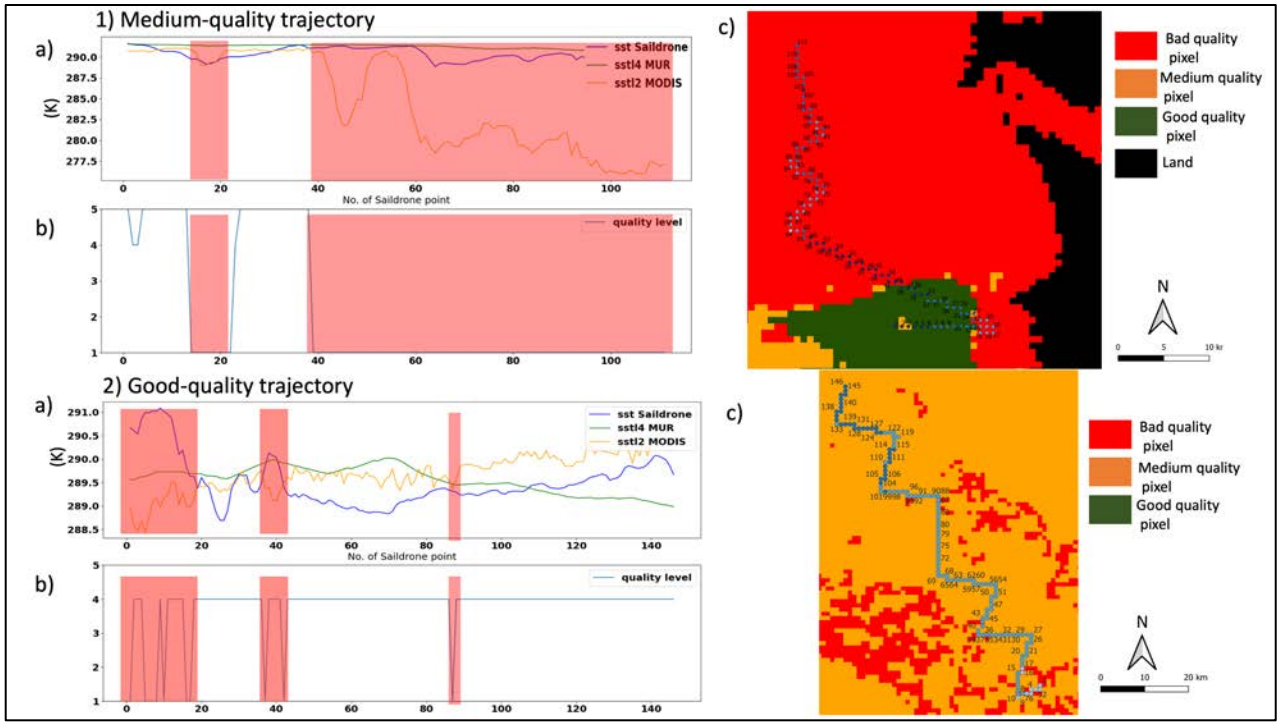

Figure 24: SST evolution of the Saildrone (blue), MUR (green), and MODIS (orange) SST along the two Saildrone trajectories during the 11th of August (1a, 2a); the quality level of each MODIS pixel along the trajectories (1b, 2b); the quality level maps (1c,2c) with the trajectories, in which the points of the trajectories are numbered following the numbering of the x-axis in the plots (1,2)a and (1,2)b.

4.4.2 Thermal gradients

4.4.2.1 Pixel-based approach

For the pixel-based approach, formula 1 was used to calculate the spatial SST gradient for each of the pixels along the Saildrone trajectory and the corresponding pixels within the two satellite products. Figure 25a summarizes the results in terms of the RMSE between Saildrone and the two satellite products, relative to the percentage of bad-quality MODIS pixels of each trajectory shown

in Figure 25c. From all the quality trajectories we extracted a mean RMSE of 0.19 and 0.84 K/km for MUR and MODIS, respectively.
For all the bad-quality trajectories, the MUR products are more accurate in terms of RMSE than the corresponding MODIS products, except for one trajectory (number 12). The RMSE values range from 0.16-4,6 K/km for MODIS and from 0.04-0.39 K/km for MUR. The differences in RMSE between the two products are large, reaching almost 4.2 K/km. The MODIS products appear to have high inaccuracies (RMSE up to 4.6 K/km) in some bad-quality trajectories (number 3, 7).

For the medium and good-quality trajectories, the RMSE values for both products are closer to each other than in the case of the bad-quality trajectories. MUR is more accurate than MODIS. However, the trajectories of medium-quality do not correspond to lower RMSE values than the bad-quality trajectories for both products. On the contrary, for some trajectories (number 5, 23) the inaccuracies are higher compared to some bad-quality trajectories, for both products and especially for MUR.

For the good-quality trajectories, the RMSE values for both products are also similar to those for the bad-quality trajectories. For MODIS, the accuracies for the good-quality trajectories are generally much better than those for the bad-quality trajectories. The only exception is trajectory number 2, where the RMSE is larger than the RMSE of one of the medium-quality trajectories (number 5) and one of the bad-quality trajectories (number 11).

Comparing the two products, MUR is generally more robust or equally robust compared to MODIS, with the exception of trajectory number 12. The higher RMSE for the MUR compared to the MODIS product for the good trajectory number 12, and the increased RMSE values for some medium and good-quality trajectories for both products, are similar results to those derived from the SST pixel-based comparisons in Section 4.1.1. They may indicate the following: Either possible errors in the characterization/classification of the quality levels of some MODIS pixels, or errors in the interpolation to produce the level-4 MUR product.

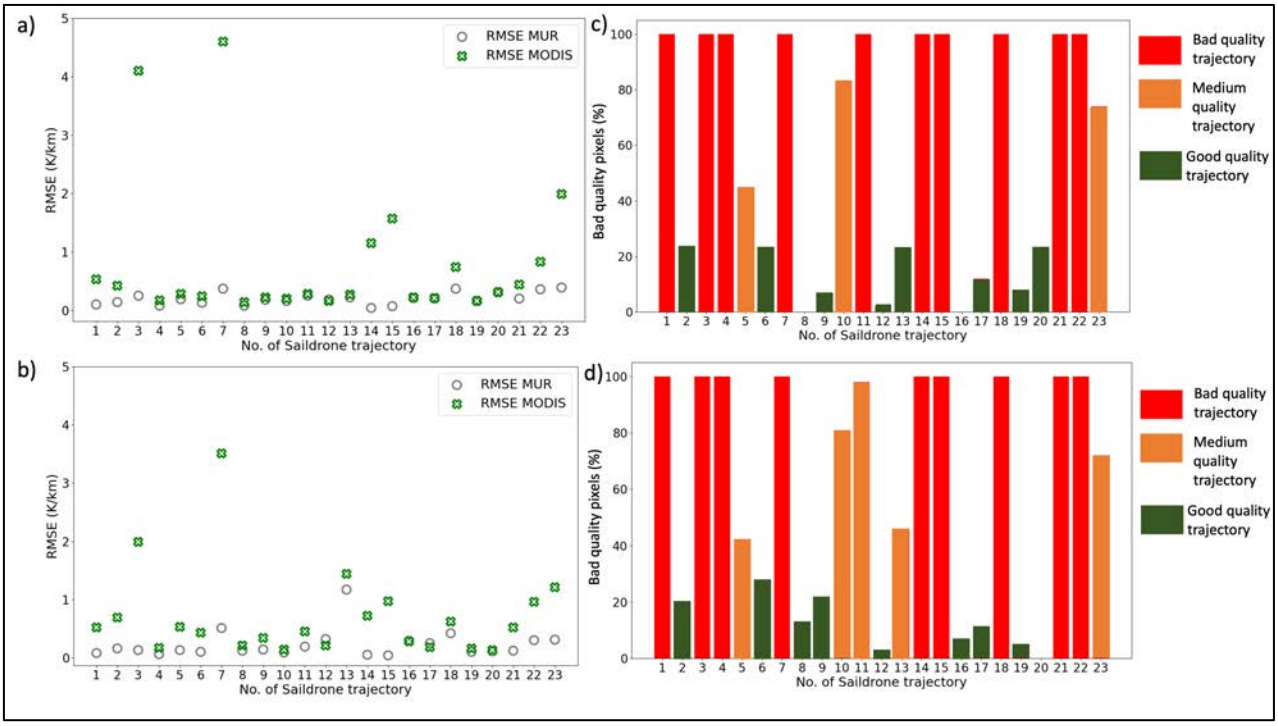

Figure 25: RMSE plots for the pixel-based (a) and kriging-based (b) gradients comparisons; percentage of bad-quality MODIS pixels for each of the trajectory for the pixel-based (c) and kriging-based (d)approach: in red, orange and green the bad, medium and good-quality trajectories, respectively.

4.4.2.2 Kriging-based approach

For the kriging-based approach, formula 1 was used to calculate the spatial SST gradients for all the kriging-based SST values within the mask, as described in section 3.2.2. Formula 1 was also used to calculate the gradients for all the pixels of the two satellite products within the same mask. The comparisons in terms of RMSE between the kriging-based gradients and those calculated directly from the satellite products are shown in Figure 25b. The percentage of bad-quality MODIS pixels of each trajectory is also shown in Figure 25d. From all the quality trajectories we extracted a mean RMSE of 0.23 and 0.71 K/km for MUR and MODIS, respectively.

The results in terms of RMSE are slightly better for the kriging-based approach than for the pixel-based approach for MODIS products, and very similar for MUR products (slightly better for the pixel-based approach). The RMSE values range from 0.13-3.51 K/km for MODIS and from 0.04-1.17 K/km for MUR. The maximum difference between the two products is 3 K/km.

For all the bad-quality trajectories the MUR RMSE is lower than that of the MODIS. The highest inaccuracies of MODIS are found mainly found for the bad trajectories, with a maximum RMSE of 3.51 K/km (number 7). The differences between the two products decrease for medium and good-quality trajectories. For the medium-quality trajectories, MUR is generally more accurate than MODIS. For the good-quality trajectories, MUR is generally more accurate than the corresponding MODIS, except for the trajectories with numbers 12, 16, 17. Also, as found in the results for the gradient pixel-based approach, some medium and good trajectories (numbers 2, 11, 23) have higher MUR errors than some bad trajectories.

These latter results, also found in the pixel-based SST comparisons and the pixel-based gradient comparisons, suggest possible biases in the processes of characterizing the quality levels and the MUR interpolation.

4.5. Discussion

4.5.1 Accuracies compared to previous Saildrone studies

We derived mean SST RMSE of 0.86 and 4.64 K for MUR and MODIS respectively (excluding the outlier of 50K).

Our study showed higher bias and RMSE between SST MUR and Saildrone for most of the trajectories compared to the study of Vazquez-Cuervo et al., 2019 during the 2018 campaign along Baja California (bias of 0.32 deg Celsius and RMSE of 0.42 deg Celsius). However, compared to the previous study comparing MUR SST with two Saildrone deployments over the Arctic and Alaskan coastal waters, which derived RMSE of about 7 and 9 deg Celsius (Vazquez-Cuervo et al., 2022), our results are more promising in terms of the accuracy of the MUR products (we found a maximum RMSE of 2.57 K).

The high gradient values we obtained in most trajectories are due to the coastal upwelling that occurs within the distance of 100 km from the California Coast.

Similar results for the California Coast are derived from the recent study by Vazquez-Cuervo et al., 2023 who found gradients for MUR products as high as 1 K/km. They also found very similar results for the MUR RMSE (0.21 K/km) compared to ours (mean RMSE MUR of 0.19 K/km for the pixel-based gradient approach and 0.23 K/km for the kriging-based approach). Therefore, our RMSE values for the MUR gradients are reasonable considering the ocean dynamics of the California Coast due to the California Current System.

Comparing the gradients between MUR and Saildrone over Peru and Chile, Vazquez-Cuervo et al., 2017 identified the maximum magnitude of the gradients up to 0.03 K/km (Vazquez-Cuervo et al., 2017). In our study, the maximum magnitude of the MUR gradient was higher, reaching even 0.8 K/km.

Since no previous studies have validated MODIS level-2 over the California Coast, we were not able to compare our results with previous studies specifically for our study area. The mean SST MODIS RMSE of 4.64 K and the mean gradient RMSE of 0.71-0.81 K/km are rather high compared to the MUR RMSE of our study and the previous studies over the California Coast. These high inaccuracies indicate the poor quality of MODIS level-2 data in coastal areas especially over summer months when there is increased cloud coverage. In the next section, we compare our results for MODIS with previous MODIS studies in other areas of the world.

4.5.2 Accuracies compared to previous MODIS studies

Comparing our MODIS results in terms of RMSE SST with previous studies conducted in other study areas, we conclude that our MODIS RMSE values are rather high.

More specifically, Qin et al., 2014 found a bias of 0.19-0.34 deg Celsius within the MODIS data in the South China Sea when compared with in situ data 5m below the surface. Comparison with coastal buoys extracted RMSE between 0.36 and 1.42 deg Celsius over the Bay of Bengal, India (Pasula and Sil, 2019), lower than in our study. Ghanea et al., 2016 compared MODIS level-2 with SST_{depth} buoys-based measurements over the Persian Gulf and found a bias of 0.07 deg Celsius at 63 measurement points and a RMSE of 0.53 deg Celsius.

The high RMSE and MAE values of the MODIS products that were found close to the coast, confirm the poor quality of the infrared data in cloud-covered areas, as also found also in the study by Moteki, 2022. In fact, close to the coast there are only bad-quality pixels due to high cloud cover during the summer months. We have also seen in Section 4.1.2 that the MODIS signal is very noisy, even noisier than the corresponding MUR signal. One reason that could explain the high noise within the MODIS level-2 product, is the fact that since it is a level-2 product it is still at an early stage of processing where not all noise sources have been eliminated. Other reasons that may explain the much noisier MODIS signal, such as errors related to sensor characteristics, are the subject for future investigations and are beyond the scope of this study.

Regarding the MUR products, beyond the comparisons we made between them and the Saildrone and MODIS data, we could not perform further analysis to assess the per-pixel quality of the interpolation as we did for the MODIS quality levels. This is because we did not have information available on exactly which data (AVHRR, microwave, in situ) were used to interpolate each pixel when MODIS level-5 data were not available.

4.5.3 Source of errors due to Saildrone

Existing literature has already demonstrated the efficiency of averaging Saildrone values for co-registration with satellite products (Vazquez-Cuervo et al., 2019, 2017). The Euclidean distance co-registration method was also tested on our dataset and gave similar results to the averaging co-registration method. The Saildrone is a wind-powered vehicle and therefore shifts in its trajectory are expected. Although no SST differences of more than half a degree Kelvin were found within pixels for the Saildrone trajectories, averaging for co-registration purposes could also introduce uncertainties. In addition, the Saildrone can detect SST changes at higher spatiotemporal resolutions (sub-kilometer and sub-daily) than the corresponding satellite products, which also explains the discrepancies (Vazquez-Cuervo et al., 2019).

4.5.4 Source of errors due to mismatches between the instruments

There are differences in what the three instruments explicitly measure, both in space and in time. MODIS L2P maps SST_{skin} whereas MUR is tuned to a bulk temperature by using only nighttime retrievals. Thus, the issue of diurnal variability could still be a factor in the measured differences between the three data sets. More detailed information is provided below. The Saildrone sensor used in this current study measures bulk SST (SST_{depth}) at 0.6 m below the surface. The Saildrone sensor that measures SST_{skin} is also under development, according to a recent study (Jia et al., 2022), and this will also improve the ability of Saildrones to validate satellite SST products.
In addition, MUR uses a 5-day window for the interpolation, unlike MODIS and Saildrone data which refer to a specific acquisition time and day, respectively. As a consequence, the three datasets also have a temporal mismatch with respect to the SST values they measure: MUR includes only nighttime measurements, and MODIS level-2P SST corresponds to a specific time, which we tried to be as close as possible to a nighttime measurement to coincide with the MUR SST. However, it was not always possible to find good MODIS data due to the high cloud contamination problems during this period of the year. The Saildrone data corresponded to a whole 24h time window, including both day and night measurements, with the assumption that SST variations measured by the radiometer within a day are negligible.

4.5.5 Assessment of the MODIS quality levels and the MUR interpolation

Regarding the assessment of the characterization of the quality levels of the MODIS products, the characterization of the bad-quality pixels is generally accurate. As can be seen from the analysis of the SST and the gradients, pixels characterized as bad-quality pixels during the production of the level-2 MODIS product are indeed bad pixels/values and are correctly excluded from the production of the gridded SST maps. These areas consisting mainly of bad pixels are those close to the coast, and therefore we can conclude that the characterization of the MODIS quality level seems to be valid in areas close to the coast that are covered by clouds. This result confirms the low quality of MODIS level-2 data that we can obtain in coastal areas due to factors such as cloud cover and erroneous atmospheric correction (Mouw et al., 2015).

The results for the medium and good-quality trajectories imply that some pixels have been misclassified as medium or good-quality pixels when they appear to correspond to bad-quality pixels. Conversely, some pixels have been classified as bad-quality when they appear to correspond to medium or good-quality pixels. As a result, they are erroneously included or excluded in the production of the gridded SST maps, respectively, during the processing of the MODIS level-2 products. Furthermore, the misclassification of some pixels as ‘‘bad-quality pixels’’ results in data loss and interpolation for the creation of the SST maps in pixel areas that are not needed. Therefore, the interpolation to produce the level-4 MUR product contains errors and this can explain the increased RMSE and MAE values for the MUR in some good and medium-quality trajectories. This inaccurate interpolation in some pixels indicates that the level-2 MODIS product may be more accurate than the corresponding level-4 MUR, even though the former is a level-2

dataset in a primary data processing step with some sources of error not yet removed. In addition, the process of assigning quality levels to each pixel is an area of ongoing research.

An interesting potential study which was not investigated in this study is the assessment of the quality levels relevant to the distance from the coast.

4.5.6 Comparing both gradient approaches

The use of a larger pixel window around the Saildrone trajectory within the kriging-based approach was made to avoid using only the pixels within the Saildrone trajectory and to have a better representation of the area around the trajectory. Using only the pixels within the trajectory and considering that the Saildrone trajectories may contain shifts due to wind (see section 5.3), inaccuracies in the x and y coordinates can lead to incorrect estimates of gradients using formula 1. In fact, the results of the kriging-based approach are more promising, as they generally show lower RMSE values for the MODIS products than the results of the pixel-based approach.

In addition, the kriging interpolation method is useful because the Saildrones are mainly used near the coast and therefore there is a lack of data outside the coast. By interpolating the SST sampled Saildrone values in areas away from the coast, we ‘‘generate’’ in situ data in areas where we do not yet have Saildrones deployments. This allows us to produce a new dataset for the validation of satellite products, with the high spatial and temporal resolution of Saildrones. Our work can also show future researchers where are the areas that need to be validated in more detail and therefore where in situ instruments need to be deployed. Such areas appear to be those far away from the coast. For the areas close to the coast, we have shown that the quality of level-2 MODIS is very low (very high or complete coverage of bad pixels) and that the characterization of the quality levels of MODIS is already generally accurate.

More advanced interpolation approaches, such as taking into account correlations between Saildrone and satellite products, could be further explored in future work.

The methods used in this study can also be applied to other study areas as well. Our study provides a basis for investigating the magnitude of phenomena such as coastal upwelling, especially with the integration of additional parameters such as chlorophyll-a provided by from satellites and Saildrones. Also, our study was focused on the summer months, so it could be interesting to replicate our work during the winter months, when the cloud cover is potentially lower and we therefore expect level-2 MODIS SST data of better quality.

4.6 Conclusions

From the comparisons between Saildrone and satellite products using the pixel-based SST approach, from all the trajectories we derived a mean RMSE of 0.86 and 4.64 K for MUR and MODIS (excluding the outlier), respectively. From the gradient approaches, we derived a mean RMSE of 0.19 and 0.84 K/km for MUR and MODIS for the pixel-based approach, and a mean RMSE of 0.23

and 0.71 K/km for MUR and MODIS for the kriging-based approach. These results for MUR are promising for considering the results of previous studies and the influence of the dynamics of the coastal upwelling over the California Coast. The results for MODIS show rather high inaccuracies compared to the corresponding MUR products and other studies over different study areas. The high inaccuracies for MODIS deriving from our study highlight the poor-quality of MODIS level-2 data near the coast, especially during the summer.
Our comparisons with Saildrone data also showed that for the bad-quality trajectories, the MUR interpolated product was more accurate than the MODIS. For the medium and good-quality trajectories, MUR was generally more accurate than MODIS, with some exceptions. These exceptions reveal possible inaccuracies within the processes of characterizing the quality level of MODIS pixels and the interpolation process for producing the MUR level-4 gridded product.

The pixel-based gradient approach gave similar results to the kriging-based approach, with the kriging-based approach being more accurate in terms of RMSE for MODIS. Kriging interpolation is an approach to generate SST data in areas where Saildrone deployments are still lacking, and to indicate where future campaigns should be conducted. The latter is important as more data acquisitions away from the coast are needed to better validate the satellite products.

The characterization of MODIS quality levels appears to be generally valid for the bad-quality pixels, especially in coastal areas, but less valid for the medium and bad-quality pixels. Further research on the assessment of the MODIS quality levels is needed, for example in relation to distance from the coast.

Considering all the above-mentioned results, the Saildrone technology proved to be efficient in validating ocean satellite products due to its high spatial and temporal sampling capabilities compared to traditional in situ measurement techniques. This current study shows that high spatiotemporal in situ data can be successfully used to validate ocean SST products, both for pixel-level SST values and SST gradients. There are promising areas for further research, such as the use of Saildrone data to detect sub-pixel variations and to downscale satellite products using machine learning techniques.

Acknowledgments

The project was supported through a Fonds de donations grant from the University of Neuchatel. Kalliopi Koutantou and Philip Brunner were supported by the University of Neuchatel and Jorge Vazquez-Cuervo from NASA Jet Propulsion Laboratory, California Institute of Technology. The research was carried out at the Jet Propulsion Laboratory, California Institute of Technology, under a contract with the National Aeronautics and Space Administration (80NM0018D0004). The authors would like to thank Philippe Renard and Julien Straubhaar for their assistance in the geostatistical simulations.

References

lerskans, E., Høyer, J.L., Gentemann, C.L., Pedersen, L.T., Nielsen-Englyst, P., Donlon, C., 2020. Construction of a climate data record of sea surface temperature from passive microwave measurements. Remote Sens. Environ. 236, 111485. https://doi.org/10.1016/j.rse.2019.111485

Ashfaq, M., Skinner, C.B., Diffenbaugh, N.S., 2011. Influence of SST biases on future climate change projections. Clim. Dyn. 36, 1303–1319. https://doi.org/10.1007/s00382-010-0875-2

Atkinson, C.P., Rayner, N.A., Roberts-Jones, J., Smith, R.O., 2013. Assessing the quality of sea surface temperature observations from drifting buoys and ships on a platform-by-platform basis. J. Geophys. Res. Oceans 118, 3507–3529. https://doi.org/10.1002/jgrc.20257

Cao, M., Mao, K., Yan, Y., Shi, J., Wang, H., Xu, T., Fang, S., Yuan, Z., 2021. A New Global Gridded Sea Surface Temperature Data ProductBased on Multisource Data (preprint). Oceanography – Physical. https://doi.org/10.5194/essd-2021-6

Castro, S.L., Wick, G.A., Steele, M., 2016. Validation of satellite sea surface temperature analyses in the Beaufort Sea using UpTempO buoys. Remote Sens. Environ. 187, 458–475. https://doi.org/10.1016/j.rse.2016.10.035

Chin, T.M., Milliff, R.F., Large, W.G., 1998. Basin-Scale, High-Wavenumber Sea Surface Wind Fields from a Multiresolution Analysis of Scatterometer Data. J. Atmospheric Ocean. Technol. 15, 741–763. https://doi.org/10.1175/1520-0426(1998)015<0741:BSHWSS>2.0.CO;2

Chin, T.M., Vazquez-Cuervo, J., Armstrong, E.M., 2017. A multi-scale high-resolution analysis of global sea surface temperature. Remote Sens. Environ. 200, 154–169. https://doi.org/10.1016/j.rse.2017.07.029

Clemesha, R.E.S., Gershunov, A., Iacobellis, S.F., Williams, A.P., Cayan, D.R., 2016. The northward march of summer low cloudiness along the California coast. Geophys. Res. Lett. 43, 1287–1295. https://doi.org/10.1002/2015GL067081

Cokelet, E.D., Meinig, C., Lawrence-Slavas, N., Stabeno, P.J., Mordy, C.W., Tabisola, H.M., Jenkins, R., Cross, J.N., 2015. The use of Saildrones to examine spring conditions in the Bering sea, in: OCEANS 2015 - MTS/IEEE Washington. Presented at the OCEANS 2015 - MTS/IEEE Washington, pp. 1–7. https://doi.org/10.23919/OCEANS.2015.7404357

Emery, W.J., Baldwin, D.J., Schlüssel, P., Reynolds, R.W., 2001. Accuracy of in situ sea surface temperatures used to calibrate infrared satellite measurements. J. Geophys. Res. 106, 2387–2405. https://doi.org/10.1029/2000JC000246

Gentemann, C.L., Meissner, T., Wentz, F.J., 2010. Accuracy of Satellite Sea Surface Temperatures at 7 and 11 GHz. IEEE Trans. Geosci. Remote Sens. 48, 1009–1018. https://doi.org/10.1109/TGRS.2009.2030322

Ghanea, M., Moradi, M., Kabiri, K., Mehdinia, A., 2016. Investigation and validation of MODIS SST in the northern Persian Gulf. Adv. Space Res. 57, 127–136. https://doi.org/10.1016/j.asr.2015.10.040

Gruber, N., Lachkar, Z., Frenzel, H., Marchesiello, P., Münnich, M., McWilliams, J.C., Nagai, T., Plattner, G.-K., 2011. Eddy-induced reduction of biological production in eastern boundary upwelling systems. Nat. Geosci. 4, 787–792. https://doi.org/10.1038/ngeo1273

Guan, L., Kawamura, H., 2003. SST Availabilities of Satellite Infrared and Microwave Measurements. J. Oceanogr. 59, 201–209. https://doi.org/10.1023/A:1025543305658

Hansen, D.V., Poulain, P.-M., 1996. Quality Control and Interpolations of WOCE-TOGA Drifter Data. J. Atmospheric Ocean. Technol. 13, 900–909. https://doi.org/10.1175/1520-0426(1996)013<0900:QCAIOW>2.0.CO;2

Huyer, A., 1983. Coastal upwelling in the California current system. Prog. Oceanogr. 12, 259–284. https://doi.org/10.1016/0079-6611(83)90010-1

Iacobellis, S.F., Cayan, D.R., 2013. The variability of California summertime marine stratus: Impacts on surface air temperatures. J. Geophys. Res. Atmospheres 118, 9105–9122. https://doi.org/10.1002/jgrd.50652

Jia, C., Minnett, P., Luo, B., 2022. Significant Diurnal Warming Events Observed by Saildrone at High Latitudes (preprint). Oceanography. https://doi.org/10.1002/essoar.10512612.1

Lantuéjoul Cristian, 2002. Geostatistical Simulation.

Liu, Y., Chin, T.M., Minnett, P.J., 2017. Sampling errors in satellite-derived infrared sea-surface temperatures. Part II: Sensitivity and parameterization. Remote Sens. Environ. 198, 297–309. https://doi.org/10.1016/j.rse.2017.06.011

Meinig, C., Burger, E.F., Cohen, N., Cokelet, E.D., Cronin, M.F., Cross, J.N., de Halleux, S., Jenkins, R., Jessup, A.T., Mordy, C.W., Lawrence-Slavas, N., Sutton, A.J., Zhang, D., Zhang, C., 2019. Public–Private Partnerships to Advance Regional Ocean-Observing Capabilities: A Saildrone and NOAA-PMEL Case Study and Future Considerations to Expand to Global Scale Observing. Front. Mar. Sci. 6.

Merchant, C.J., Embury, O., Bulgin, C.E., Block, T., Corlett, G.K., Fiedler, E., Good, S.A., Mittaz, J., Rayner, N.A., Berry, D., Eastwood, S., Taylor, M., Tsushima, Y., Waterfall, A., Wilson, R., Donlon, C., 2019. Satellite-based time-series of sea-surface temperature since 1981 for climate applications. Sci. Data 6, 223. https://doi.org/10.1038/s41597-019-0236-x

Minnett, P.J., Alvera-Azcárate, A., Chin, T.M., Corlett, G.K., Gentemann, C.L., Karagali, I., Li, X., Marsouin, A., Marullo, S., Maturi, E., Santoleri, R., Saux Picart, S., Steele, M., Vazquez-Cuervo, J., 2019. Half a century of satellite remote sensing of sea-surface temperature. Remote Sens. Environ. 233, 111366. https://doi.org/10.1016/j.rse.2019.111366

Mordy, C., Cokelet, E., De Robertis, A., Jenkins, R., Kuhn, C., Lawrence-Slavas, N., Berchok, C., Crance, J., Sterling, J., Cross, J., Stabeno, P., Meinig, C., Tabisola, H., Burgess, W., Wangen, I., 2017. Advances in Ecosystem Research: Saildrone Surveys of Oceanography, Fish, and Marine Mammals in the Bering Sea. Oceanography 30. https://doi.org/10.5670/oceanog.2017.230

Moteki, Q., 2022. Validation of satellite-based sea surface temperature products against in situ observations off the western coast of Sumatra. Sci. Rep. 12, 92. https://doi.org/10.1038/s41598-021-04156-0

Mouw, C.B., Greb, S., Aurin, D., DiGiacomo, P.M., Lee, Z., Twardowski, M., Binding, C., Hu, C., Ma, R., Moore, T., Moses, W., Craig, S.E., 2015. Aquatic color radiometry remote sensing of coastal and inland waters: Challenges and recommendations for future satellite missions. Remote Sens. Environ. 160, 15–30. https://doi.org/10.1016/j.rse.2015.02.001

O'Carroll, A.G., Armstrong, E.M., Beggs, H.M., Bouali, M., Casey, K.S., Corlett, G.K., Dash, P., Donlon, C.J., Gentemann, C.L., Høyer, J.L., Ignatov, A., Kabobah, K., Kachi, M., Kurihara, Y., Karagali, I., Maturi, E., Merchant, C.J., Marullo, S., Minnett, P.J., Pennybacker, M., Ramakrishnan, B., Ramsankaran, R., Santoleri, R., Sunder, S., Saux Picart, S., Vázquez-Cuervo, J., Wimmer, W., 2019. Observational Needs of Sea Surface Temperature. Front. Mar. Sci. 6, 420. https://doi.org/10.3389/fmars.2019.00420

Pasula, A., Sil, S., 2019. Validation of Multi-Scale Ultra-High Resolution (MUR) Sea Surface Temperature with Coastal Buoys Observations and Applications for Coastal Fronts in the Bay of Bengal. pp. 1–4. https://doi.org/10.23919/URSIAP-RASC.2019.8738356

Qin, H., Chen, G., Wang, W., Wang, D., Zeng, L., 2014. Validation and application of MODIS-derived SST in the South China Sea. Int. J. Remote Sens. 35, 11–12. https://doi.org/10.1080/01431161.2014.916439

Stammer, D., Wentz, F., Gentemann, C., 2003. Validation of Microwave Sea Surface Temperature Measurements for Climate Purposes. J. Clim. 16, 73–87. https://doi.org/10.1175/1520-0442(2003)016<0073:VOMSST>2.0.CO;2

Vazquez-Cuervo, J., Castro, S.L., Steele, M., Gentemann, C., Gomez-Valdes, J., Tang, W., 2022. Comparison of GHRSST SST Analysis in the Arctic O
cean and Alaskan Coastal Waters Using Saildrones. Remote Sens. 14, 692. https://doi.org/10.3390/rs14030692

Vazquez-Cuervo, J., García-Reyes, M., Gómez-Valdés, J., 2023. Identification of Sea Surface Temperature and Sea Surface Salinity Fronts along the California Coast: Application Using Saildrone and Satellite Derived Products. Remote Sens. 15, 484. https://doi.org/10.3390/rs15020484

Vazquez-Cuervo, J., Gomez-Valdes, J., Bouali, M., 2020. Comparison of Satellite-Derived Sea Surface Temperature and Sea Surface Salinity Gradients Using the Saildrone California/Baja and North Atlantic Gulf Stream Deployments. Remote Sens. 12, 1839. https://doi.org/10.3390/rs12111839

Vazquez-Cuervo, J., Gomez-Valdes, J., Bouali, M., Miranda, L., Van der Stocken, T., Tang, W., Gentemann, C., 2019. Using Saildrones to Validate Satellite-Derived Sea Surface Salinity and Sea Surface Temperature along the California/Baja Coast. Remote Sens. 11, 1964. https://doi.org/10.3390/rs11171964

Vazquez-Cuervo, J., Torres, H.S., Menemenlis, D., Chin, T., Armstrong, E.M., 2017. Relationship between SST gradients and upwelling off Peru and Chile: model/satellite data analysis. Int. J. Remote Sens. 38, 6599–6622. https://doi.org/10.1080/01431161.2017.1362130

Wentz, F.J., Gentemann, C., Smith, D., Chelton, D., 2000. Satellite Measurements of Sea Surface Temperature Through Clouds. Science 288, 847–850. https://doi.org/10.1126/science.288.5467.847

Xiu, P., Chai, F., Curchitser, E.N., Castruccio, F.S., 2018. Future changes in coastal upwelling ecosystems with global warming: The case of the California Current System. Sci. Rep. 8, 2866. https://doi.org/10.1038/s41598-018-21247-7

Xu, F., Ignatov, A., 2014. In situ SST Quality Monitor (iQuam). J. Atmospheric Ocean. Technol. 31, 164–180. https://doi.org/10.1175/JTECH-D-13-00121.1

5. Fine spatial resolution topsoil organic matter mapping using UAV-borne hyperspectral data: A preliminary study

Abstract

Soil organic matter (SOM) is one of the main indicators of soil productivity and it improves soil fertility and its chemical, physical, and biological state. Extraction of SOM using traditional laboratory chemical analysis or image spectroscopy is labor-intensive, and expensive, and provides SOM estimations only at specific point locations. Therefore, there is a need for new technologies that can map soil parameters and their spatial variabilities at high spatial resolutions in less time and lower costs. Uncrewed aerial vehicle (UAV) technology combined with hyperspectral spectrometers is becoming a promising technology for the rapid mapping of topsoil at fine spatial scales. In this study, we are using a UAV-borne hyperspectral system in the visible and near-infrared to map topsoil organic matter over a Swiss agricultural field site at a fine scale of 7cm. Fourteen soil samples were acquired and combined with the minimum distance spectral algorithm applied on the hyperspectral data before and after data pre-processing techniques, to calibrate linear regression models for SOM prediction. Results show good and similar performance for all the models, with RMSE of prediction between 3.81-3.85% and R^2 between 0.74-0-75. The SOM map shows big variations within the field site and comparison with a coarser map based on data from the whole season confirms the high spatiotemporal variability of the soil in our study area. Our insights allow for deriving important recommendations on the use of the UAV-hyperspectral system for soil mapping for future studies in terms of data acquisition and processing.

5.1 Introduction

Soil organic matter (SOM) is the main source of soil nutrients and the key to a healthy soil (Six et al., 2000; Six and Paustian, 2014; Tiessen et al., 1994). It consists of any plant or animal material that returns to the soil at various stages of decomposition. SOM is very important for the soil's chemical, physical and biological state. It provides habitat to organisms living in the soil by improving the soil's capacity to store and supply essential nutrients. It also improves the soil structure, water infiltration, and the water-holding capacity of the soil. From the biological aspect, SOM's main component is carbon (C), which is a big source of energy for microorganisms in the soil, increasing biodiversity. Therefore, the rapid and accurate estimation of SOM and its spatial variation is crucial for monitoring the soil quality and improving the agricultural management and sustainability (Francos et al., 2021; Shen et al., 2020).

Conventional laboratory chemical analysis is used to extract SOM content, but it is time-consuming, laborious, expensive, and provides data only at specific point locations.

Besides the conventional laboratory chemical analysis, visible (VIS) and near-infrared (NIR) spectroscopy has been used to estimate simultaneously various physical parameters of the soil within less time (Cezar et al., 2019; Francos et al., 2021; Reeves et al., 2002; Shen et al., 2020; Shi et al., 2014; Summers et al., 2011). However, point spectroscopy measurements are time-consuming and limited to measurements only at specific locations. Therefore, they do not offer spatial variability information since they do not offer to map of the area of interest. Therefore, there is a need for a new technology that can map the soil at big spatial extents and not only at point locations, within less time and at low costs. Also, the sustainable management of individual field sites needs to be able to map small-scale spatial patterns of the different soil parameters (Hbirkou et al., 2012). Uncrewed aerial vehicles (UAVs) are an evolving technology that can offer rapid mapping of soil parameters and their spatial variability at high spatiotemporal resolutions using imaging spectrometers mounted on them.

Image spectroscopy in VIS, NIR, and middle infrared (MIR) offers benefits against point-based measurements and laboratory analysis (Ben-Dor et al., 2009; Chabrillat et al., 2019). More precisely, the output is an image and can lead to the extraction of a spatially continuous map of the soil parameters such as soil organic carbon (Askari et al., 2018) and SOM (Reis et al., 2021). Also, image spectroscopy acquires less fieldwork and data acquisition time.

The rapid evolution of remote sensing systems such as hyperspectral sensors is allowing the capture of spectral information in VIS, NIR, and MIR with high spatial and spectral resolution.
Many methods have been used to associate hyperspectral information either from spectroscopy or from imagery with SOM and other soil organic properties. Some of them include the Partial Least Squares Regression (PLSR) (Bai et al., 2022; Hbirkou et al., 2012; Reis et al., 2021; Selige et al., 2006; Shen et al., 2020), Principal Component Analysis regression (PCAR) (Chang et al., 2001; Fox and Metla, 2005) and machine learning (Bai et al., 2022; Ge et al., 2019). Also, recent studies combined imaging and non-imaging sensors to predict SOM and soil organic carbon using PLSR (Guo et al., 2019; Nanni et al., 2021).

However, hyperspectral data are associated with various noise sources, so the implementation of a data preprocessing workflow is crucial for the accuracy of the calibration models (Liu et al., 2019; Qiao et al., 2017). Different data pre-processing techniques are applied to the hyperspectral spectra before proceeding to the calibration, for noise removal purposes such as the Savitzky-Golay filter (Cezar et al., 2019; Ge et al., 2019; Shen et al., 2020), the Multiplicative Scatter Correction (MSC) (Zhou et al. 2014; Yang et al. 2021) and the first and second derivatives (Qiao et al., 2017). Pre-processing techniques are also applied to reduce reductant information on the hyperspectral data, such as the Principal Component Analysis (PCA) (Reis et al., 2021) and the discriminant analysis (Reis et al., 2021).

Airborne platforms (crewed aircraft) have already been used with hyperspectral sensors for soil mapping in high spatial resolutions (Guo et al., 2019; Selige et al., 2006; Stevens et al., 2010).
Recently, the use of UAVs for precision agriculture evolves rapidly. UAVs are more operationally flexible than crewed aircraft offering higher temporal resolutions and lower costs. With their ability

to map big areas at one acquisition while flying at low altitudes, they can map spatial variability of different soil parameters at high spatial resolutions.

UAV-borne hyperspectral imaging technology to map soil has already been a matter of study and has proved promising. The estimation of SOM from hyperspectral data is mostly based on the reflectance in the VIS and NIR. More precisely, the reflectivity of the soil decreases when the amount of SOM within the soil increases (Bartholomeus et al., 2008; Ben-Dor et al., 2009). Recent studies combine UAV-based hyperspectral imagery with machine learning to predict topsoil properties: Yang et al., 2021 using extreme learning machine mapped soil organic matter in 400 to 1000 nm with 10cm spatial resolution.
Ge et al., 2021, 2019 using hyperspectral data in the same wavelengths with an even higher spatial resolution of 4cm and using 70 topsoil samples, predicted soil moisture content using the random forest method and extreme learning machine (2019) as well as the extreme gradient boost algorithm (2021). Mészáros et al., 2020 predicted the soil organic carbon content using the Random Forest algorithm.

Before the data preprocessing for noise removal and extraction of accurate radiometric information from hyperspectral data, as analyzed in the previous paragraph, the design of accurate flight planning affects the data quality in the case of the UAV studies. Accurate flight planning can minimize the shifts of the UAV, assisting in accurate data acquisition and minimizing the errors within the images related to the topography and the scanning angle. Hence, in this current study, the UAV data acquisition workflow is analyzed to assist similar future UAV-borne hyperspectral studies.

In this current study, we are focusing on fine-scale (7cm) SOM mapping using hyperspectral data and laboratory-based SOM analysis. Our study is the first to map topsoil organic matter and its spatial variability at the fine spatial resolution of 7cm using a UAV-borne hyperspectral system. We are using the wavelengths of 453.03 to 927.12 (VIS to NIR) since they are the bands associated with the study of SOM.
More precisely, the objectives of the study are the followings:

- The ability of the UAV-borne hyperspectral imagery system to accurately predict SOM and its spatial variability at the fine scale of 7cm
- Use of the hyperspectral properties and laboratory-measured SOM to calibrate linear regression models that can predict SOM

5.2 Methods

5.2.1 The study site

The study area is located at Kerzers, part of the Seeland region of Switzerland. The Seeland region is located in the southeast of the Jura mountains, surrounded by three lakes and it is considered one of the main agricultural regions of Switzerland.

The Kerzers study site is located at 46°58'56.145"N, 7°10'15.026"E at approximately 432 m above mean sea level. It encompasses a mostly bare-soil area of 60*200 meters with soil type varying between sand and clay. The choice of this specific field site was made because of the variation in SOM that it offers that could serve the needs of this study for mapping the SOM variation in high spatial resolutions.

Figure 26: Location of the field site on the Swiss map (source: https://map.geo.admin.ch) (a); Field site area in red polygon (source: https://map.geo.admin.ch) (b); The state of the field site on the day of hyperspectral data acquisition (10th of August 2021) (c); Sampling bricks and the four sampling locations(in red color) at each side of the brick (d); The UAV-borne hyperspectral system (e).

5.2.2 Hyperspectral data acquisition

Hyperspectral data were acquired on the 10th of August 2021 using an AisaKestrel10 pushbroom sensor from Specim SA. The hyperspectral sensor operates in wavelengths between 395.55-1002.4 nm, with a spectral resolution of 3.41 nm. The sensor was mounted on a twelve-motor multicopter from Altigator SA. The hyperspectral push broom sensor weighs approximately 4 kilos and operates using the battery capacity of the UAV. AisaKestrel10 has an integrated GNSS/IMU xNAV500 unit made by Oxford Technical Solutions Limited.

For the hyperspectral data acquisition of this study, the flight plan consisted of four flying lines of 200m in length, and the distance between them was set to 26 m. The distance of 26 m between the flying lines and the flying altitude of 49 m above ground were chosen so as with the field of view of 100 deg of the sensor to achieve a spatial resolution of 7 cm. The flight took place during wind-free, sunny, and clear-sky conditions. The duration of the flight was limited to 8-9 minutes, due to the increased capacity consumption of the sensor.

5.2.3 Soil sampling

Fourteen bricks were placed at sampling locations within the field site where the soil was not uniform to represent areas with different amounts of SOM. The acquisition of the soil samples was important for the calibration of a model that could predict the SOM in combination with the hyperspectral data. The bricks to be identified in the hyperspectral images were marked with a reflective tape with almost 100% reflectivity in the spectral bands of the sensor.
At each brick/sampling location, we collected four samples at 10 cm from each of the four sides of the brick at 0-5cm depth. These four samples were then mixed as one sample to represent each brick/sampling location. We proceeded the same for all the fourteen bricks/sampling locations.
The soil sampling took place on the 11th of August 2021, and low grass was covering the soil at some parts of the field site. On the day of the soil sampling, the soil had approximately 40-50% moisture content. The mean, the standard deviation, and the coefficient of variation of the SOM and the water content as measured in the fourteen samples in the lab are mentioned in Table 1.

	SOM (%)	WC (%)
Mean (%)	41.84	46.43
Standard deviation (%)	7.91	5.35
Coefficient of variation	0.19	0.12

Table 1: Mean, standard deviation, and coefficient of variation in soil organic matter and in water content (in %) for the fourteen soil samples as measured in the lab.

5.2.4 Auxiliary data acquisition

Optical imagery was acquired using a SODA 3D sensor mounted on an EbeeX fixed-wing UAV from Sensefly to extract a high-resolution orthomosaic of the study area. The optical-based high-resolution orthomosaic was used for the identification of the bricks/sampling locations. The fixed-

wing flight took place at 124 m above ground to achieve a spatial resolution of 2.8 cm. The flight took place on the same day as the hyperspectral data acquisition (10th of August 2021) and under the same weather conditions.

LiDAR data were also acquired using a Yellowscan Mapper II sensor mounted on the multicopter to provide a high-resolution (30 cm) digital elevation model of the study area. The high-resolution digital elevation model was used for the orthorectification of the hyperspectral data, as described in the following section (section 5.2.5.1). A LiDAR UAV flight was performed at 30m above the ground at a constant flying speed of 3 m/s to achieve a point density of approximately 90 points per m^2.

Differential Global Position System (dGPS) measurements were acquired in the middle of the fourteen bricks to extract the coordinates of the sampling locations. The fourteen sampling points were also used as ground control points for improving the georeferencing of the RGB-based orthomosaic.
For performing later the radiometric correction within the hyperspectral images, we placed on the field four bricks fully covered with the reflective tape. These four bricks acted as ‘‘white reference targets’’ for the conversion from radiance to reflectance.

5.2.5. Remote sensing data processing

5.2.5.1. Hyperspectral data processing

The four scanning lines acquired from the four flying lines of the push broom sensor were automatically processed within CaliGeoPRO software (Specim, 2021) to produce four images of the field site. The four images were radiometrically and geometrically corrected also within CaliGeoPRO. For the radiometric calibration, the raw digital number values were converted to radiance values using the sensor calibration files provided by the sensor manufacturer. The geometric correction for eliminating the distortions due to the sensor was performed using the sensor’s characteristics also provided by the manufacturer.
To orthorectify the images to eliminate errors imposed by the topography, we used the LiDAR-derived digital elevation model on CaliGeoPRO.

The radiometrically and geometrically corrected output images were extracted in radiance values. For converting them to reflectance to represent the property of the soil without the effect of the position of the sensor or the illumination conditions, we used the radiance values of the four white reference targets we had placed on the field. Each white reference target was visible in one image. For each of the four radiance images, we divided the image radiance values by the maximum radiance of the corresponding white reference target and the output was the four images in reflectance values.
We should mention here that because of the 49m flying height of the UAV, the interferences from the atmosphere are considered negligible, so we did not proceed to any atmospheric correction.

To extract the SOM map, we created the mosaic by stitching the four reflectance images to get a complete orthorectified field site map. The mosaic was created within the ENVI software (ENVI Harris Geospatial Solutions, 2021) using the nearest neighbor resampling method.

Extra data processing steps were performed on the hyperspectral mosaic for noise removal purposes. We performed the removal of the marginal bands (bands 395.55-449.64nm and 930.55-1002.4nm) since they were introducing a lot of noise that could be identified as strips within the mosaic. Additionally, we performed two different types of filtering separately: In the spatial domain, we applied a 3-by-3 median filter to eliminate the ‘‘salt and paper noise’’ that existed in some parts of the mosaic. By‘‘salt and paper noise’’ we define a few pixels which are very noisy within the image, resulting in sprinkling white and black dots called ‘‘salt and pepper’’ within the image. In the spectral domain, we applied separately a first-order and second-order Savitzky-Golay polynomial filter (Savitzky and Golay, 1964) to smooth the spectral signal by removing the high frequencies. More precisely, the Savitzky-Golay filtering of a 3-by-3 spectral window was applied to minimize the noise that was identified as ‘‘sparks’’ at some bands for some pixels. The three mosaics after the application of the abovementioned filters as well as the unprocessed mosaic were used as a base for the statistical analysis that follows in section 5.2.7.

The soil samples were associated with the corresponding pixels within the mosaic for the model calibration that would predict the SOM at the unsampled areas using the spectral properties of the mosaic. In the mosaic, the fourteen bricks/sampling locations were identified as areas with white pixels since they were covered with reflective tape, as described in section 5.2.3. For each of the fourteen white pixel areas, we picked four pixels with very similar spectral signatures within the mosaic. The four pixels were chosen at a distance of 2 pixels (around 14cm) from each side of the white pixel areas (north, south, east, west) since for the soil sampling we also sampled at a 10 cm distance from each side of each brick (see Figure 26d). The mean reflectance of the four pixels was then assigned as the spectral signature of each of the fourteen sampling locations.

5.2.5.2. Optical imagery and LiDAR data processing

The optical images acquired using the SODA 3D were processed using the Pix4DMapper software (Pix4D, 2021). The images were stitched together using the structure from the motion method and the final output was the orthomosaic of the study area in the spatial resolution of 2.8 cm. To further improve the georeferencing of the orthomosaic, we used within PixD4Mapper the ground control points as we measured them with the dGPS in the middle of the bricks.

Regarding the processing of the LiDAR data, the position and altitude recordings of the Inertial Navigation System of the LiDAR were merged with the raw LiDAR returns and processed to a georeferenced point cloud. The procedure took place within the CloudStation software (YellowScan CloudStation, 2021). To further improve the georeferencing of the point cloud, the flight trajectory was post-processed using the data from a nearby (<2km) Global Navigation Satellite System base station from the continuously operating reference stations of the Swiss positioning system. This post-processing kinematic (PPK) correction was performed within the software POSPac UAV

(Applanix, 2019). The outcome of the PPK correction was the post-processed Smoothed Best Estimate Trajectory that was then used for improving the geolocation of the point cloud.

To derive the digital elevation model from the point cloud and use it for the orthorectification of the hyperspectral mosaic, an essential step was the identification of the points that correspond to the bare earth surface. These bare-earth points represent the real elevation of the field site, rather than the surface with the low vegetation/grass. Including the low vegetation/grass points in the extracting of the elevation model could lead to an overestimation of the real elevation of the study area. To extract the bare earth points we used the lasthin classification tool from LAStools software (Licensed Academic Version 190812, 2019). As bare-earth points were classified only as the points with the lowest elevation within a 30 by 30 cm spatially moving window. These classified bare-earth points were then gridded into a raster of 30cm pixel size which was the digital elevation model of the study area. The digital elevation model was afterward used within CaloGeoPRO to othorectify the mosaic.

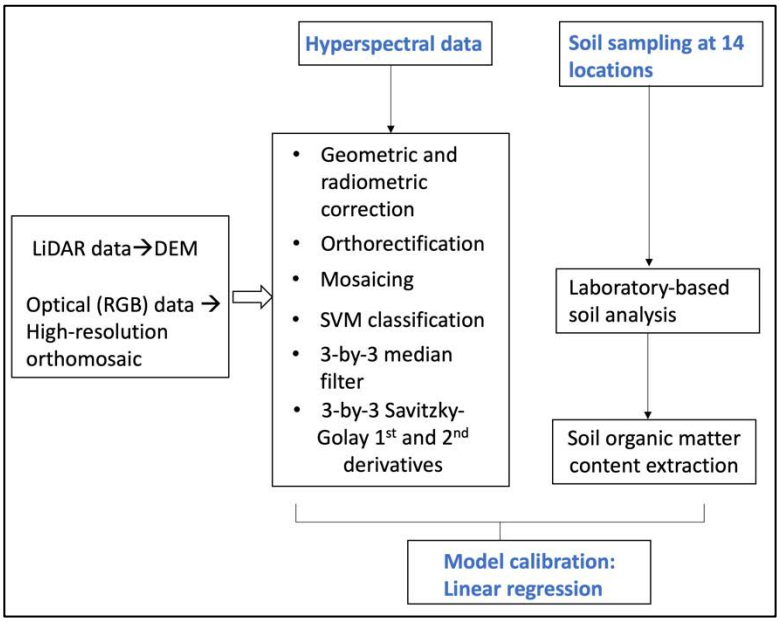

Figure 27: Workflow of the remotely sensed data processing and of the soil laboratory analysis for the model calibration to predict soil organic matter.

5.2.6 Laboratory soil analysis

The soil laboratory analysis took place according to the standard methods used in Switzerland for soil sampled with carbon content higher than 15 % (D-AS method). More information on the analysis can be found here: https://ira.agroscope.ch/de-CH/publication/46264. First, the samples were weighed and dried, and then their standard mass was used for the extraction of the water content and the calculation of the SOM. The SOM content within each soil sample was calculated as the mass difference between initial mass and ash mass. Finally, for each sample, we extracted the soil moisture content and the SOM (both in %). The soil moisture content was calculated to have an estimation of how wet the soil was during the data acquisition. The SOM values were used along

with the hyperspectral mosaic for calibrating a model to predict SOM for the unsampled areas. More details are mentioned in the following section.

5.2.7 Statistical analysis

For the extraction of the SOM map at 7cm resolution using the hyperspectral mosaic and the SOM laboratory-based values, we performed the following steps.
Firstly, the minimum distance spectral algorithm within ENVI was applied to all the fourteen samples using as a reference the soil sample with the highest reflectance which also corresponds to the soil sample with the lowest SOM content (soil sample number 15). Each soil sample was marked as a polygon/ Region Of Interest (ROI) within the mosaic (hereafter each soil sample will be referred to as ROI). The minimum distance spectral algorithm was applied to all the pixels within the mosaic using as a reference the ROI with the highest reflectance (ROI 15). The minimum distance algorithm calculates the Euclidean distance from each pixel to the mean of the ROI15. The result of the algorithm is a map containing the minimum distance to ROI15 for each pixel at the spatial resolution of 7cm. We used the mean calculated distance of all the pixels within each ROI, and this mean value was the minimum distance of each ROI to the reference ROI (ROI15) that was used afterward for the statistical analysis.

To calibrate a model that predicts SOM from the hyperspectral data, we run a linear regression using as y (dependent variable) the SOM-laboratory-based value of each sample/ROI and as x (independent variable) the minimum distance to ROI15, as it was calculated at the previous step. To evaluate the performance of the model considering the limited amount of training data we had available, we performed leave-one-out cross-validation (LOOCV). The prediction accuracy of the model was assessed in terms of the root mean squared error of cross-validation ($RMSE_{cv}$), the mean absolute error of cross-validation (MAE_{CV}), the root mean squared error of prediction ($RMSE_P$), the coefficient of determination (R^2), and the Ratio of Performance to Deviation (RPD).

To extract the SOM map of the area, we had to apply the equation derived from the linear regression to the soil pixels of the mosaic. Therefore, we had to separate the soil pixels from the grass/low vegetation pixels. To do so, support vector machine (SVM) classification was performed within ENVI using as training datasets the soil and grass/low vegetation areas we identified within the mosaic.
The evaluation of the classification's performance was assessed by calculating the confusion matrix and the emission and omission errors of the classification. We used the optical-based high-resolution orthomosaic to define the validation datasets. Within the optical-based orthomosaic, we chose areas of soil and grass/low vegetation that we could very precisely identify. Since the optical-based orthomosaic was very well registered to the hyperspectral mosaic, we identified the same areas within the hyperspectral mosaic. These areas were then used as validation datasets for the calculation of the confusion matrix and emission and omission errors.

The linear regression model was finally applied to the soil pixels and the SOM map of the area at 7cm resolution was extracted.

The same workflow (model prediction and SOM extraction) was applied to the mosaics after the application of the spatial and spectral filters (see section 5.2.5.1), to see how the pre-processing of the hyperspectral data affects the prediction of the SOM. The comparison of the four different models calibrated on the four mosaics is mentioned in the results section (section 5.3.1).

5.3 Results and Discussion

5.3.1 Statistical analysis and soil organic matter map

The limited amount of training data is the main restriction of our study. However, the models' evaluation using the leave-one-out cross-validation indicated good accuracies of the calibration models. The four models calibrated on the different mosaics gave very similar results in terms of $RMSE_{cv}$, MAE_{cv}, R^2, RPD, and $RMSE_P$. The results are shown in
Table **2**. The coefficients of the linear regression shown also in
Table **2** were applied on the minimum distance algorithm map at each pixel, and the SOM map at 7cm spatial resolution was extracted.

	mosaic	mosaic median filter	mosaic Sav-Gol 1st der.	mosaic Sav-Gol 2nd der.
RMSEcv	4.51	4.37	4.52	4.52
MAEcv	3.44	3.51	3.45	3.45
$RMSE_P$	3.84	3.81	3.85	3.85
R^2	0.75	0.75	0.74	0.75
RPD	1.69	1.75	1.69	1.69
y=a*x+c0	y=15.58*x+25.66	y=14.65*x+25.75	y=15.49*x+25.82	y=15.51*x+25.78

Table 2: Leave-one-out-cross validation and linear regression models' predictions accuracies.

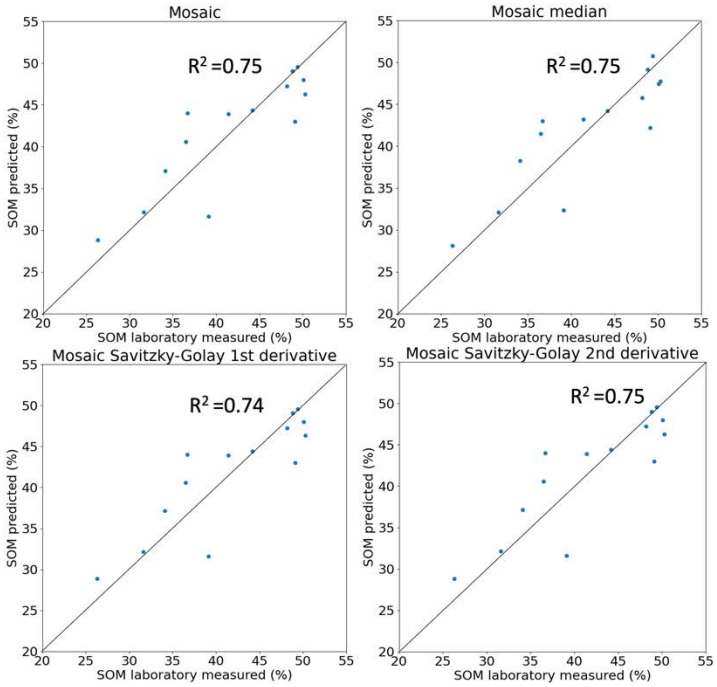

Figure 28: Scatterplots laboratory-measured against predicted soil organic matter for the four mosaics.

In

Table **2** we see that the regression models for soil organic matter prediction were statistically significant (p-value ≤ 0.05). The SOM measured in the laboratory gave a mean of 41.8% and our linear regression model predicted SOM with $RMSE_{CV}$=3.44 $RMSE_P$=3.84, R^2=0.75, and RPD=1.69 for the mosaic without any data preprocessing. The results for the other three mosaics are very similar. The RPD values of the models range between 1.69 and 1.75, which show a medium prediction ability (Chang et al., 2001). The R^2 values of 0.74 and 0.75 show that 74-75% of the variance in the laboratory-measured SOM is explained by the independent variable (minimum distance to the soil sample with the highest reflectivity).

Our results compared to previous studies are promising, despite the limited number of samples we had to calibrate our linear regression model. Reis et al., 2021 using the wavelengths 380 to 2506nm applied PLSR to predict SOM, they derived R^2 = 0.75, RMSE = 3.44 g $kg^{-1,}$ and RPD = 2.1, with an average SOM content of 26.32 g kg^{-1} within 384 samples.

Shen et al., 2020 applied different data pre-processing techniques in the VIS, NIR, and MIR and the best one using PLSR gave RMSE of validation=0.280, $R^2$0.713, and RPD=1.712 with an average value within 198 samples of SOM=2.2%.

Selige et al., 2006 predicted soil organic carbon in the spectrum range of 420-2480nm from 72 samples. They used both multiple linear regression and the PLSR approach with soil organic carbon range between 0.7% and 3.85%. PLSR gave R^2=0.9 and $RMSE_{cv}$=0.29% and multiple linear regression gave R^2=0.86 and $RMSE_{cv}$=0.22%.

Nanni et al., 2021 also used different PLSR models on 66 samples with a spectrum range of 380-2500nm, predicted SOM with R^2 bigger than 0.67 with mean SOM of 8.26gdm^{-3}.

Whereas in the case of our data, the hyperspectral data pre-treatment methods gave very similar results to the original data (mosaic without any filter applied), the study of (Shen et al., 2020) showed much better results when different data pre-treatment methods were applied to the hyperspectral data. Using PLSR for SOM estimation, they extracted 1.2% RMSEv = 1.2%, $R^{2=}$0.007, and 0.4 RPD whereas the most optimal pretreatment method gave 0.28%, 0.713, and 1.712, respectively. Selige et al., 2006 while predicting soil organic carbon also concluded that different data pre-treatments (min-max normalization, Savitzky-Golay derivatives, etc.) lead to very similar inaccuracies within the calibration models.

Figure 29 depicts the map extracted from the mosaic without the implementation of any of the filters. Big variations can be identified within the SOM map ranging between 26 to 60%. The areas with the smallest amount of SOM are located close to the center of the study area whereas in the south the SOM content reaches its highest value (60%). Also, in the center of the study area, there is an area with high SOM content (around 50%). In the north, the SOM content decreases with an average value of around 30%. The linear correlation between SOM and water moisture based on the fourteen laboratory-measured values showed a Rvalues^2 of 0.96. Therefore, as expected, areas with high SOM content coincide with areas with increased soil water holding capacity and hence with high soil moisture (Hudson, 1994). Indeed, within our study area, the areas close to the center and in the south were the areas with the highest amount of water which even made their accessibility difficult.

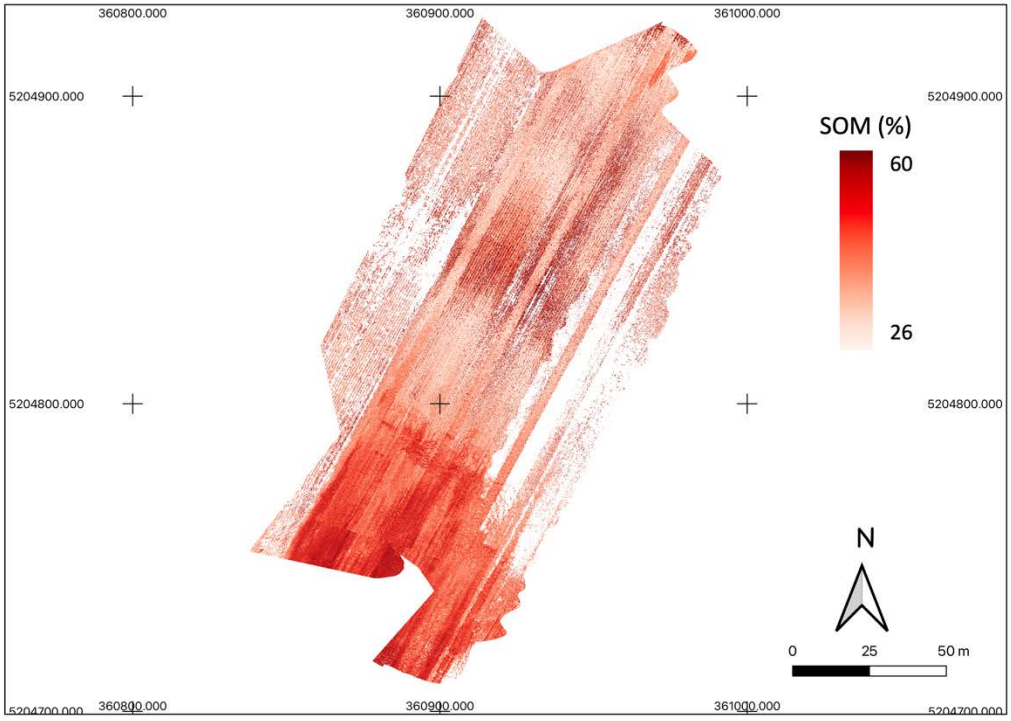

Figure 29: Soil organic matter map extracted from the mosaic (soil-only pixels) without any data pre-processing.

We performed a comparison of our SOM map with a SOM map of 2m derived from field estimation and lab data acquired within the whole year of 2021 (Nussbaum et al 2023). The 2m SOM map was

provided by the Bern University of Applied Sciences and the School of Agricultural, Forest, and Food Sciences.

More precisely, 2500 data from the Seeland area were used to calibrate a random forest to predict SOM using 50 different parameters (flow accumulation, curvature, elevation difference, height above groundwater level, etc.). To perform the comparison between our SOM predictions and the ones on the 2m map, we upscaled our 7cm resolution SOM map to 2m, by averaging all the SOM values within a 2-by-2 m moving average spatial window. The two maps are depicted in Figure **30**.

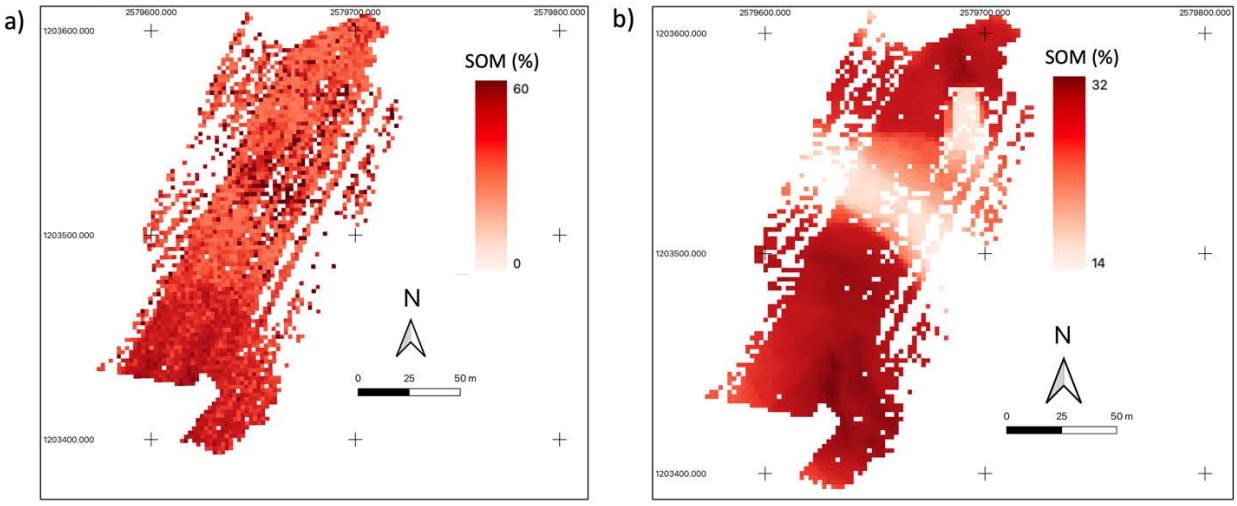

Figure 30: SOM map upscaled to 2m from our hyperspectral data (a); SOM map 2m provided from Bern based on data from the whole of 2021 for performing the comparison(b).

The differences in the SOM within the two maps are big within the whole study area, and the comparison showed an RMSE of around 17.39%. This RMSE value is high considering that the mean SOM as measured in the laboratory was 41.8%, in our upscaled SOM map is 38.47% and in the SOM map of 2m is 24.9%. The SOM content values in our map (

Figure 30**a) have a bigger range (0-60%) and reach much higher SOM content values than the 2m SOM map that was provided to us (**

Figure **30**b) which has a SOM content range of 14-32%. Despite the differences between the two maps, similar patterns can be identified between the two of them: There is a decrease in SOM content close to the center of the study area and an increase in the north and in the south.

The big differences between the 2m SOM map and our 2m upscaled map indicate that indeed the soil in our study area has a big variation in SOM that changes within the season according to the farmer's sowing schedule. Therefore, there is a need for frequent monitoring of the SOM within the season, especially before and after the farmers sowing the soil. We should also consider that our hyperspectral map was upscaled to be compared to the 2m spatial resolution map and that also included some averaging of the SOM values. Also, our SOM predictions are based on a specific state of the soil during the days of hyperspectral data acquisition and soil sampling: The soil was considerably humid (almost 50% moisture content), a state that does not represent the soil state

through the whole season. Within our linear regression models, the water content could not be parametrized and therefore was not taken into consideration for the prediction of the SOM.

Before the minimum distance algorithm that was used as the independent variable for the models to predict SOM, we tested different statistical analysis methods on our data similar to previous studies (Reis et al., 2021; Selige et al., 2006; Shen et al., 2020; Stevens et al., 2010). PLSR and regression tree methods using either all the bands of the hyperspectral mosaic or the PCA components were tested but did not perform successfully in our data due to the limited amount of training data. The first four PCA components were also used to perform multiple linear regression using only the soil pixels, but the p-value was high for all the independent variables. The addition of the water content as an independent variable aimed at improving the performance of the multiple linear regression model, but the p-value was also high for the PCA components. Minimum Noise Fraction Transform was applied on the soil pixels. The first 24 bands were used as independent variables for performing multiple linear regression, but the p-values were high as in the case of the PCA-based multiple linear regression. The main reason that could explain the failure of the abovementioned models is the limited amount of training data since we had only fourteen samples available. Consequently, we strongly recommend the acquisition of an adequate amount of soil samples to have a good amount of training, testing, and validation datasets for model calibration. Previous studies focusing on predicting topsoil parameters via hyperspectral data in VIS, NIR, and MIR used a big amount of soil samples to calibrate their models using different statistical methods: Stevens et al., 2010 acquired 325 soil samples to predict topsoil organic carbon, Reis et al., 2021 and Shen et al., 2020 to map SOM they used 384 and 213 samples, respectively. To map also SOM Selige et al., 2006 used a smaller amount of 72 soil samples, and Nanni et al., 2021 66 samples.

5.3.2 Data quality assessment

Despite the ‘‘strips’’ noise that was removed by discarding the marginal bands of the hyperspectral mosaic, the two different filters were also applied successfully to the mosaic. Whereas there were no significant differences within the accuracies of the calibration models between the original mosaic and the ones after the implementation of the filters, the filtered mosaic contained less amount of noise. More precisely, Savitzky-Golay's first and second derivatives successfully removed the high frequencies from the data and the final spectral signatures were much smoother. Savitzky-Golay filters also retained the shape of the original spectral signatures in contrast to the median filter which led to over/underestimation of the original spectral curves (Guiñón et al., 2007).

Regarding the geometry of the hyperspectral mosaic, there were some artifacts on the border of the mosaic. These artifacts were created probably due to remaining distortions even after the geometric corrections of the original four images or due to inaccuracies in the boresight calibration parameters of the hyperspectral sensor. Since the 14 sampling points are lying mainly in the center of the mosaic, these artifacts did not affect the results of this study.

The SVM classification confusion matrix gave satisfactory results for the use purposes of this study. The kappa coefficient that measures the agreement between classification and truth values (validation set) was 0.93 and we got 4.13% commission and 2.11% emission errors for the soil pixels.

The post-processing kinematic correction of the optical data along with the georeferencing using the 14 GCPs gave a mean RMSE of 0.032 m. Therefore, the optical-based orthomosaic can be considered accurate for use in the content of this study.
Regarding the LiDAR data, the flat terrain and the favorable weather conditions (wind-free flight) that did not cause extra shifts to the UAV, did not make the IMU performance more difficult. Therefore, there was no need for any extra processing steps regarding the strip adjustments after the PPK, as in Koutantou et al., 2021 which used the same UAV- borne LiDAR system in steep forested terrain. The LiDAR scanner recorded eventually mainly 1 return per pulse (rarely up to 2), despite the manufacturer's statement of up to three returns per pulse. However, the ability to fly close to the ground and achieve high point density did not allow the record of only 1 return to affect the quality of the point clouds in terms of data gaps.

5.3.3 Recommendations for future campaigns

The designing of an accurate flight planning that adjusts to the needs of each study (pixel size, side overlap, etc.) is crucial in the case of a push broom sensor. The heavy setup used in our study (UAV and hyperspectral camera) was not a constraint for the hyperspectral data acquisition since we only had to cover a small study area. However, the heavy setup can be a considerable constraint for future studies in the case of bigger study areas, requiring performing many flights to cover the whole area. Many flights require also the implementation of data co-registration methods which comes with many difficulties and might affect the accuracy of the final product (SOM map).
Nowadays more advanced sensors in terms of weight, size, and user-friendly functionalities are being designed and used with UAVs. These sensors can offer more flexibilities in data acquisition, such as increased flight duration and more straightforward use. Similarly, newly designed UAVs offer more flexibility in terms of size, weight, and operation. UAV manufacturers provide also nowadays more advanced software for flight planning and data processing, adjusting better to the needs of the pilots.

The use of big white reference targets well distributed within the study area is important for the accurate radiometric correction of the hyperspectral images. Since they are easily identified within the hyperspectral data, we recommend also measuring their absolute coordinates with a dGPS. These coordinates can serve also as GCPs to cover other needs of the study, for example, the evaluation of the orthorectification of the mosaic. The use of concrete bricks as reference/sampling targets was made to avoid being removed from the wind or any animal between the hyperspectral data acquisition day and the soil sampling day. A similar setup using targets made from cartons and covered by reflective tape could be easier to place in the field than the concrete bricks that we used. We also recommend avoiding placing the reference/sampling targets in the borders of the study area due to the reduced accuracy of the hyperspectral data in the borders.

As discussed in section 5.3.1, the use of big training, testing, and validation datasets for accurate model calibration is crucial for similar studies. Therefore, we strongly advise acquiring a considerable amount of soil samples, depending also on the needs of the statistical model used.

5.4 Conclusions

This study was the first one to map SOM at the fine scale of 7cm using a UAV-borne hyperspectral system. Linear regression models were calibrated using 14 laboratory-measured SOM values and the minimum distance spectral algorithm was applied to the hyperspectral data before and after the implementation of spatial and spectral filters. We derived promising results ($RMSE_P$ =3.81-3.84, R2=0.74-0.75, RPD=1.69-1.75) that also showed that the different data pre-processing methods applied to the hyperspectral data give very similar model predictions.

The prediction map showed big variability in SOM within the field site. Comparison with a 2m SOM map based on field predictions and models on data acquired within the whole year confirms the high spatial variability of the soil within the season. The high spatial variability of the soil indicates the need for frequent monitoring before and after the farmers' practices (soil sawing).

Our study derived also important recommendations for similar future studies aiming to map topsoil properties at high spatial resolutions. The use of many soil samples for accurate model calibration in combination with appropriate UAV-borne data acquisition planning can assist in the prediction and mapping of soil parameters, as well as their spatial distribution.

Acknowledgments

The UAV, hyperspectral, and LiDAR systems were funded by the Swiss National Science Foundation (SNSF, R'Equip grant 206021_170753). The project took place in collaboration with the Bern University of Applied Sciences, School of Agricultural, Forest and Food Sciences HAFL, and especially with Prof. Stéphane Burgos. Kalliopi Koutantou and Philip Brunner as the authors of this chapter were supported by the University of Neuchatel. The authors would like to thank Laurent Marguet from the University of Neuchatel for his assistance with the field work, and Roland Schaffluetzel and Madlene Nussbaum from the Bern University of Applied Sciences for performing the laboratory analysis of the soil samples and for providing the SOM map, respectively.

References

Applanix, 2019. POSPac UAV, Version 8.3, Licensed.

Askari, M.S., O'Rourke, S.M., Holden, N.M., 2018. A comparison of point and imaging visible-near infrared spectroscopy for determining soil organic carbon. Journal of Near Infrared Spectroscopy 26, 133–146. https://doi.org/10.1177/0967033518766668

Bai, Z., Xie, M., Hu, B., Luo, D., Wan, C., Peng, J., Shi, Z., 2022. Estimation of Soil Organic Carbon Using Vis-NIR Spectral Data and Spectral Feature Bands Selection in Southern Xinjiang, China. Sensors 22, 6124. https://doi.org/10.3390/s22166124

Bartholomeus, H.M., Schaepman, M.E., Kooistra, L., Stevens, A., Hoogmoed, W.B., Spaargaren, O.S.P., 2008. Spectral reflectance based indices for soil organic carbon quantification. Geoderma 145, 28–36. https://doi.org/10.1016/j.geoderma.2008.01.010

Ben-Dor, E., Chabrillat, S., Demattê, J.A.M., Taylor, G.R., Hill, J., Whiting, M.L., Sommer, S., 2009. Using Imaging Spectroscopy to study soil properties. Remote Sensing of Environment 113, S38–S55. https://doi.org/10.1016/j.rse.2008.09.019

CaliGeoPRO 2.3.1 software (Specim Inc, 2017)

Cezar, E., Nanni, M.R., Guerrero, C., da Silva Junior, C.A., Cruciol, L.G.T., Chicati, M.L., Silva, G.F.C., 2019. Organic matter and sand estimates by spectroradiometry: Strategies for the development of models with applicability at a local scale. Geoderma 340, 224–233. https://doi.org/10.1016/j.geoderma.2019.01.021

Chabrillat, S., Ben-Dor, E., Cierniewski, J., Gomez, C., Schmid, T., van Wesemael, B., 2019. Imaging Spectroscopy for Soil Mapping and Monitoring. Surv Geophys 40, 361–399. https://doi.org/10.1007/s10712-019-09524-0

Chang, C.-W., Laird, D.A., Mausbach, M.J., Hurburgh, C.R., 2001. Near-Infrared Reflectance Spectroscopy–Principal Components Regression Analyses of Soil Properties. Soil Science Society of America Journal 65, 480–490. https://doi.org/10.2136/sssaj2001.652480x

Fox, G.A., Metla, R., 2005. Soil Property Analysis using Principal Components Analysis, Soil Line, and Regression Models. Soil Science Society of America Journal 69, 1782–1788. https://doi.org/10.2136/sssaj2004.0362

ENVI Harris Geospatial Solutions, Version 5.6, Licensed

Francos, N., Ogen, Y., Ben-Dor, E., 2021. Spectral Assessment of Organic Matter with Different Composition Using Reflectance Spectroscopy. Remote Sensing 13, 1549. https://doi.org/10.3390/rs13081549

Ge, X., Ding, J., Jin, X., Wang, J., Chen, X., Li, X., Liu, J., Xie, B., 2021. Estimating Agricultural Soil Moisture Content through UAV-Based Hyperspectral Images in the Arid Region. Remote Sensing 13, 1562. https://doi.org/10.3390/rs13081562

Ge, X., Wang, J., Ding, J., Cao, X., Zhang, Z., Liu, J., Li, X., 2019. Combining UAV-based hyperspectral imagery and machine learning algorithms for soil moisture content monitoring. PeerJ 7, e6926. https://doi.org/10.7717/peerj.6926

Guiñón, J., Ortega, E., García-Antón, J., Pérez-Herranz, V., 2007. Moving average and Savitzki-Golay smoothing filters using Mathcad.
Guo, L., Zhang, H., Shi, T., Chen, Y., Jiang, Q., Linderman, M., 2019. Prediction of soil organic carbon stock by laboratory spectral data and airborne hyperspectral images. Geoderma 337, 32–41. https://doi.org/10.1016/j.geoderma.2018.09.003

Hbirkou, C., Pätzold, S., Mahlein, A.-K., Welp, G., 2012. Airborne hyperspectral imaging of spatial soil organic carbon heterogeneity at the field-scale. Geoderma 175–176, 21–28. https://doi.org/10.1016/j.geoderma.2012.01.017

Hudson, B.D., 1994. Soil organic matter and available water capacity. Journal of Soil and Water Conservation 49, 189–194.

LAStools, Academic Version 190812, 2019. Licensed.

Liu, Yi, Liu, Yaolin, Chen, Y., Zhang, Y., Shi, T., Wang, J., Hong, Y., Fei, T., Zhang, Y., 2019. The Influence of Spectral Pretreatment on the Selection of Representative Calibration Samples for Soil Organic Matter Estimation Using Vis-NIR Reflectance Spectroscopy. Remote Sensing 11, 450. https://doi.org/10.3390/rs11040450

Mészáros, J., Jakab, G., Árvai, M., Szabó, J., Tóth, M., Keller, B., Szatmári, G., Szalai, Z., Pásztor, L., 2020. Predicting topsoil organic carbon using UAV-based hyperspectral sensor (No. EGU2020-9324). Presented at the EGU2020, Copernicus Meetings. https://doi.org/10.5194/egusphere-egu2020-9324

Nanni, M.R., Demattê, J.A.M., Rodrigues, M., Santos, G.L.A.A. dos, Reis, A.S., Oliveira, K.M. de, Cezar, E., Furlanetto, R.H., Crusiol, L.G.T., Sun, L., 2021. Mapping Particle Size and Soil Organic Matter in Tropical Soil Based on Hyperspectral Imaging and Non-Imaging Sensors. Remote Sensing 13, 1782. https://doi.org/10.3390/rs13091782
Nussbaum, M., Oechslin, S., Burgos, S.: Kartenerstellung aus vorhandenen Bodenaufnahmen. Technische Unterstützung Kartierung organische Böden Grosses Moos (BOKA Seeland). Hochschule für Agrar-, Forst- und Lebensmittelwissenschaften, Zollikofen, 2023.

Pix4D SA, 2022, Version 4.6.4, Licensed

Qiao, X.-X., Wang, C., Feng, M.-C., Yang, W.-D., Ding, G.-W., Sun, H., Liang, Z.-Y., Shi, C.-C., 2017. Hyperspectral estimation of soil organic matter based on different spectral preprocessing techniques. Spectroscopy Letters 50, 156–163. https://doi.org/10.1080/00387010.2017.1297958

Reeves, J., McCarty, G., Mimmo, T., 2002. The potential of diffuse reflectance spectroscopy for the determination of carbon inventories in soils. Environmental Pollution 116, S277–S284. https://doi.org/10.1016/S0269-7491(01)00259-7

Reis, A.S., Rodrigues, M., Alemparte Abrantes dos Santos, G.L., Mayara de Oliveira, K., Furlanetto, R.H., Teixeira Crusiol, L.G., Cezar, E., Nanni, M.R., 2021. Detection of soil organic matter using hyperspectral imaging sensor combined with multivariate regression modeling procedures. Remote Sensing Applications: Society and Environment 22, 100492. https://doi.org/10.1016/j.rsase.2021.100492

Savitzky, Abraham., Golay, M.J.E., 1964. Smoothing and Differentiation of Data by Simplified Least Squares Procedures. Anal. Chem. 36, 1627–1639. https://doi.org/10.1021/ac60214a047

Selige, T., Böhner, J., Schmidhalter, U., 2006. High resolution topsoil mapping using hyperspectral image and field data in multivariate regression modeling procedures. Geoderma 136, 235–244. https://doi.org/10.1016/j.geoderma.2006.03.050

Shen, L., Gao, M., Yan, J., Li, Z.-L., Leng, P., Yang, Q., Duan, S.-B., 2020. Hyperspectral Estimation of Soil Organic Matter Content using Different Spectral Preprocessing Techniques and PLSR Method. Remote Sensing 12, 1206. https://doi.org/10.3390/rs12071206

Shi, Z., Wang, Q., Peng, J., Ji, W., Liu, H., Li, X., Viscarra Rossel, R.A., 2014. Development of a national VNIR soil-spectral library for soil classification and prediction of organic matter concentrations. Sci. China Earth Sci. 57, 1671–1680. https://doi.org/10.1007/s11430-013-4808-x

Six, J., Elliott, E.T., Paustian, K., 2000. Soil Structure and Soil Organic Matter II. A Normalized Stability Index and the Effect of Mineralogy. Soil Science Society of America Journal 64, 1042–1049. https://doi.org/10.2136/sssaj2000.6431042x

Six, J., Paustian, K., 2014. Aggregate-associated soil organic matter as an ecosystem property and a measurement tool. Soil Biology and Biochemistry 68, A4–A9. https://doi.org/10.1016/j.soilbio.2013.06.014

Stevens, A., Udelhoven, T., Denis, A., Tychon, B., Lioy, R., Hoffmann, L., van Wesemael, B., 2010. Measuring soil organic carbon in croplands at regional scale using airborne imaging spectroscopy. Geoderma, Diffuse reflectance spectroscopy in soil science and land resource assessment 158, 32–45. https://doi.org/10.1016/j.geoderma.2009.11.032

Summers, D., Lewis, M., Ostendorf, B., Chittleborough, D., 2011. Visible near-infrared reflectance spectroscopy as a predictive indicator of soil properties. Ecological Indicators, Spatial information and indicators for sustainable management of natural resources 11, 123–131. https://doi.org/10.1016/j.ecolind.2009.05.001

Tiessen, H., Cuevas, E., Chacon, P., 1994. The role of soil organic matter in sustaining soil fertility. Nature 371, 783–785. https://doi.org/10.1038/371783a0

Yang, X., Bao, N., Li, W., Liu, S., Fu, Y., Mao, Y., 2021. Soil Nutrient Estimation and Mapping in Farmland Based on UAV Imaging Spectrometry. Sensors 21, 3919. https://doi.org/10.3390/s21113919

YellowScan CloudStation, 2021. Version 1.18.0, Licensed.

6. Thesis Conclusions and Outlook

This final chapter summarizes the contributions this Ph.D. thesis offers to the remote sensing community. Also, the challenges and potentials of UAVs to resolve fine-scale hydrogeological processes in various environments are described as they are derived from this thesis. Since the biggest part of the thesis was conducted using UAVs, this chapter mainly focuses on the UAVs' potential and less on the potential of the USVs. Technical challenges of the use of UAVs are also addressed, deriving recommendations for further studies.

6.1 Contributions of the Ph.D. thesis

This Ph.D. thesis, focusing on the use of uncrewed vehicles for various hydrogeological studies mainly in Switzerland but also in California, offers innovative contributions to the field of remote sensing. The use of uncrewed vehicles in hydrogeological applications is considered challenging. This thesis by integrating data from multiple sensors and platforms manages to resolve some of these technological challenges and offers a comprehensive view of how uncrewed vehicles can improve the study of different hydrogeological parameters.
The thesis goes beyond the existing coarse spatiotemporal resolutions of many alternative remote sensing platforms and the limitations of traditional in situ observations. We also derived new datasets for the scientific community in environments that had not been mapped in the past with UAVs due to increased UAV operational risk but also due to the demanding data processing workflow over such terrain.

More precisely, our snow study over the flat and steep forests (chapter 2) derived important recommendations for future forest snow studies using UAVs specializing in the data processing workflow over such environments. The snow study over the two steep forests (chapter 3) is the first-ever study made using a UAV-borne LiDAR in such an environment. We successfully derived snow maps of 1m spatial resolution and taking advantage of the temporal resolution UAVs offer, we did a seasonal snow pattern analysis by conducting multiple campaigns within one winter season. Additionally, the findings of our study related to the dependency of the snow forest dynamics on the canopy structure and topography are very useful for the development of future hyper-resolution snow models. Future studies can use the technical recommendations derived from both our snow studies for improving their flight planning, UAV operation, and data processing workflow according to our insights.

The ocean sea surface temperature study (chapter 4) is the first study to compare MODIS level-2 with MUR level-4 SST products over the California Coast. It is also the first study to validate MODIS level-2 quality levels over the California Coast. Our study was based on data acquired from the promising technology of the Saildrone and proved that the high spatiotemporal sampling capabilities of this technology can tackle the limited and low-quality observational data in coastal areas. The kriging interpolation method applied introduces a way to generate in-situ data in areas such as those away from the coast where there is a lack of in-situ observations. Such interpolation

method has the potential to be improved using for example the correlation between in-situ and satellite data. Also, via the quality assessment we performed, we suggest that areas away from the coast need further investigation in terms of MODIS data accuracies, and more in situ data need to be acquired in these areas.

The soil study (chapter 5), despite being a preliminary study with limited training data, is the first study that uses a UAV-borne hyperspectral system to map topsoil organic matter in a fine scale of 7cm. Our soil study is the basis for future high-resolution soil properties mapping studies in various agricultural field sites. It takes advantage of the fine spatial scale data that UAVs can acquire due to their close-range mapping. It also indicates how spectral properties can be used and combined with laboratory analysis to calibrate predictive models. With more training data, different machine-learning algorithms can be tested for such model calibrations in future studies.

6.2 Potential of the UAVs for hydrological studies

Based on the studies of this thesis, UAVs proved a very promising technology for assisting the hydrological studies of fine scales. Their ability to offer high spatiotemporal resolutions that satellites and crewed aircarafts cannot provide increases their use in various environmental applications, especially in challenging environments.

While being rapidly evolving, UAV technology nowadays is much more advanced than four years ago, when this Ph.D. thesis started: Not only the newly manufactured UAVs are more advanced in terms of characteristics (smaller size, lighter weight, etc.), but also the software for flight planning and data processing come with more advanced functions that help the users extract the final remote sensing product with fewer efforts and time. Also important is the technical evolution of the sensors which are nowadays smaller, lighter, and with advanced technical characteristics that provide much more accurate data. More advanced characteristics of the newly manufactured sensors also aim at less time spent in the field: Multi/hyper-spectral cameras with integrated irradiance sensors, sensors with very accurate Inertial Navigation Systems, can, for example, eliminate the need for radiometric calibration targets and GCPs in the field, respectively.

However, despite the various fields of hydrogeological applications in which UAVs can be used, their operation is not straightforward. Many challenges need to be taken into consideration and plan the field campaigns accordingly for high-quality data acquisition. These technical challenges are addressed in the following section and recommendations for future UAV campaigns in similar environments and similar studies are made based on the experiences of the projects of this thesis

6.3 Technical challenges of the uncrewed aerial vehicles

Accurate flight planning is crucial for the acquisition of good-quality data. Within neighboring flight lines, it is important to retain the same flying altitude above ground to avoid different ground sampling distances and footprint sizes of the overlapping parts of the flying lines.

Favorable weather conditions should also be reassured before going to the field. Wind-free flights, for instance, are essential to avoid additional shifts of the UAV that can make the operation of the IMU even more challenging.
Sensor limitations increase the time spent in the field, and the data processing steps and they reduce the quality of the data. For example, our heavy AisaKestrel hyperspectral sensor with a limited flying time of around 8-9 minutes would require more than one flight to cover the whole area in case of a bigger study area. The occlusion of our LiDAR system's signal from the canopies and the single returns at the operation height of 70-80 m for the needs of our forest snow studies led to data gaps that had to be filled by performing additional overlapped patterns. The low LiDAR point densities can also affect the data quality and require additional LiDAR flights to ensure full coverage of the area of interest. The co-registration of the over-laced patterns introduced inaccuracies which were propagated to the following processing steps until the extraction of the snow maps. Consequently, the choice of sensors that fulfill the characteristics and the need of each specific study is of high importance.
For a successful field campaign, besides accurate flight planning and the appropriate sensor related to the study's needs, additional steps need to be performed on the field site to ensure the highest possible accuracy. The well-distributed within the field site GCPs are needed for enhancing the georeferencing of the UAV data besides the GPS accuracy of the mounted sensor. GCPs can also act as stable features for the co-registration of LiDAR-derived point clouds or the co-registration of neighboring hyperspectral flight lines during the creation of the hyperspectral orthomosaic.

6.4 Uncrewed surface vehicles in the future

USVs with their ability to cover spatially large areas of the ocean surface fast and at low operational costs compared to other crewed boats have a high potential for use in hydrographic studies and ocean monitoring (Patterson et al., 2022). In the context of this thesis, Saildrone data proved very efficient in validating coarse-resolution satellite sea surface temperature products. Their high sampling frequency makes the Saildrone technology very promising for potential uses in downscaling satellite products and identifying sub-pixel variations. The evolving technology of the USVs in terms of long endurance and autonomous navigation can assist their use in very isolated areas in future campaigns. Consequently, we can expect USVs and Saildrone in particular to monitor the ocean surface in ever bigger spatial extends away from the coast, and therefore, according to our ocean sea surface temperature study (chapter 4) assist the better validation of satellite products away from the coast as well. The areas away from the coast, due to the dynamics of the ocean are areas where accessibility and data collection are very dangerous and restricted. Another interesting achievement would be the use of Saildrone and more advanced USVs for inland water bodies monitoring, even though autonomous vehicles have already started being used in inland water studies (Cheng et al., 2021; Dunbabin and Grinham, 2017). The use of USVs in inland waters has been restricted so far by GPS failures, fog, and obstacles (Cheng et al., 2021).
Until now, Saildrones have been mainly used for studies in oceans and recently in lakes. By achieving to monitor smaller water bodies such as lakes, rivers, canals, etc. they can tremendously assist in small-scale hydrogeological studies across the world.

6.5 Personal Outlook

I believe that this thesis managed to successfully contribute to the improvement of the study of different hydrological processes by using the innovative technology of uncrewed vehicles. The initial aim which I believe is eventually achieved is to pursue a dissertation that integrates various remote sensing data from new and existing platforms, to extract innovative datasets for the remote sensing scientific community, and to provide significant technical and scientific inputs.

I am very optimistic, and I hope that this work will inspire future studies and motivate researchers to use more and more and enhance the promising technology of uncrewed vehicles.

Bibliography

Acharya, B.S., Bhandari, M., Bandini, F., Pizarro, A., Perks, M., Joshi, D.R., Wang, S., Dogwiler, T., Ray, R.L., Kharel, G., Sharma, S., 2021. Uncrewed Aerial Vehicles in Hydrology and Water Management: Applications, Challenges, and Perspectives. Water Resour. Res. 57. https://doi.org/10.1029/2021WR029925

Alevizos, E., Oikonomou, D., Argyriou, A.V., Alexakis, D.D., 2022. Fusion of Drone-Based RGB and Multi-Spectral Imagery for Shallow Water Bathymetry Inversion. Remote Sens. 14, 1127. https://doi.org/10.3390/rs14051127

Arango, J.G., Nairn, R.W., 2020. Prediction of Optical and Non-Optical Water Quality Parameters in Oligotrophic and Eutrophic Aquatic Systems Using a Small Uncrewed Aerial System. Drones 4, 1. https://doi.org/10.3390/drones4010001

Baluja, J., Diago, M.P., Balda, P., Zorer, R., Meggio, F., Morales, F., Tardaguila, J., 2012. Assessment of vineyard water status variability by thermal and multispectral imagery using an uncrewed aerial vehicle (UAV). Irrig. Sci. 30, 511–522. https://doi.org/10.1007/s00271-012-0382-9

Bierman, P., Lewis, M., Ostendorf, B., Tanner, J., 2011. A review of methods for analysing spatial and temporal patterns in coastal water quality. Ecol. Indic., Spatial information and indicators for sustainable management of natural resources 11, 103–114. https://doi.org/10.1016/j.ecolind.2009.11.001

Brunner, P., Hendricks Franssen, H.-J., Kgotlhang, L., Bauer-Gottwein, P., Kinzelbach, W., 2007. How can remote sensing contribute in groundwater modeling? Hydrogeol. J. 15, 5–18. https://doi.org/10.1007/s10040-006-0127-z

Cao, Q., Yu, G., Qiao, Z., 2022. Application and recent progress of inland water monitoring using remote sensing techniques. Environ. Monit. Assess. 195, 125. https://doi.org/10.1007/s10661-022-10690-9

Casas-Mulet, R., Pander, J., Ryu, D., Stewardson, M.J., Geist, J., 2020. Uncrewed Aerial Vehicle (UAV)-Based Thermal Infra-Red (TIR) and Optical Imagery Reveals Multi-Spatial Scale Controls of Cold-Water Areas Over a Groundwater-Dominated Riverscape. Front. Environ. Sci. 8.

Chadwick, K.D., Brodrick, P.G., Grant, K., Goulden, T., Henderson, A., Falco, N., Wainwright, H., Williams, K.H., Bill, M., Breckheimer, I., Brodie, E.L., Steltzer, H., Williams, C.F.R., Blonder, B., Chen, J., Dafflon, B., Damerow, J., Hancher, M., Khurram, A., Lamb, J., Lawrence, C.R., McCormick, M., Musinsky, J., Pierce, S., Polussa, A., Hastings Porro, M., Scott, A., Singh, H.W., Sorensen, P.O., Varadharajan, C., Whitney, B., Maher, K., 2020. Integrating airborne remote sensing and field campaigns for ecology and Earth system science. Methods Ecol. Evol. 11, 1492–1508. https://doi.org/10.1111/2041-210X.13463

Chawla, I., Karthikeyan, L., Mishra, A.K., 2020. A review of remote sensing applications for water security: Quantity, quality, and extremes. J. Hydrol. 585, 124826. https://doi.org/10.1016/j.jhydrol.2020.124826

Cheng, Y., Jiang, M., Zhu, J., Liu, Y., 2021. Are We Ready for Uncrewed Surface Vehicles in Inland Waterways? The USVInland Multisensor Dataset and Benchmark. IEEE Robot. Autom. Lett. 6, 3964–3970. https://doi.org/10.1109/LRA.2021.3067271

Chiodi, A.M., Zhang, C., Cokelet, E.D., Yang, Q., Mordy, C.W., Gentemann, C.L., Cross, J.N., Lawrence-Slavas, N., Meinig, C., Steele, M., Harrison, D.E., Stabeno, P.J., Tabisola, H.M., Zhang, D., Burger, E.F., O'Brien, K.M., Wang, M., 2021. Exploring the Pacific Arctic Seasonal Ice Zone With Saildrone USVs. Front. Mar. Sci. 8.

Cui, X., Guo, X., Wang, Y., Wang, X., Zhu, W., Shi, J., Lin, C., Gao, X., 2019. Application of remote sensing to water environmental processes under a changing climate. J. Hydrol. 574, 892–902. https://doi.org/10.1016/j.jhydrol.2019.04.078

DeBell, L., Anderson, K., Brazier, R.E., King, N., Jones, L., 2016. Water resource management at catchment scales using lightweight UAVs: current capabilities and future perspectives. J. Uncrewed Veh. Syst. 4, 7–30. https://doi.org/10.1139/juvs-2015-0026

Dunbabin, M., Grinham, A., 2017. Quantifying Spatiotemporal Greenhouse Gas Emissions Using Autonomous Surface Vehicles. J. Field Robot. 34, 151–169. https://doi.org/10.1002/rob.21665

Flores-Anderson, A.I., Griffin, R., Dix, M., Romero-Oliva, C.S., Ochaeta, G., Skinner-Alvarado, J., Ramirez Moran, M.V., Hernandez, B., Cherrington, E., Page, B., Barreno, F., 2020. Hyperspectral Satellite Remote Sensing of Water Quality in Lake Atitlán, Guatemala. Front. Environ. Sci. 8.

García-López, S., Vélez-Nicolás, M., Zarandona-Palacio, P., Curcio, A.C., Ruiz-Ortiz, V., Barbero, L., 2023. UAV-borne LiDAR revolutionizing groundwater level mapping. Sci. Total Environ. 859, 160272. https://doi.org/10.1016/j.scitotenv.2022.160272

Gholizadeh, M.H., Melesse, A.M., Reddi, L., 2016. A Comprehensive Review on Water Quality Parameters Estimation Using Remote Sensing Techniques. Sensors 16, 1298. https://doi.org/10.3390/s16081298

Golubkov, G.V., Manzhelii, M.I., Berlin, A.A., Lushnikov, A.A., Eppelbaum, L.V., 2018. Effects of the Interaction of Microwave Radiation with the Atmosphere on the Passive Remote Sensing of the Earth's Surface: Problems and Solutions (Review). Russ. J. Phys. Chem. B 12, 725–748. https://doi.org/10.1134/S1990793118040061

Herndon, K., Muench, R., Cherrington, E., Griffin, R., 2020. An Assessment of Surface Water Detection Methods for Water Resource Management in the Nigerien Sahel. Sensors 20, 431. https://doi.org/10.3390/s20020431

Hill, D.J., Pypker, T.G., Church, J., 2020. Applications of Unpiloted Aerial Vehicles (UAVs) in Forest Hydrology, in: Levia, D.F., Carlyle-Moses, D.E., Iida, S., Michalzik, B., Nanko, K., Tischer, A. (Eds.), Forest-Water Interactions, Ecological Studies. Springer International Publishing, Cham, pp. 55–85. https://doi.org/10.1007/978-3-030-26086-6_3

Isgró, M.A., Basallote, M.D., Barbero, L., 2022. Uncrewed Aerial System-Based Multispectral Water Quality Monitoring in the Iberian Pyrite Belt (SW Spain). Mine Water Environ. 41, 30–41. https://doi.org/10.1007/s10230-021-00837-4

Jacobs, J.M., Hunsaker, A.G., Sullivan, F.B., Palace, M., Burakowski, E.A., Herrick, C., Cho, E., 2021. Snow depth mapping with unpiloted aerial system LiDAR observations: a case study in Durham, New Hampshire, United States. The Cryosphere 15, 1485–1500. https://doi.org/10.5194/tc-15-1485-2021

Kumar, D.N., Tv, R., 2013. Remote Sensing Applications in Water Resources. J. Indian Inst. Sci. 93, 163–188.

Levy, J.S., Johnson, J.T.E., 2021. Remote Soil Moisture Measurement from Drone-Borne Reflectance Spectroscopy: Applications to Hydroperiod Measurement in Desert Playas. Remote Sens. 13, 1035. https://doi.org/10.3390/rs13051035

Liu, H., Yu, T., Hu, B., Hou, X., Zhang, Z., Liu, X., Liu, J., Wang, X., Zhong, J., Tan, Z., Xia, S., Qian, B., 2021. UAV-Borne Hyperspectral Imaging Remote Sensing System Based on Acousto-Optic Tunable Filter for Water Quality Monitoring. Remote Sens. 13, 4069. https://doi.org/10.3390/rs13204069

Lu, Q., Si, W., Wei, L., Li, Z., Xia, Z., Ye, S., Xia, Y., 2021. Retrieval of Water Quality from UAV-Borne Hyperspectral Imagery: A Comparative Study of Machine Learning Algorithms. Remote Sens. 13, 3928. https://doi.org/10.3390/rs13193928

Maesano, M., Khoury, S., Nakhle, F., Firrincieli, A., Gay, A., Tauro, F., Harfouche, A., 2020. UAV-Based LiDAR for High-Throughput Determination of Plant Height and Above-Ground Biomass of the Bioenergy Grass Arundo donax. Remote Sens. 12, 3464. https://doi.org/10.3390/rs12203464

Mbuh, M., 2019. Use of Hyperspectral Remote Sensing to Estimate Water Quality, Processing and Analysis of Hyperspectral Data. IntechOpen. https://doi.org/10.5772/intechopen.89222

Mouw, C.B., Greb, S., Aurin, D., DiGiacomo, P.M., Lee, Z., Twardowski, M., Binding, C., Hu, C., Ma, R., Moore, T., Moses, W., Craig, S.E., 2015. Aquatic color radiometry remote sensing of coastal and inland waters: Challenges and recommendations for future satellite missions. Remote Sens. Environ. 160, 15–30. https://doi.org/10.1016/j.rse.2015.02.001

Nikishin, V., Durmanov, M., Skorik, I., 2020. Autonomous Uncrewed Surface Vehicle for Water Surface Monitoring. TransNav Int. J. Mar. Navig. Saf. Sea Transp. 14, 853–858. https://doi.org/10.12716/1001.14.04.09

Olmanson, L., Brezonik, P., Bauer, M., 2013. Airborne Hyperspectral Remote Sensing to Assess Spatial Distribution of Water Quality Characteristics in Large Rivers: The Mississippi River and Its Tributaries in Minnesota. Remote Sens. Environ. 130, 254–265. https://doi.org/10.1016/j.rse.2012.11.023

Patterson, R.G., Lawson, E., Udyawer, V., Brassington, G.B., Groom, R.A., Campbell, H.A., 2022. Uncrewed Surface Vessel Technological Diffusion Depends on Cross-Sectoral Investment in Open-Ocean Archetypes: A Systematic Review of USV Applications and Drivers. Front. Mar. Sci. 8.

Peterson, J., Zhang, Z., 2005. High-Resolution DEM Generated from LiDAR Data for Water Resource Management 7.

Sagan, V., Peterson, K.T., Maimaitijiang, M., Sidike, P., Sloan, J., Greeling, B.A., Maalouf, S., Adams, C., 2020. Monitoring inland water quality using remote sensing: potential and limitations of spectral indices, bio-optical simulations, machine learning, and cloud computing. Earth-Sci. Rev. 205, 103187. https://doi.org/10.1016/j.earscirev.2020.103187

Schaeffer, B.A., Schaeffer, K.G., Keith, D., Lunetta, R.S., Conmy, R., Gould, R.W., 2013. Barriers to adopting satellite remote sensing for water quality management. Int. J. Remote Sens. 34, 7534–7544. https://doi.org/10.1080/01431161.2013.823524

Sheffield, J., Wood, E.F., Pan, M., Beck, H., Coccia, G., Serrat-Capdevila, A., Verbist, K., 2018. Satellite Remote Sensing for Water Resources Management: Potential for Supporting Sustainable Development in Data-Poor Regions. Water Resour. Res. 54, 9724–9758. https://doi.org/10.1029/2017WR022437

Sibanda, M., Mutanga, O., Chimonyo, V.G.P., Clulow, A.D., Shoko, C., Mazvimavi, D., Dube, T., Mabhaudhi, T., 2021. Application of Drone Technologies in Surface Water Resources Monitoring and Assessment: A Systematic Review of Progress, Challenges, and Opportunities in the Global South. Drones 5, 84. https://doi.org/10.3390/drones5030084

Sun, X., Zhang, Yunlin, Shi, K., Zhang, Yibo, Li, N., Wang, W., Huang, X., Qin, B., 2022. Monitoring water quality using proximal remote sensing technology. Sci. Total Environ. 803, 149805. https://doi.org/10.1016/j.scitotenv.2021.149805

Totland, A., Johnsen, E., 2022. Kayak Drone – a silent acoustic uncrewed surface vehicle for marine research. Front. Mar. Sci. 9.

Trepekli, K., Balstrøm, T., Friborg, T., Fog, B., Allotey, A.N., Kofie, R.Y., Møller-Jensen, L., 2022. UAV-borne, LiDAR-based elevation modelling: a method for improving local-scale urban flood risk assessment. Nat. Hazards 113, 423–451. https://doi.org/10.1007/s11069-022-05308-9

Vazquez-Cuervo, J., Castro, S.L., Steele, M., Gentemann, C., Gomez-Valdes, J., Tang, W., 2022. Comparison of GHRSST SST Analysis in the Arctic Ocean and Alaskan Coastal Waters Using Saildrones. Remote Sens. 14, 692. https://doi.org/10.3390/rs14030692

Vélez-Nicolás, M., García-López, S., Barbero, L., Ruiz-Ortiz, V., Sánchez-Bellón, Á., 2021. Applications of Uncrewed Aerial Systems (UASs) in Hydrology: A Review. Remote Sens. 13, 1359. https://doi.org/10.3390/rs13071359

Yang, T.H., Hsiung, S.H., Kuo, C.H., Tsai, Y.D., Peng, K.C., Peng, K.C., Hsieh, Y.C., Shen, Z.J., Feng, J., Kuo, C., 2018. Development of uncrewed surface vehicle for water quality monitoring and measurement, in: 2018 IEEE International Conference on Applied System Invention (ICASI). Presented at the 2018 IEEE International Conference on Applied System Invention (ICASI), pp. 566–569. https://doi.org/10.1109/ICASI.2018.8394316

Yu B. a. I., Zhizhong Z., Liancun X.I.U., Hangjian Z., Yingxu X., 2022. UAV hyperspectral remote sensing technology and its application progress in natural resources survey. East China Geol. 43, 527–538. https://doi.org/10.16788/j.hddz.32-1865/P.2022.04.011

Zarco-Tejada, P.J., González-Dugo, V., Berni, J.A.J., 2012. Fluorescence, temperature and narrow-band indices acquired from a UAV platform for water stress detection using a micro-hyperspectral imager and a thermal camera. Remote Sens. Environ., Remote Sensing of Urban Environments 117, 322–337. https://doi.org/10.1016/j.rse.2011.10.007

Zhang, C., Levine, A.F., Wang, M., Gentemann, C., Mordy, C.W., Cokelet, E.D., Browne, P.A., Yang, Q., Lawrence-Slavas, N., Meinig, C., Smith, G., Chiodi, A., Zhang, D., Stabeno, P., Wang, W., Ren, H.-L., Peterson, K.A., Figueroa, S.N., Steele, M., Barton, N.P., Huang, A., Shin, H.-C., 2022. Evaluation of Surface Conditions from Operational Forecasts Using In Situ Saildrone Observations in the Pacific Arctic. Mon. Weather Rev. 150, 1437–1455. https://doi.org/10.1175/MWR-D-20-0379.1

Curriculum Vitae

Kalliopi Koutantou
Date of Birth: 03.01.1994

EDUCATION

Sept. 2018-Jan. 2023: **Doctor of Philosophy (Ph.D.)**
University of Neuchâtel
Centre for Hydrogeology and Geothermics (CHYN)
Laboratory of Hydrogeological Processes
Remote Sensing

Sept. 2012-July 2017: **Master of Engineering (MEng)**
National Technical University of Athens (NTUA)
Geomatics Engineering; Remote Sensing Specialization
61 subjects, 300 ECTS, GPA: 8.52/10 (top 3%, graduated 3rd in the year of 2017)

PUBLICATIONS

Koutantou, K., Mazzotti, G., & Brunner, P. (2021). UAV-BASED LIDAR HIGH-RESOLUTION SNOW DEPTH MAPPING IN THE SWISS ALPS: COMPARING FLAT AND STEEP FORESTS. *The International Archives of the Photogrammetry, Remote Sensing and Spatial Information Sciences*, *XLIII-B3-2021*, 477–484. https://doi.org/10.5194/isprs-archives-XLIII-B3-2021-477-2021

Koutantou, K., Mazzotti, G., Jonas T., Webster C., & Brunner, P. (2022). Exploring snow distribution dynamics in steep forested slopes with UAV-borne LiDAR. *Cold Regions Science and Technology, Volume 200, 103587.* https://doi.org/10.1016/j.coldregions.2022.103587

Koutantou, K., Brunner, P., & Vazquez-Cuervo, J. Validation of NASA Sea Surface Temperature Satellite Products using Saildrone data. Remote Sensing, Special Issue ‘‘Advances in Retrieval, Operationalization, Monitoring and Application of Sea Surface Temperature II’’, *under revision*

EXPERIENCE

May 2022-September 2022: **Research Intern,** NASA Jet Propulsion Laboratory, Pasadena, California, Ocean Circulation and Air-Sea Interaction Group, Supervisor: Dr. Jorge Vazquez-Cuervo

- Validation of Level-2 and Level-4 Sea Surface Temperature NASA satellite products using Saildrone (uncrewed surface vehicle) data
- Validation of the quality levels of Level-2 MODIS data

Dec. 2019-June 2021: **Guest Ph.D. Researcher**, WSL Swiss Federal Institute for Snow and Avalanche Research SLF, Davos, Switzerland, Snow Hydrology group, Supervisor: Dr. Tobias Jonas

- Assessing the forest snow pattern dynamics in steep Alpine forests using UAV-borne LiDAR
  The first research conducted in a steep forested environment using UAV-borne LiDAR

Oct. 2018-Sept. 2022: **External Ph.D. Researcher**, University of Lausanne (UNIL), Institute of Earth Surface Dynamics (IDYST), Remote Sensing and Pattern analysis group, Professor Gregoire Mariethoz

- Acquiring and processing UAV-borne RGB, multispectral and thermal data for hydrogeological studies

Sept. 2018-Jan. 2023: **Ph.D. Candidate**, University of Neuchatel, Centre for Hydrogeology and Geothermics, Laboratory of hydrogeological processes, Neuchâtel, Switzerland, Supervisor: Prof. Philip Brunner

- Use of a state-of-the-art UAV system for studying hydrogeological processes
  Ph.D. Projects:
  UAV-borne LiDAR snow mapping in the Swiss Alps: Case studies of flat and steep forests
  Mapping of soil organic matter in a Swiss agriculture field site: A preliminary study
  Validation of NASA Sea Surface Temperature satellite products using Saildrone data

Mar. 2018-July 2018: **Software Testing Intern,** Pix4D, Innovation Park of École Polytechnique Féderale de Lausanne (EPFL), Lausanne, Switzerland, Supervisor: Dr. Martin Rehak

- Working with the calibration and radiometry team on the UAV-based photogrammetry software “Pix4Dmapper”

Sept. 2017-Jan. 2018: **Research Intern-Teaching assistant,** Geodetic Engineering Laboratory (TOPO Lab), École Polytechnique Féderale de Lausanne (EPFL), Switzerland, Supervisor: Prof. Bertrand Merminod

- Lake ice monitoring using hyperspectral data over lake Onega in the context of the multidisciplinary Russian/Swiss project “Life under Ice”
- Lake ice classification using machine learning methods
- Teaching assistant for 2nd year’s Bachelor course “Méthodes Quantitatives 1” (Propagation of errors, Least Squares Method based on Matlab applications)

Jan. 2017-Jul. 2017: **MSc Thesis Researcher,** Laboratory of Remote Sensing, National Technical University of Athens (NTUA), Supervisor: Prof. Karathanassi Vassilia, Grade: 10/10

- Study of the ocean upwelling phenomenon using satellite multispectral data

Sept. 2016-Dec. 2016: **MSc project Researcher,** Laboratory of Remote Sensing**,** National Technical University of Athens (NTUA), Supervisor: Dr. Doulamis Nikolaos, Grade: 10/10

- Applications of interconnected digital systems: Techniques for the analysis and processing of multispectral remote sensing images with application to the environment

TECHNICAL SKILLS

Remote sensing software (QGIS, ER Mapper, ENVI, SNAP, ERDAS, SeaDAS, Panoply)
Photogrammetric software (Pix4DMapper)
Machine Learning (Regression and classification algorithms)
Programming (Python, Matlab, R)
Graphic Software
Microsoft Office

HONORS & AWARDS

June 2021: "Fonds des donation" grant for 5 months internship at NASA Jet Propulsion Laboratory, University of Neuchatel, Switzerland
Oct. 2018: 3rd prize in the pitch contest "My start-up idea in 60 sec", APML association of EPFL, EPFL, Lausanne, Switzerland
Dec. 2017: "Limmat Stiftung" award for achieving the 3rd highest grade in the graduation year of 2017, Limmat Stiftung, Zürich, Switzerland
Sept. 2017: Research scholarship, École Polytechnique Fédérale de Lausanne(EPFL), Lausanne, Switzerland
Aug. 2017: Scholarship from "equal society" to attend RG Bootcamp 2017 for new entrepreneurs organized by ALBA and "The American College of Greece", Athens, Greece
July 2017: Bodossaki Foundation Scholarship for MSc studies in Greece, Athens, Greece
Mar. 2011: Euroscola program of the European Parliament selected participant, Strasbourg, France
Sept. 2009: Award from the Greek Minister of Education for excellent performance, Heraklion, Greece

LANGUAGES

Greek (Native)
English; ECPE, C2, Michigan University
German; B1, Goethe Institute.V., Zertifikat Deutsch
French (A2 level)
Italian (A1 level)

HOBBIES & INTERESTS

Open water swimming (3 bronze and 1 silver medal at Greek open water swimming races)
Water polo (water polo player for “Lausanne natation”, the year 2021-2022)
Volleyball
Cycling
Poems, novels, plays writing (20 literature awards & distinctions in Greek competitions)
Volunteerism